

**THE LIGHT-LINE-TETHERING TECHNIQUE FOR DETERMINING  
THE AERODYNAMIC DERIVATIVES OF AN AIR CUSHION VEHICLE**

*G. KURYLOWICH*  
*UNIVERSITY of TORONTO*

**Distribution of this  
document is unlimited.**


FOREWORD

This report was prepared by the Institute for Aerospace Studies, University of Toronto, Ont., Canada. Financial support for the work was received from the Defence Research Board and National Research Council of Canada, the U. S. A. F. Research and Technology Division, Flight Dynamics Laboratory Control Criteria Branch, (Contract AF-33(657)8451) and the Vertol Division, Boeing Aircraft Co. The investigation was conducted from Oct. 1960 to May 1965. The contract was initiated under Project 8219 "Stability and Control Investigations" Task No. 821907" V/STOL Aerodynamic Stability and Control. "

Contributions to this study were made by Messrs. J. Liiva, R. C. Radford, B. W. Gowans, and G. Kurylowich, who designed and constructed the track and the models, and carried out all the experiments and mathematical analysis. Professor B. Etkin initiated the project and served as principal investigator and supervisor.

Manuscript released by the author July 13, 1965 for publication as an RTD Technical Report. With minor differences, it has also been published as UTIAS Report No. 110, August 1965.

This technical report has been reviewed and is approved.

  
C. B. WESTBROOK  
Chief, Control Criteria Branch  
Flight Control Division  
AF Flight Dynamics Laboratory

## ABSTRACT

A complete feasibility study was performed on a new technique for determining ACV aerodynamic derivatives. A circular track simulated "ground" while the vehicle, tethered to a centerpost by means of a light cable, flew a circular flight path above the track surface. A step on the "ground" perturbed the vehicle from equilibrium and the resulting oscillations were recorded by a movie camera. The results obtained indicated that many derivatives were functions of height.

Although scatter in the data permitted a qualitative study only, it was concluded that the scatter resulted from random errors in the recorded time histories and the manner in which the cable was attached to the vehicle. By making certain improvements in the experimental design and apparatus (especially using a larger track) it was concluded that all derivatives could be obtained with satisfactory precision with this technique.

## TABLE OF CONTENTS

	<u>Page</u>
1. INTRODUCTION	1
2. EXPERIMENTAL APPARATUS	4
2.1 Track Development	4
2.2 Flight Recording	4
2.3 The Centerpost-to-Model Assembly	6
2.4 Model Development	7
2.5 Measurement of R. F. M.	8
3. FILM ANALYSIS	9
3.1 Reduction of Data	9
3.2 The Symmetrical Parameters	12
3.3 The Antisymmetric Parameters	13
3.4 The Track Reduction Equations	14
4. DEVELOPMENT OF THE VEHICLE'S EQUATIONS OF MOTION	16
4.1 Choice of Axes	16
4.2 Moments of Inertia	16
4.3 Linearization of Angular Quantities, Velocities, and Forces	16
4.4 The Equations of Motion	18
4.5 Cable Effects (General)	19
4.6 Cable Influences on Vehicle Forces	20
4.6.1 The Height Effect	20
4.6.2 Roll Cable Effects	21
4.6.3 The Yaw Cable Effects	21
4.6.4 The $\dot{h}$ Cable Derivatives	22
4.7 The Air Reactions	22
4.8 Ground Roughness Input	26
4.9 The Nondimensional Equations	28

# Contrails

	<u>Page</u>
5.	DERIVATIVE EXTRACTION TECHNIQUE 31
5.1	Introduction 31
5.2	A Survey of the Techniques 31
5.3	A Comparison of the 4 Selected Methods 33
5.4	Selection of the Most Appropriate Technique 38
6.	EXPECTED ACCURACIES IN FINAL RESULTS 39
6.1	Introduction 39
6.2	Application of the Technique to the Equations of Motion 39
6.3	The Conditioning Check 43
6.4	The Effects of Data Scatter on the Final Results 45
6.5	Preliminary Error Analysis 46
7.	FINAL RESULTS AND DISCUSSION 47
7.1	Testing Procedure 47
7.2	Reduced Data and Analogue Comparison 48
7.3	Equilibrium Data 48
7.4	The Extracted Derivatives 49
7.5	Error Analysis 51
7.6	Track Improvements 53
8.	CONCLUSIONS 55
	APPENDIX I The General Equations of Motion. 56
	APPENDIX II A Theoretical Evaluation of Some Aerodynamic Derivatives. 58
	APPENDIX III The Scaled Analogue Equation of Motion. 66
	REFERENCES 68

ILLUSTRATIONS

<u>Figure</u>		<u>Page</u>
1	UTIAS CIRCULAR TRACK. . . . .	77
2	THE CENTRE POST INSTALLATION. . . . .	78
3	FILM ANALYSER. . . . .	79
4a	THE EXPERIMENTAL ACV VEHICLE. . . . . (COURTESY OF B. GOWANS)	80
4b	THE SCHEMATIC OF THE ACV. . . . . (COURTESY OF B. GOWANS-REF. 6)	81
5	TEST RESULTS OF JETEX UNIT-THRUST VS TIME. .	82
6	THE TARGET POINT MEASUREMENTS. . . . .	83
7	TARGET POINTS RELATIVE TO BODY FIXED AXIS. .	83
8	VERTICAL PARALLAX CORRECTION . . . . .	84
9	HORIZONTAL PARALLAX AND GRID CURVATURE CORRECTION. . . . .	84
10	AXES SYSTEMS FOR EQUATIONS OF MOTION. . . .	85
11	THE VEHICLE'S FLIGHT PATH. . . . .	85
12a	THE CABLE HEIGHT DERIVATIVE. . . . .	86
12b	THE CABLE ROLL DERIVATIVE. . . . .	87
12c	THE CABLE YAW DERIVATIVE. . . . .	87
12d	THE CABLE PLUNGE DAMPING DERIVATIVE. . . .	88
13	GROUND INPUTS. . . . .	89
14	A COMPARISON BETWEEN A TYPICAL PITCH PERTURBATION AND THE SIMULATED EXPERIMENTAL OUTPUT. .	90

# Contrails

<u>Figure</u>		<u>Page</u>
15	THE EFFECT OF SCATTER ON COEFFICIENTS a AND b. . . . .	91
16	ANALOGUE SCHEMATIC. . . . .	91a
17a	THE EFFECT OF SCATTER ON THE FLIGHT DERIVATIVES. . . . .	92
17b	THE EFFECT OF SCATTER ON THE FLIGHT DERIVATIVES. . . . .	93
18	PITCH PERTURBATION VS TIME (H=.070). . . . .	94
19	PITCH PERTURBATION VS TIME (H=.054). . . . .	95
20	PITCH PERTURBATION VS TIME (H=.043). . . . .	96
21	HEIGHT PERTURBATION VS TIME (H=.070). . . . .	97
22	HEIGHT PERTURBATION VS TIME (H=.054). . . . .	98
23	HEIGHT PERTURBATION VS TIME (H=.043). . . . .	99
24	ROLL PERTURBATION VS TIME (H=.070). . . . .	100
25	ROLL PERTURBATION VS TIME (H=.054). . . . .	101
26	ROLL PERTURBATION VS TIME (H=.043). . . . .	102
27	YAW PERTURBATION VS TIME (H=.070). . . . .	103
28	YAW PERTURBATION VS TIME (H=.054). . . . .	104
29	YAW PERTURBATION VS TIME (H=.043). . . . .	105
30	A COMPARISON OF THE EXPERIMENTAL PITCH PERTURBATIONS AND THE ANALOGUE COMPUTER RESULTS . . . . .	106
31	A COMPARISON OF THE EXPERIMENTAL HEIGHT PERTURBATIONS AND THE ANALOGUE COMPUTER RESULTS . . . . .	107

# Contrails

<u>Figure</u>		<u>Page</u>
32	A COMPARISON OF THE EXPERIMENTAL ROLL PERTURBATIONS AND THE ANALOGUE COMPUTER RESULTS. . . . .	108
33	A COMPARISON OF THE EXPERIMENTAL YAW PERTURBATIONS AND THE ANALOGUE COMPUTER RESULTS. . . . .	109
34	THE AUGMENTATION CURVE. . . . .	110
35	$L/L_s$ VS $C_\mu$	111
36	$L/L_s$ VS $(\dot{q}/q_J)$ . $(\frac{H. Deq}{G})^{\frac{1}{2}}$	111
37	$C_{Z_H}$ AND $C_{Z_H^*}$ VS H	112
38a	$C_{Z_\phi}$ , $C_{Z_q}$ AND $C_{Z_\theta}$ VS H	113
38b	LIFT VS $\alpha$ (COURTESY OF K. DAU-REF. 13). . . . .	114
39	$C_{M_\theta}$ AND $C_{M_q}$ VS H	115
40	$C_{M_H}$ , $C_{M_H^*}$ , $C_{l_\phi}$ , $C_{l_p}$ AND $C_{l_\psi}$ VS H	116
41	$C_{l_H^*}$ , $C_{l_r}$ AND THE YAW DERIVATIVES VS H	117
41a	COMPARISON BETWEEN PREDICTED AND EXPERI- MENTAL STANDARD DEVIATIONS	118
42	SCHEMATIC DIAGRAMS FOR APPENDIX B	119



TABLES

<u>Table</u>		<u>Page</u>
1	MODEL DATA	72
2	THE NONDIMENSIONAL SYSTEM	73
3	EXPERIMENTALLY EXTRACTED DERIVATIVES (Mean Value)	74
4	COMPARISON OF THEORETICALLY COMPUTED ERROR AND ACTUAL EXPERIMENTAL ERROR	76

# Contrails

## SYMBOLS

$A_J$	exit area of the annular jet
A, B, C, D, E, F	the moments and products of inertia relative to stability axes (slugs-ft <sup>2</sup> )
$\overline{A}, \overline{B}, \overline{C}, \overline{D}, \overline{E}, \overline{F}, \overline{G}, \overline{H},$ $\overline{P}, \overline{Q}, \overline{S}, \overline{T}, \overline{U}, \overline{W}$	{ constants used in reducing film measurements to vehicle parameters
A', B', C'	moments of inertia relative to body fixed axes ( $I_{x'x'}, I_{y'y'}, I_{z'z'}$ )
$C_\mu$	blowing coefficient ( $C_\mu = \frac{J}{qS}$ )
Deq.	equivalent diameter of the vehicle
D', E', F'	products of inertia relative to the body fixed axes ( $I_{y'z'}, I_{x'z'}, I_{x'y'}$ )
g	acceleration of gravity (ft/sec <sup>2</sup> )
$\underline{h}$	c. g. perturbation from equilibrium
$\overline{h}$	mirror height defined in figure 8
h	total height above "ground"-see section 2.1
$h_s$	ground perturbation
J	jet momentum flux
L	lift for $q \neq 0$
$L_s$	lift for $q/q_J = 0$
$l_1, l_2, l_3, l_4, l_5$	vehicle dimensions
$\mathcal{L}$	Laplacian operator
m	vehicle mass
$m_c$	cable mass
$M_a$	centerpost moment arm

# Contrails

$p, q, r$	angular velocity perturbations
$P_a$	atmospheric pressure
$\Delta P$	pressure rise through the curtain
$q$	forward speed dynamic pressure
$q_J$	cushion jet dynamic pressure
$R$	track radius (centerpost to vehicle c. g.)
$R_c$	cable length
$T$	cable tension
$U$	vehicle velocity (ft/sec)
$V_J$	cushion jet velocity
$X Y X$	the stability axes
$X'Y'Z'$	the vehicle's fixed axes
$\bar{z}_1^+, \bar{z}_2^+, \bar{z}_3^+, \bar{x}_1^+, \bar{x}_3^+$	film measurements in reducing data
$\alpha$	angle of attack
$\alpha^*$	cable angle induced by cable drag
$\beta$	computer constant
$\eta_A, \eta_J$	factors for correcting ideal conditions to that of actual (Appendix B)
$(\theta, \phi, \psi)$	perturbation angles in pitch, roll and yaw
$\Theta, \Phi, \Psi$	total pitch, roll and yaw angles
$\bar{\lambda}$	flight path wave length
$\rho$	density
$\rho_c$	cable density (lb/ft)
$\omega_f$	engine frequency (radians/sec)

# *Contrails*

## 1. INTRODUCTION

During 1957 to 1962, investigators in several countries performed extensive studies on the ACV or Air Cushion Vehicle. Small free flight and wind tunnel vehicles (Ref. 1 and 2) were used to verify the theories developed during this period and these investigations indicated that the vehicles were feasible, that they were relatively insensitive to the consistency of the surface that they travelled over (i. e. water, snow, mud, etc.) and finally that they were stable if certain height restrictions were met. This research, however, dealt mainly with lift augmentation, drag, power requirements, curtain studies and efficiencies. There was a marked lack of information about aerodynamic derivatives. For example, of the thirty papers presented in Reference 2, only 3 produced any moment data while only 2 investigated plunge damping. This indicated that research into the vehicle's aerodynamic derivatives would indeed be useful. Derivative information can be obtained by several means such as the wind tunnel, free flight, rotating arm, and the UTIAS light-line-tethering technique. Let us consider these methods.

Many experiments have been conducted in the wind tunnel (Ref. 2, 8 and 13). The vehicle is usually fixed to 3 struts while a balance system measures lift, drag, side force, and all the moments. Since  $\dot{h}$ ,  $\dot{\theta}$ ,  $\dot{\phi}$ , and  $\dot{\psi}$  do not exist, the damping derivatives cannot be measured. If the vehicle were harnessed with one degree of freedom such that pitch were free, we could determine  $C_{mq}$ ; with freedom in height we obtain  $CZ\dot{H}$ . The underlying point in this is that with a simple harnessing mechanism, the damping derivatives are usually obtained individually and not all at once. Thus a prime disadvantage of wind tunnel testing is that one requires an extremely complicated and expensive harnessing system, which allows six degrees of freedom to the model, before all the vehicle's flight derivatives can be measured simultaneously.

Another difficulty is that of ground representation. With an unmodified wind tunnel, a vehicle's response to a step or sine wave in the ground cannot be determined. Furthermore, P. E. Colin (Ref. 8) indicates that the wind tunnel's boundary layer interacts with the curtain air and affects the resulting vehicle reactions. A moving belt (Ref. 3) and boundary layer bleed off would relieve these problems for smooth, but not for rough, ground.

Free flight testing can, of course, be used in determining the vehicle's flight derivatives. The prime advantages are accuracy and that many derivatives can be obtained simultaneously, while the obvious disadvantage is, of course, cost. Furthermore, if the vehicle is relatively large, outdoor testing is required; the vehicle would then be subjected to undesirable disturbances produced by weather conditions such as atmospheric turbulence, or side winds.

# Contrails

The rotating arm technique, used at the David Taylor Model Basin (Refs. 2 and 31) has two distinct advantages. The need for expensive monitoring and control equipment is eliminated (data can be obtained by photography) and the vehicle need not be self-propelled if pressure lines are included in the rotating arm.

A disadvantage to this method is that one must minimize the effect of the rotating arm by making the vehicle mass to arm mass ratio extremely large. This factor results in a fairly large installation (Ref. 2). Furthermore, the natural frequency of the rotating arm will usually be low and serious interactions between arm and vehicle motion may result (Ref. 31).

The light-line-tethering technique, a new method first proposed by Prof. B. Etkin, is by far the simplest and least expensive. It is analogous to the rotating arm method in that the vehicle is forced into a circular flight path; however, the rotating arm is replaced by a light cable. This method reduces the interaction between the harnessing mechanism and vehicle and permits the use of a smaller installation. The main disadvantage is that the model must be self-propelled.

This report then, describes the UTIAS track facility and presents a feasibility study conducted of this method. The problem areas investigated are as follows:

- (1) The development of the track facility (this includes data recording and data reduction).
- (2) The development of a relatively efficient self-propelled vehicle.
- (3) A survey of the available mathematical techniques for determining the aerodynamic derivatives.
- (4) A theoretical investigation of how progressively increasing scatter in the raw data affects the accuracy of the stability derivatives (this includes a comparison between the above and the actual experimental results.)

As an illustration the derivatives for the particular vehicle developed are presented. The results are based on data obtained from 9 separate runs.

In the light-line-tethering technique, the method of harnessing, i. e. of attaching the cable to the model, determines the cable constraints, and the effective degrees of freedom of the model. The least restraint, of course, is provided by attaching the line at the C. G. In the tests described herein, the

# *Contrails*

attachment is at the left side of the model (see Fig. 12) and hence the cable provides very large constraints in roll and yaw. The experiment is therefore one in which the nominal degrees of freedom are only the longitudinal ones, pitch and plunge. Only the corresponding aerodynamic coefficients would therefore be expected to be derivable with useful precision. In fact, the gyroscopic coupling terms generate appreciable rolling and yawing motions, and some information is obtained about aerodynamic derivatives in roll and yaw as well. Obviously, other harnessing systems can produce other effective degrees of freedom - for example, the roll restraint can be released by attaching cables at two points on the x axis, fore and aft.

## 2. EXPERIMENTAL APPARATUS

### 2.1. Track Development

Initial experiments on the circular track were conducted by J. Liiva (Ref. 4). Eighteen segments of  $\frac{1}{2}$ " thick plywood formed the horizontal "ground" surface, the width of the annular track being 2.5 feet (Fig. 1). The wooden surface, was supported by a framework made from Dexion angles; this assembly facilitated the adjustment for "ground" leveling. The bottom of the Dexion framework was fastened to the concrete floor with Ramset bolts and each frame was cross-braced to form a very strong and stiff structure. The horizontal table, or "ground" was approximately 30 inches above the floor providing convenience in preparing the vehicle for a flight. The outer diameter of the track was 21 feet.

The preliminary tests (Ref. 4) indicated that the following improvements should be made:

The level of adjacent segments of plywood varied throughout the length of the track creating small step-up and step-down inputs to the vehicle while in flight. An improvement was realized by fairing the gaps between adjacent plywood sections with plastic wood and accurately leveling the table. The leveling procedure was performed at 36 stations around the track and at three radial distances from the centre (8, 9, and 10 feet). The 9 foot station measurements provided the accuracy in ground height ( $\pm 1/64$  inches) while the 8 and 10 foot stations produced a measurement of the warp in the table ( $\pm .11$  degrees). Some station levels were checked upon completion of runs (see Fig. 1 for the improved track assembly).

### 2.2. Flight Recording

During a flight, the vehicle was photographed by a 16 mm. movie camera with an electric drive. Originally, a Bolex camera was used with an exposure time of  $1/64$  secs. at 32 frames per second (Ref. 4). Since the model's forward velocity was from 10 to 20 f. p. s., the vehicle moved from 1.8 to 3.6 ins. in horizontal translation during an exposure blurring the vertical gridlines (Fig. 1). This necessitated the use of a new camera, which was adjusted by the manufacturer to produce an exposure time of  $1/1000$  secs. at 32 frames/sec. (Fig. 2). The camera was fixed rigidly over the center of the track by a wooden-Dexion structure which overhung the track and which was firmly attached to the walls of the room housing the whole facility (Fig. 1). The optical path from the camera to the model was completed with a mirror mounted at an angle on a sleeve (Fig. 2). The cable from the model swung the sleeve and mirror in such a way that the mirror was always aimed at the vehicle; the model was always in the camera's field of vision. This type of mounting system was pre-



# Contrails

ferred for the safety of the model. If the camera were mounted directly onto the centerpost sleeve, the inertia of the camera would drag the vehicle towards the centerpost and off the track when the model was accelerating (start of flight) or decelerating (end of flight).

To compensate for the reduced camera exposure time, 33 three hundred watt flood lamps, positioned 2 feet above the tracktable, provided the illumination (Fig. 1). This illumination was increased further by painting the track surface with a white reflective lacquer. These steps produced good pictures when Kodak XX movie film was used (lens aperture  $f = 2.2$ ).

For data reduction purposes, there was a reference grid with horizontal lines one inch apart and vertical lines every four inches. This background stood six inches in height and was 21 feet in diameter (Fig. 1). It was attached to the flood lamp posts such that the very bottom horizontal reference line was 4 inches from the tracktable. A black curtain was then positioned behind this structure for maximum photographic contrast. A check on the gridline height relative to the track was performed for each leveling of the track; gridline accuracy was  $\pm 1/64$  ins.

The reason for the "gap" between the background reference lines and the "ground" was as follows: An experiment was conducted to determine whether the vehicle flew into its own wake on continually circuiting the track. Tufts were placed on approximately 3 feet of the track's circumference (the table top, grid lines and light standards) and the motion of these tufts studied while the ACV was in flight. We found that the wake spilled radially away from the track center and curled up the background grid; the tufts became motionless after the vehicle had passed them by approximately 6 feet. The "gap" then facilitated the removal of this wake from the track "ground" surface; this study proved that no wake problem existed.

There were three reference points on the vehicle; nose, tail and body target points. A frame-by-frame film analysis of the behaviour of these points, both relative to the ground and relative to each other, produced pitch, roll, yaw, and height histories of the vehicles progress around the track (see Section 3). The camera filming speed was calibrated both before and after experimentation by filming the second hand of an electric clock.

Data reduction was performed on the analyzer shown in Fig. 3. The film was projected onto the comparator by a time-and-motion movie projector. It contained a zoom motor, a frame counter and a special transmission which detached the electric drive and permitted manual operation by means of a handcrank. Furthermore, while the electric drive was detached, a filter positioned itself between the lamp and film in the projector preventing the overheating and warping of the film.

# Contrails

The projected picture was viewed on the table of the analyzer (Fig. 3). This table could be rotated 360° if necessary until the horizontal track background gridlines appeared parallel with the lines of a graph paper attached to the slide panel; the protractor could then be used to produce the angle of viewing (accuracy  $\pm .10^\circ$ ). This angular reading was used to determine vehicle velocity perturbation ( $u \neq 0$ , see section 4.7); as the model proceeded along the track, the image of the track rotated in the camera frame due to the stationary camera-rotating mirror arrangement (see above).

The comparator table consisted of two parts: the rotatable section discussed above and a removable white slide panel (Fig. 3). The principle behind this construction was that of the conventional slide-rule. To plot a certain target point at a particular ordinate line on the graph paper, we slid the front panel until that target point rested on the proper line. A screw-spring system was provided for clamping the forepanel to the rotatable table section. The whole assembly could be displaced vertically or horizontally by means of two electric motors providing more degrees of freedom in properly positioning the projected picture relative to the graph paper.

The data reducing procedure, once the above alignments were made, was to plot the target positions on the graph paper versus frame number (the abscissa).

For quicker, and more accurate measurements, a steel rule, calibrated in 1/100 of an inch, was used. This alteration eliminated the necessity of sliding the forepanel back and forth and produced a measurement directly.

## 2.3. The Centerpost-to-Model Assembly

The centerpost (Fig. 2) consisted of a three-legged frame bolted to a wooden platform which was Ramset into the concrete floor. This assembly housed a 3/4 inch diameter steel rod that was adjustable in height, or held rigid by means of set-screws (Ref. 4). The rod was fitted with two ball bearings at the top and an aluminum sleeve was pressed over the outer races of the bearings. The mirror assembly was held firmly on this sleeve, by means of a set-screw. Upon changing the centerpost height relative to the track table, the mirror slant angle could be altered to position the vehicle properly in the camera's view finder (see Section 2.2.)

One light dacron line (tensile strength 6 lbs. and density  $8.56 \times 10^{-5}$  lb./ft.) was used as the connecting link between centerpost and vehicle. At the centerpost, this line was attached to the end of the mirror holder (Fig. 2); the long centerpost arm provided a restoring moment to the rotating mirror if it tended to lead or lag the vehicle. At the vehicle, the line was attached to a bellcrank which rode on a vertical post fixed to the vehicle (Fig. 4a). The body side

target point was glued to the bellcrank such that the target center corresponded to the dacron line's attachment point to the model (Fig. 4a).

The installation provided no control over the vehicle other than forcing the model into a circular flight path. Once started, a flight continued until either the fuel tank became empty or until the vehicle was manually caught, at the entrance to the track (Fig. 1), and the fuel turned off.

## 2.4. Model Development

Some preliminary feasibility tests were made, by J. Liiva, on a GETOL model based on a Vertol Design (Ref. 4). This vehicle, however, was unsuitable for the following reasons:

- 1.) The engine overheated rapidly permitting only approximately 3 circuits around the track.
- 2.) Due to the extremely bad matching of fans to engine and model ducting, the vehicle's efficiency was poor; many collisions between ground and vehicle occurred.

A systematic program was then initiated to produce an adequate model (Ref. 5). Based on a survey of the available fuel and electric power plants, a .35 cubic inch displacement Fox glowplug engine was selected for the new vehicle and a matching propulsion system designed. Performance studies on the vehicle's propulsion system were performed by R. C. Radford (Ref. 5).

This vehicle was not used for the final tests because:

- 1.) Breakages continually occurred; repairs and modifications ultimately increased the weight of the vehicle beyond an acceptable value.
- 2.) The jet momentum flux distribution along the peripheral slots was very poor. Some portions of the annular slots were starved of air creating a break in the curtain and, consequently, a lower hover height. Attempts were made to rectify the situation by:
  - (a) Placing vanes inside the wing forcing air to the tips.
  - (b) Using screens to smooth the distribution. Some success was achieved; however, the resulting large pressure losses drastically reduced the total dynamic pressure at the vehicle's exit.
- 3.) Upon mass balancing (trimming) the vehicle for equilibrium forward flight, the maximum height above ground was reduced to only  $\frac{1}{4}$  inch.

The final model (ACV 4) was built and calibrated by B. Gowans (Fig. 4a and b - Ref. 6). This vehicle was powered by a Cox "Special 15" model airplane engine which developed .46 horsepower at 18,000 r.p.m. A simple axial fan (a commercially available two bladed propeller) 8 inches in diameter

supplied air to the peripheral and stability jets. For propulsion, some of the air was bled off behind the fan and out through the propulsion duct (Fig. 4b). Additional propulsion could be gained by flying the ACV in a nosedown attitude. The model, in its normal configuration (weight 2.6 lbs.), could fly at a height of  $1\frac{1}{2}$  inches above ground (engine cps. = 225) and at speeds ranging between 5 and 20 feet per second. The forward speed was a function of c. g. position; an approximate 2 degree equilibrium pitch angle produced the 5 fps. forward speed and a -2.0 degree equilibrium pitch angle produced 20 fps.

A model Jetex (Rocket) unit was tested to see whether variations in forward speed could be obtained while maintaining a constant c. g. position. The thrust was measured by a dynamometer constructed by B. Gowans (Ref. 6); some results are shown in Fig. 5. These tests indicated that these units were unacceptable because:

1. ) Rocket thrust was unrepeatable - probably because of impurities in the fuel.
2. ) The Jetex unit usually became red-hot and finally ruptured during a test - this could destroy the model.

The vehicle's equilibrium height was changed by adding weight to the vehicle. Coils of solder were positioned around the intake just below the bell mouth (Fig. 4a). Duct Seal was then used as a fairing over these weights to minimize drag. The operational heights above ground were from 1.4 inches (vehicle wt. = 3.08 lbs.) to .9 inches (vehicle wt. = 4.63 lbs.) Table 1 and Fig. 4b illustrate the physical dimensions of the vehicle.

## 2.5. Measurement of R. P. M.

The jet momentum flux of the vehicle was experimentally determined for an engine speed of 225 cps. (Ref. 6). Since the flux is directly proportional to the square of the engine r. p. m., J and  $V_J$  can be determined when the engine r. p. m. is known.

This parameter was obtained by the acoustic equipment shown in Fig. 1. The sound level meter, at the center of the track, responds to the noise of the engine. The signal from it was passed through a 1/3 octave band filter and finally displayed on a counter. Since the engine noise was in the form of a distinct "pop" once per propeller revolution, the electronic counter recorded the number of engine "pops" per second and hence displayed the engine frequency in cps.

## 3. FILM ANALYSIS

### 3.1. Reduction of Data

While in flight, the vehicle was photographed by the movie camera situated at the centerpost (see section 2.2.). The raw data could then be reduced, by a frame-by-frame analysis of the movie film, to produce time histories of the vehicle variables and forward flight speed ( $u = 0$ , see section 4.7). These records, in conjunction with the equations of motion, could then be used to determine the required derivatives.

Film reduction involved the distance measurements of target points  $P_1$ ,  $P_2$ , and  $P_3$  both relative to each other and relative to the ground (see Fig. 6).  $P_2$  is on the harnessing side of the vehicle and is situated in the model's fixed  $X'Y'$  plane (see Fig. 7).  $\bar{Z}_1^+$ ,  $\bar{Z}_2^+$ ,  $\bar{Z}_3^+$ ,  $\bar{X}_1^+$  and  $\bar{X}_3^+$  are the measurements taken from each frame of film analyzed, where + indicates that the measurement is made relative to the reference gridlines of the track (Fig. 1).

The assumptions made for this analysis were:

- 1) The vehicle was stationary during the exposure time of one frame (with an exposure time of 1/1000 secs., displacements in the  $X'$  direction (Fig. 6) were .12 inches for a forward velocity of 10 fps. From an analysis of the flight records (Figs. 18 to 29), angular motions never exceeded  $.02^\circ$  and height motion never exceeded .008 inches during exposure).
- 2) Vehicle angular displacements were small permitting linearization.
- 3) Since the center of gravity distance from the centerpost is large in comparison with the model dimensions, radial translation towards the track center was negligible (less than 1/1000 inches).

Due to parallax; the actual height of  $P_n$ , from film measurements is (Fig. 8),

$$\bar{Z}_n = \frac{R_n}{R+d} (\bar{Z}_n^+ - \bar{h}) + \bar{h} \quad (1)$$

Projecting this point onto the vehicle's unperturbed  $X'Y'$  plane produces a view similar to Fig. 9. Point  $P_n$  is shown for the vehicle's principal axis perturbed from equilibrium.

By geometry

$$R_n = (R + d_n) / \cos(\gamma_n + \gamma)$$

# Contrails

But experimentally,  $\gamma/\gamma_n \ll .03$  where  $\gamma_n \sim 7^\circ$   
 Thus to a good approximation

$$R_n \doteq \frac{R + d_n}{\cos \gamma_n} \quad (2)$$

Substituting equation (2) into (1) produces

$$\bar{Z}_n = \frac{(R + d_n)}{(R + d) \cos \gamma_n} (\bar{Z}_n^+ - \bar{h}) + \bar{h} \quad (3)$$

The geometrical  $X'$  distance (Fig. 9) between  $P_2$  and  $P_n$  is given by  $\Delta X' = (P_n)_{X'} - (P_2)_{X'}$  where  $(P_n)_{X'}$  and  $(P_2)_{X'}$  are the  $X'$  distances from the unperturbed  $Y'$  axis. This becomes

$$\Delta X' = P_n B + \delta x'$$

where  $P_n B \approx (R + d_n) \tan \gamma_n$

Since  $\frac{\delta x'}{P_n B} < .003$ , a good approximation for  $X'$  becomes

$$\Delta X' = \frac{(R + d_n)}{(R + d)} \bar{X}_n^+ \quad \text{where} \quad \bar{X}_n^+ = (R + d) \tan \gamma_n \quad (4)$$

Equations (3) and (4) give parallax and gridline curvature corrections required for the reduction of film data.

Let us now determine some geometrical relationships when the vehicle is perturbed by all the variables. Perturb the  $X'Y'Z'$  axes in height only and let the  $X''Y''Z''$  coordinate system correspond to the vehicle axes perturbed from the above by a pitch, roll and yaw, using the conventional flight-dynamics definitions. The Eulerian relationship between the coordinates of a point in the two reference frames is then given by (Ref. 7)

$$\begin{Bmatrix} X' \\ Y' \\ Z' \end{Bmatrix} = \begin{bmatrix} (\cos \theta \cos \psi), & (\sin \phi \sin \theta \cos \psi - \cos \phi \sin \psi), & (\cos \psi \sin \theta \cos \psi + \sin \phi \sin \psi) \\ (\cos \theta \sin \psi), & (\sin \phi \sin \theta \sin \psi + \cos \phi \cos \psi), & (\cos \phi \sin \theta \sin \psi - \sin \phi \cos \psi) \\ (-\sin \theta), & (\sin \phi \cos \theta), & (\cos \phi \cos \theta) \end{bmatrix} \begin{Bmatrix} X'' \\ Y'' \\ Z'' \end{Bmatrix} \quad (5)$$

# Contrails

By assumption 2, this becomes

$$\begin{Bmatrix} X' \\ Y' \\ Z' \end{Bmatrix} = \begin{bmatrix} 1 & -\psi & \theta \\ \psi & 1 & -\varphi \\ -\theta & \varphi & 1 \end{bmatrix} \begin{Bmatrix} X'' \\ Y'' \\ Z'' \end{Bmatrix} \quad (6)$$

Using equation (6) and the dimensions shown in Fig. 7, we obtain

$$X'_1 = l_1 - l_4 \theta = l_1 \quad \text{where } l_4 \theta / l_1 \ll .002 \quad (\text{See table 1})$$

$$X'_2 = l_6 + l_2 \psi \quad (7)$$

$$X'_3 = -l_3 - l_5 \theta = -l_3 \quad \text{where } l_5 \theta / l_3 \ll .002 \quad (\text{See table 1})$$

$$d_1 = Y'_1 = l_1 \psi + l_4 \varphi$$

$$d_2 = Y'_2 = l_6 \psi - l_2 \varphi \quad (8)$$

$$d_3 = Y'_3 = -l_3 \psi + l_5 \varphi$$

$$Z'_1 = -l_1 \theta - l_4$$

$$Z'_2 = -l_6 \theta - l_2 \varphi \quad (9)$$

$$Z'_3 = l_3 \theta - l_5$$

where the subscripts of the LHS relate to the  $n$  of point  $P_n$ .

Equations (7) give the distances of  $P_n$  from the undisturbed  $Y'$  axis of the vehicle when  $P_n$  is projected onto the undisturbed  $X'Y'$  plane (Fig. 9). Similarly, equations (8) give the  $Y'$  distances of  $P_n$  from the undisturbed  $X'$  axis of the vehicle when  $P_n$  is projected onto the same plane.

Keeping the  $Z$  axis vector in mind (Fig. 6 and equation 5), the signs of equation (9) were changed to produce the height of  $P_n$  above the ground.

These heights are

# Contrails

$$\begin{aligned}
 \bar{Z}_1 &= h_{cg} + l_1 \theta + l_4 + \underline{h} \\
 \bar{Z}_2 &= h_{cg} + l_6 \theta + l_2 \varphi + \underline{h} \\
 \bar{Z}_3 &= h_{cg} - l_3 \theta + l_5 + \underline{h}
 \end{aligned}
 \tag{10}$$

where  $h_{cg}$  is the height of the unperturbed X'Y' plane above the ground and  $\underline{h}$  is the perturbation.

### 3.2. The Symmetrical Parameters

From equation (10), the center of gravity height becomes

$$h_{cg} + \underline{h} = \bar{Z}_1 - l_1 \theta - l_4 \tag{11}$$

On combining the first and third of equations (10)

$$\bar{Z}_1 - l_1 \theta - l_4 = \bar{Z}_3 + l_3 \theta - l_5$$

whence

$$\theta = \frac{\bar{Z}_1 - \bar{Z}_3}{l_1 + l_3} - \frac{(l_4 - l_5)}{(l_1 + l_3)} \tag{12}$$

substituting  $d_1$  and  $d_3$  of equation (8) into equation (3)

$$\begin{aligned}
 \bar{Z}_1 &= \bar{A} + \bar{B} \psi + \bar{C} \varphi \\
 \bar{Z}_3 &= \bar{D} - \bar{E} \psi + \bar{F} \varphi
 \end{aligned}
 \tag{13}$$

where

$$\begin{aligned}
 \bar{A} &= \bar{h} + \frac{R(\bar{Z}_1^+ - \bar{h})}{\cos \gamma_1 (R+d)} & \bar{D} &= \bar{h} + R(\bar{Z}_3^+ - \bar{h}) / \cos \gamma_3 (R+d) \\
 \bar{B} &= \frac{l_1 (\bar{Z}_1^+ - \bar{h})}{\cos \gamma_1 (R+d)} & \bar{E} &= l_3 (\bar{Z}_3^+ - \bar{h}) / \cos \gamma_3 (R+d) \\
 \bar{C} &= l_4 (\bar{Z}_1^+ - \bar{h}) / \cos \gamma_1 (R+d) & \bar{F} &= l_5 (\bar{Z}_3^+ - \bar{h}) / \cos \gamma_3 (R+d)
 \end{aligned}$$



### 3.3. The Antisymmetric Parameters

From equation (7),

$$X'_1 - X'_2 = l_1 - l_0 - l_2 \psi = \Delta X' \quad (14)$$

Substituting equation (4) into (14) ( $d_n = d_1$ )

$$\frac{(R + l_1 \psi + l_4 \varphi) \bar{X}_1^+}{R + d} = l_1 - l_0 - l_2 \psi$$

And on simplification,

$$\psi = \bar{P} \left[ l_1 - l_0 - \frac{R \bar{X}_1^+}{R + d} - \frac{l_4 \bar{X}_1^+}{R + d} \varphi \right] \quad (15)$$

where

$$\bar{P} = (R + d) / (l_2 (R + d) + l_1 \bar{X}_1^+)$$

The second equation of (10) may be rewritten as

$$\varphi = \frac{1}{l_2} \left[ \bar{Z}_2 - h c g - \bar{h} - l_0 \theta \right] \quad (16)$$

By the use of equation (11), equation (16) gives

$$\varphi = \frac{l_4}{l_2} - \frac{1}{l_2} \left[ (Z_1 - Z_2) - (l_1 - l_0) \theta \right] \quad (17)$$

where

$$\bar{Z}_2 = \bar{G} + \bar{\omega} \psi \begin{cases} \bar{G} = \bar{h} + (R - l_2)(Z_2^+ - \bar{h}) / (R + d) \\ \bar{\omega} = l_0 (\bar{Z}_2^+ - \bar{h}) / (R + d) \end{cases}$$

### 3.4. The Track Reduction Equations

When the proper values of  $\bar{Z}_n$  are substituted into equations (12), (15), and (17), one obtains

$$\theta = \frac{(\bar{A} - \bar{D}) + (\bar{B} + \bar{E})\psi + (\bar{C} - \bar{F})\varphi}{l_1 + l_3} - \theta_c \quad (18)$$

$$\varphi = \frac{1}{(l_2 + \bar{C})} \left[ l_2 \bar{H} + (\bar{G} - \bar{A}) + (\bar{W} - \bar{B})\psi + (l_1 - l_6)\theta \right] \quad (19)$$

and

$$\psi = P \left[ l_1 - l_6 - \frac{RX_1^+}{R+d} - \frac{l_4 X_1^+}{R+d} \varphi \right] \quad (20)$$

where  $\bar{H} = l_4 / l_2$  and

$$\theta_c = (l_4 - l_5) / (l_1 + l_3)$$

Equations (18), (19), and (20) form three equations in the unknowns  $\theta$ ,  $\varphi$  and  $\psi$ . All other quantities in these equations are functions of track, model, and movie film measurements.

By substituting equation (20) into (18) and (19) to eliminate  $\psi$ , the resulting two equations can be rearranged to give

$$\theta = \frac{1}{1 - \bar{Q}\bar{S}(l_1 - l_6)} \left[ \bar{T} + \bar{Q}\bar{S}\bar{U} - \theta_c \right] \quad (21)$$

and

$$\varphi = \bar{S} \left[ \bar{U} + (l_1 - l_6)\theta \right] \quad (22)$$

# Contrails

$$\begin{aligned} \text{where } \bar{T} &= \frac{\bar{A} - \bar{D}}{l_1 + l_3} + \frac{(\bar{B} + \bar{E})\bar{P}}{l_1 + l_3} \left[ l_1 - l_6 - \frac{R\bar{X}_1^+}{R+d} \right] \\ \bar{S} &= (R+d) / \left[ (R+d)(l_2 + \bar{C}) + (\bar{\omega} - \bar{B})\bar{P}l_4\bar{X}_1^+ \right] \\ \bar{Q} &= (\bar{C} - \bar{F}) / (l_1 + l_3) - (\bar{B} + \bar{E})\bar{P}l_4\bar{X}_1^+ / (l_1 + l_3)(R+d) \\ \bar{U} &= l_2\bar{H} + (\bar{G} - \bar{A}) + (\bar{\omega} - \bar{B})\bar{P}(l_1 - l_6 - R\bar{X}_1^+ / (R+d)) \end{aligned}$$

Equations (21), (22), (20) and (11) were used to determine  $\theta$ ,  $\varphi$ ,  $\psi$  and  $\underline{h}$  for all film frames analysed. The time histories shown in Figs. 17 to 29 were obtained by plotting the vehicle variables against frame number (Camera speed = 32 frames/sec.).

All computations were performed on the IBM 7090 Computer in the University of Toronto Institute of Computer Science.

## 4. DEVELOPMENT OF THE VEHICLE'S EQUATIONS OF MOTION

### 4.1. Choice of Axes

The axes selected in deriving the equations of motion were the commonly known stability axes (Fig. 10 and Ref. 7) where the X axis points in the direction of flight before the perturbation takes place, with the Y and Z axes as shown (the X', Y', Z' axes are the principle axes). The stability axis forces the reference value of pitch angle to be zero, thus simplifying the equations of motion.

### 4.2. Moments of Inertia

The magnitudes of all moments and products of inertia relative to the body-fixed axes were determined. By means of the bifilar suspension pendulum technique (Ref. 6), A', B', and C', were experimentally measured. Representative values were  $A' = .01 \text{ slugs-ft}^2$ ,  $B' = .04 \text{ slugs-ft}^2$ , and  $C' = .04 \text{ slugs-ft}^2$ .

Estimates of the products of inertia were

$$\begin{aligned} D' &\sim 3 \times 10^{-6} \text{ slugs-ft}^2 \\ E' &\sim 1 \times 10^{-4} \text{ slugs-ft}^2 \\ F' &\sim 3 \times 10^{-6} \text{ slugs-ft}^2 \end{aligned} \tag{23}$$

Since the products of inertia are at least 2 orders of magnitude less than the moments of inertia, we neglected the products of inertia relative to the body fixed axis.

With the vehicle in forward flight at speed  $U_0$  and with a nose up attitude of  $\epsilon$  relative to the stability axis (Fig. 10), the stability axes moments and products of inertia became, upon transforming ( $\epsilon \leq 2^\circ$ ).

$$\begin{aligned} A &= A' \cos^2 \epsilon + C' \sin^2 \epsilon = A' \\ C &= A' \sin^2 \epsilon + C' \cos^2 \epsilon = C' \\ E &= \frac{1}{2} (A' - C') \sin 2\epsilon = \epsilon (A' - C') \\ B &= B' \end{aligned} \tag{24}$$

### 4.3. Linearization of Angular Quantities, Velocities, and Forces

The total pitch and roll rotations of the vehicle can be represented by

$$\begin{aligned}\Theta &= \theta_0 + \theta \\ \Phi &= \phi_0 + \phi\end{aligned}\tag{25}$$

where  $\theta$  and  $\phi$  are the perturbation quantities.

For the stability axes and for horizontal equilibrium flight,  $\theta_0 = 0$ . Furthermore, to minimize the cable derivatives, the tethering height and the centerpost were adjusted so that  $\phi_0 = 0$ .

From Fig. 11, the total yaw angle relative to a reference fixed in space is, when the vehicle is perturbed from equilibrium.

$$\Psi = - \int_0^t \Omega dt + \psi_0 + \psi\tag{26}$$

Preliminary data established that forward velocity perturbation was negligible in comparison with angular perturbations (see section 4.7). Hence  $\Omega$  is constant, and Equation (26) gives

$$\Psi = - \Omega t + \psi_0 + \psi\tag{27}$$

Substituting equations (25) and (27) into the angular velocity relationships (equations A-3 of appendix A) we get after linearization

$$\begin{aligned}P &= \dot{\phi} + \Omega \theta \\ Q &= \dot{\theta} - \Omega \phi \\ R &= -\Omega + \dot{\psi}\end{aligned}\tag{28}$$

Linearized velocity and plunge relationships can be obtained if we examine the motion of the stability axes relative to an earth-fixed reference frame X, Y, Z, (Fig. 11). At some time  $t_n$ , position the origin of the fixed frame of reference at the c. g. of the vehicle and point the X axis in the direction of  $U_0$  and position the X, Y, plane parallel to the vehicle's unperturbed XY plane. Then for  $t = t_n$ , equations A-5 of appendix I give, on linearization

$$U_0 = U\tag{29}$$

$$v = -U\psi \tag{30}$$

$$\frac{dZ_{cg}}{dt} = -U\theta + w$$

But  $Z_{cg} \sim -\underline{h}$

Thus

$$-\frac{1}{U} \frac{d\underline{h}}{dt} = -\theta + \alpha \tag{31}$$

The three velocities, and the forces and moments become

$$\begin{aligned} U &= U_0 \\ V &= -U\psi \\ W &= w \end{aligned} \tag{32}$$

$$\begin{aligned} X &= X_0 + \Delta X \\ Y &= Y_0 + \Delta Y \\ Z &= Z_0 + \Delta Z \end{aligned} \tag{33}$$

$$\begin{aligned} L &= \Delta L \\ M &= \Delta M \\ N &= \Delta N \end{aligned} \tag{34}$$

where the subscripted values indicate equilibrium conditions and  $\Delta$  terms are a linear combination of aerodynamic effects and cable influences ( $L_0 = M_0 = N_0 = 0$  for trimmed flight).

#### 4.4. The Equations of Motion

Substituting equations (24), (25), (27), (28), (32), (33) and (34) into equations A1 and A2 of Appendix I give

$$\begin{aligned}
 \Delta X - mg\theta &= -m\Omega U\psi \\
 \Delta Y &= -mg\varphi \\
 \Delta Z &= m\dot{\omega} - m\dot{\theta}U + m\Omega\varphi U \\
 \Delta L &= A\ddot{\varphi} + [A\Omega - \Omega(C-B) - C_f\omega_f]\dot{\theta} + [\Omega^2(C-B) + \Omega C_f\omega_f]\varphi \\
 \Delta M &= B\ddot{\theta} + [\Omega(C-A) - \Omega B + C_f\omega_f]\dot{\varphi} + [\Omega^2(C-A) + \Omega C_f\omega_f]\theta \\
 \Delta N &= C\ddot{\psi}
 \end{aligned} \tag{35}$$

#### 4.5. Cable Effects (General)

While in flight, the vehicle was harnessed to the centerpost by means of a light line. When the model was perturbed from equilibrium, an impulse was transmitted down the cable and reflected by the centerpost assembly (Fig. 2) back to the model. This reflected disturbance could conceivably interfere with the vehicle's motion (Ref. 4).

The velocity of an impulse, regardless of form, travelling along a cable is given by (Ref. 9).

$$v = \sqrt{\frac{T}{\rho_c}} \tag{36}$$

A signal of the above type arrives back at the vehicle in the time

$$\tau_1 = \frac{2R_c}{v} = 2R_c \sqrt{\frac{\rho_c}{T}} \quad \text{where } T = \frac{mU^2}{R} \tag{37}$$

Since one oscillation of the vehicle is performed in the time

$$\tau_2 = \bar{\lambda}/U_0 \tag{38}$$

the ratio of the two times gives

$$\frac{\tau_1}{\tau_2} = \frac{2R_c}{\bar{\lambda}} \sqrt{\frac{m_c}{m} \left(\frac{R}{R_c}\right)} \tag{39}$$

For minimal cable interaction, this time ratio should be as small as possible corresponding to quasi-static behaviour of the cable. Our dacron line relative to the vehicle's weight produced  $\tau_1/\tau_2 = .02$ . Hence it is concluded that there are no significant effects of cable inertia on the vehicle forces.

## 4.6. Cable Influences on Vehicle Forces

In this investigation, we attached the cable to the side of the vehicle with the centerpost height and harness mechanism adjusted so that the cable lay in the XY plane of the model (Ref. 4). This provided large antisymmetric restoring moments forcing the vehicle to simulate a longitudinal flight path while minimizing the longitudinal cable influences.

In this section, we evaluate the cable effects by applying  $h$ ,  $\varphi$ ,  $\psi$  and  $\dot{h}$  perturbations separately to the vehicle while determining the resulting forces and moments. Differentiating these with respect to the perturbed parameters, then, produces the required derivatives (some of them were first presented in Ref. 4).

The cable angle  $\alpha^*$  (Fig. 12) is non-zero because of cable drag.

### 4.6.1. The Height Effect

The forces and moments exerted on the vehicle by the cable, when there is a perturbation in  $h$  only, are (Fig. 12a)

$$\begin{aligned}
 X^* &= -T \sin \alpha^* \sim -T \alpha^* \\
 Y^* &= -T \cos \alpha^* \cos \zeta \sim -T \\
 Z^* &= T \cos \alpha^* \sin \zeta \sim T \underline{h} / R_c \\
 M^* &= 0 \\
 N^* &= -l_2 T \sin \alpha^* \sim -l_2 T \alpha^* \\
 L^* &= -l_2 \sin \zeta T \cos \alpha^* \sim -l_2 T \underline{h} / R_c
 \end{aligned}$$

whence

$$\begin{aligned}
 Z^*_{\dot{h}} &= \frac{m U^2}{R R_c} \\
 L^*_{\dot{h}} &= -\frac{l_2 m U^2}{R R_c}
 \end{aligned} \tag{40}$$



## 4.6.2. Roll Cable Effects

By perturbing the vehicle in roll (Fig. 12b)

$$\begin{aligned}
 X^* &= -T \sin \alpha^* \sim -T \alpha^* \\
 Y^* &= -T \cos \alpha^* \cos \zeta' \sim -T \\
 Z^* &= T \cos \alpha^* \sin \zeta' \sim \frac{T [R_c + l_2]}{R_c} \varphi \\
 L^* &= -l_2 T \sin \zeta' \cos \alpha^* \sim -\frac{l_2 T [R_c + l_2]}{R_c} \varphi \\
 M^* &= 0 \\
 N^* &= -l_2 T \sin \alpha^* \sim -l_2 T \alpha^*
 \end{aligned}$$

Differentiating these expressions w. r. t.  $\varphi$  gives

$$\begin{aligned}
 Z^*_{\varphi} &= \frac{m U^2}{R R_c} [R_c + l_2] \\
 L^*_{\varphi} &= -\frac{l_2 m U^2}{R R_c} [R_c + l_2]
 \end{aligned} \tag{41}$$

## 4.6.3. The Yaw Cable Effects

The cable yaw effects are illustrated in Figure 12c. The forces and moments are

$$\begin{aligned}
 X^* &= -T \sin(\alpha^* + \zeta') \sim -T \left[ \alpha^* + \frac{(R_c + l_2)}{R_c} \psi \right] \\
 Y^* &= -T \cos(\alpha^* + \zeta') \sim -T \\
 Z^* &= L^* = M^* = 0 \\
 N^* &= -l_2 T \sin(\alpha^* + \zeta') \sim -l_2 T \left[ \alpha^* + \frac{(R_c + l_2)}{R_c} \psi \right]
 \end{aligned}$$

whence

$$\begin{aligned}
 X^*_{\psi} &= -\frac{m U^2}{R R_c} [R_c + l_2] \\
 N^*_{\psi} &= -\frac{l_2 m U^2}{R R_c} [R_c + l_2]
 \end{aligned} \tag{42}$$

#### 4.6.4. The h Cable Derivatives

From equation 31, perturbing the vehicle by an h is equivalent to flying the vehicle with an angle of attack  $\alpha = -\frac{1}{U} \dot{h}$

From Fig. 12d

$$\begin{aligned} X^* & \doteq T\alpha^* \\ Y^* & \doteq -T \\ Z^* & \doteq \frac{T\alpha^*}{U} \dot{h} \\ L^* & \doteq -l_2 \frac{T\alpha^*}{U} \dot{h} \\ M^* & = 0 \\ N^* & = -l_2 T\alpha^* \end{aligned}$$

By differentiation, these become

$$Z_{\dot{h}}^* = \frac{T\alpha^*}{U} \quad L_{\dot{h}}^* = -l_2 \frac{T\alpha^*}{U} \quad (43)$$

where  $\alpha^* \sim .02^\circ$  (Ref. 4). These derivatives were found to be negligibly small (see Table 3) and hence were dropped from the equations of motion.

The nondimensional values of all the cable derivatives are presented in Table 3.

#### 4.7. The Air Reactions

The assumptions made in obtaining the air reactions were

- 1) The vehicle was rigid (no aeroelastic terms).
- 2) Fixed controls.
- 3) The aerodynamic forces and moments were functions of the instantaneous values of the velocities, perturbation angles and their derivatives. We thus expanded the reactions in a Taylor series about the unperturbed or equilibrium state and assumed that all but 3 of the nonlinearities were negligible. Since experimental tests (both lamp black and curtain probing - see Ref. 6) indicated that the model plus curtain configuration were symmetrical, the longitudinal reactions, when differentiated with respect to the antisymmetrical motion parameters, became zero and vice versa. We excluded  $Z_\phi$  from this assumption for reasons given below.

- 4) All derivatives with respect to acceleration were assumed to

be negligible as in Reference 7.

The Aerodynamic reactions then become

$$\begin{aligned}
 \Delta X &= X_{\theta} \theta + X_q q + X_{\dot{h}} \dot{h} + X_{\dot{\psi}}^* \dot{\psi} \\
 \Delta Z &= Z_{\theta} \theta + Z_q q + (Z_h + Z_h^*) h + Z_{\dot{h}} \dot{h} + (Z_{\dot{\psi}}^* + Z_{\psi}) \dot{\psi} + Z_{h\dot{h}} h^2 \\
 \Delta M &= M_{\theta} \theta + M_q q + M_h h + M_{\dot{h}} \dot{h} + M_{\theta\dot{h}} \theta \dot{h} \\
 \Delta Y &= Y_{\psi} \psi + Y_p p + Y_{\dot{\psi}} \dot{\psi} + Y_r r \\
 \Delta L &= (L_{\psi} + L_{\dot{\psi}}^*) \dot{\psi} + L_p p + L_{\dot{\psi}} \dot{\psi} + L_r r + L_h^* h + L_{\psi\dot{h}} h \dot{\psi} \\
 \Delta N &= N_{\psi} \psi + N_p p + (N_{\dot{\psi}} + N_{\dot{\psi}}^*) \dot{\psi} + N_r r
 \end{aligned}
 \tag{44}$$

where the unstarred quantities are model derivatives and the starred quantities are cable effects.

A comparison of equations 44 with the aerodynamic reactions of a conventional airplane (Ref. 7) reveals one important difference between the two, namely the existence of the  $\theta$ ,  $\psi$ , and  $\dot{\psi}$  terms and the apparent lack of angle of attack contributions in the above.  $C_{m\alpha}$  is the "static stability" derivative of an airplane in flight. This is not, however, an adequate criterion for the Air Cushion Vehicle in close proximity to ground. We can illustrate this by examining the  $C_{m\alpha} \alpha$  of our model (Eq. 31). We could perturb the angle of attack  $\alpha$  by maintaining zero pitch and slowly plunging the vehicle or, restricting the vehicle to a constant height, slowly changing pitch. By plunging the vehicle (for  $\theta = 0$ ), the  $C_{m\alpha} \alpha$  exerted on the model would be due to an adjustment of the pressure field on the external surface of the model-plus-curtain configuration. When  $\dot{h} = 0$  and the vehicle is perturbed in pitch, the principal contribution to  $C_{m\alpha} \alpha$  becomes the strong restoring torque  $C_{m\theta} \theta$  (Refs. 2, 6 and 12) exerted by the internal cushion air. For this reason, the conventional  $\alpha$  notation is not used, and the static stability derivative is specified by  $C_{m\theta}$ . Angle of attack reactions, then can be thought of as a combination of  $\theta$  and  $\dot{h}$  reactions.

Many of the derivatives in equation 44 were estimated to be sizeable from the data of References 2, 6 and 13 or by the theoretical approach presented in Appendix B. The magnitudes of  $Z_{\psi}$ ,  $M_h$ ,  $M_{\dot{h}}$ ,  $L_{\dot{\psi}}$ ,  $L_r$ ,  $Y_{\dot{\psi}}$ ,  $Y_r$ ,  $N_{\psi}$ ,  $N_p$ ,  $N_{\dot{\psi}}$  and  $N_r$ , however, could not be determined from the available information. We justified the inclusion of  $Z_{\psi}$  on the following grounds. Perturbing the vehicle in roll while in flight could alter the curtain geometry slightly. This could force

# Contrails

a weak portion of the curtain into operating in the underfed condition Fig. 42(b) creating a base pressure leak which in turn would produce a reaction in the Z direction. We assumed, however, that changes in curtain geometry were not excessive enough to violate the symmetry assumption (see above). A similar argument can be presented for  $C_{m\dot{H}}$  and  $C_{m\ddot{H}}$ ; lacking curtain symmetry, the vehicle, while in plunge, could be induced to pitch. Since their magnitudes were unknown, the above unestimateable derivatives could not be discarded. By deducing them experimentally, we can determine whether any of these are negligible or not.

Certain contributions, functions of our experiment only, were not included in Equation 44. By a frame by frame movie analysis of the vehicle's progress around the track, we found that  $v/U \leq .005$ . Since this is second order in comparison to the other variables, the velocity terms were neglected. Since  $\Delta T^*/J \leq .005$ , the cable tension term in the Y equation was also neglected. The calibration and measurement of the engine cps (see section 2.5) indicated that engine frequency was accurate to within .44%. By Reference 6, this produced negligible fluctuations in jet momentum flux, on comparing this variable with  $h$ ,  $\theta$ ,  $\phi$  and  $\psi$  ( $\Delta J/J \leq .009$ ). Finally,  $Z^*_{\dot{h}}$  and  $L^*_{\dot{h}}$  were not included in equations (44) since these are orders of magnitude less than any of the other derivatives (see Table 3).

Since  $v/U$  is negligible, the X equation of equations(35) can be excluded from the set (Ref. 7). The variable  $\Delta T^*/J$  appears, in the Y equation only. With  $\Delta T^* \sim 0$ , this equation is also deleted. Thus substituting equations (44), (29), and (28) into (35) gives

$$[V] \begin{Bmatrix} h \\ \theta \\ \phi \\ \psi \end{Bmatrix} = 0 \quad (45)$$

where

$$\begin{aligned}
 & \left[ Z_h + Z_h^* + (Z_h^*) \frac{d}{dt} + (m) \frac{d^2}{dt^2} + Z_{hh} \frac{d}{dt} \right], [Z_\theta + Z_{q\theta} \frac{d}{dt}], [Z_\varphi + Z_\varphi^* - m \Omega U - Z_{q\Omega}], \quad 0 \\
 & \left[ M_h + M_h^* \frac{d}{dt} \right], [M_\theta + M_{\theta h} - \Omega^2 (C-A) - \Omega C_f \omega_f + M_{q\theta} \frac{d}{dt} + (-B) \frac{d^2}{dt^2}], [-\{\Omega M_q + \Omega (C-A) - \Omega B + C_f \omega_f\} \frac{d}{dt}], 0 \\
 & \left[ L_h^* \right], [\Omega L_p + \{\Omega A + \Omega (C-B) + C_f \omega_f\} \frac{d}{dt}], [L_\varphi + L_{\varphi h} - \Omega^2 (C-B) - \Omega C_f \omega_f + L_{p\varphi} \frac{d}{dt} + (-A) \frac{d^2}{dt^2}], [L_\psi + L_{r\psi} \frac{d}{dt}] \\
 & 0, [\Omega N_p], [N_\varphi + N_p \frac{d}{dt}], [N_\psi + N_\psi^* + N_r \frac{d}{dt} + (-C) \frac{d^2}{dt^2}]
 \end{aligned}$$

From matrix  $[V]$ , one can easily see how the longitudinal and antisymmetric equations are coupled. Excluding  $Z_\varphi$ , there are cable terms, gyro terms, and circular flight path coupling components.

## 4.8. Ground Roughness Input

Since the ACV is always (excluding GETOL airplanes) in the presence of the earth's surface, ground roughness, if present, provides an input to the air cushion's dynamic system. This perturbing influence is analogous to that of a vertical gust input for the conventional aircraft. The airplane can be influenced by a constant gust, sinusoidal gust or atmospheric turbulence while the ACV may pass over steps, waves, slopes or rough surfaces (flight over disturbed water).

Let us take the arguments presented in References 10 and 12 and apply them in representing ground roughness. Namely, let the ground under the vehicle be represented by the Taylor series

$$h_s = (h_s)_0 + \left( \frac{\partial h_s}{\partial \hat{x}_i'} \right) \hat{x}_i' + \frac{1}{2!} \left( \frac{\partial^2 h_s}{\partial \hat{x}_j' \partial \hat{x}_i'} \right) \hat{x}_i' \hat{x}_j' \quad (46)$$

$$\begin{aligned} i &= 1, 2 \\ j &= 1, 2 \end{aligned}$$

where the subscript 0 denotes the vehicle c. g. i. e. the point  $(U_{0t}, 0, h_e$  - see Fig. 13). The contention is that the vehicle is perturbed by the input  $h_s$  with each term of equation (46) resulting in an aerodynamic reaction. Equation (45) becomes

$$[V] \begin{Bmatrix} \hat{h} \\ \hat{\theta} \\ \hat{\varphi} \\ \hat{\psi} \end{Bmatrix} = [\hat{F}] \quad (47)$$

where

$$\{\hat{F}\} = [G_s] \{H_s\}$$

and

$$\{H_s\} = \begin{bmatrix} (h_s)_0 \\ h_{sx} \\ h_{sy} \\ h_{sx}^2 \\ h_{sx}h_{sy} \\ h_{sy}^2 \\ (h_s)_0^2 \\ h_{sx}(h_s)_0 \\ h_{sy}(h_s)_0 \end{bmatrix}$$

$$[G_s] = \begin{bmatrix} Z_{h_s}, Z_{h_{sx}}, Z_{h_{sy}}, Z_{h_{sx}^2}, Z_{h_{sx}h_{sy}}, Z_{h_{sy}^2}, Z_{h_s^2}, 0, 0 \\ M_{h_s}, M_{h_{sx}}, 0, M_{h_{sx}^2}, 0, 0, 0, 0, M_{h_{sx}h_{sy}}, 0 \\ 0, 0, 0, L_{h_{sx}}, 0, 0, 0, L_{h_{sy}}, 0, 0, L_{h_{sx}h_{sy}} \\ 0, 0, 0, N_{h_{sx}}, 0, 0, 0, N_{h_{sy}}, N_{h_{sx}h_{sy}}, 0, 0 \end{bmatrix}$$

Where certain elements of  $[G_s]$  are set to zero by virtue of assumption 3 -  $Z_{h_{sx}h_{sy}}$  and  $Z_{h_{sy}^2}$  are retained following the arguments presented for  $Z_{\phi}$  above.

The elements of  $G_s$  are aerodynamic derivatives and some of these can be related to those presented in equation (44). For example, the Z reaction exerted on the vehicle is the same if we plunge the vehicle towards the ground ( $h_s = 0$ ), or bring the ground up towards the vehicle. Thus  $Z_h = -Z_{hs}$  and  $Z_{hh} = -Z_{hshs}$ . Similarly,  $M_h = -M_{hs}$ . Similarly, a slope in the ground typified by  $h_s \hat{x}$  would exert a strong restoring torque on the vehicle tending to force the vehicle's X'Y' plane to be parallel to the ground. Thus  $M_{hs \hat{x}} = -M_\theta$  and  $L_{hs \hat{y}} = -L_\varphi$ . One can also verify that  $M_{hshs \hat{x}} = -M_{h\theta}$ ,  $L_{hs \hat{y}} = -L_\varphi$  and  $N_{hs \hat{y}} = -N_\varphi$ .

At this moment, the curvature derivatives, those containing the double subscripts,  $\hat{X}\hat{X}$ ,  $\hat{X}\hat{Y}$  and  $\hat{Y}\hat{Y}$ , cannot be simply related to any of the derivatives in equation (44) (i. e.  $Z_{hs \hat{X}\hat{X}}$  to  $Z_q$  etc.), for the following reasons. During vehicle perturbations when  $\{H_s\} = 0$ , the cushion continually strikes a flat ground while if  $h_s \hat{X}\hat{X}$  or  $h_s \hat{Y}\hat{Y}$  are non-zero the cushion strikes a curved surface; there could be a significant difference in certain behaviour between these two situations, there being no information available about the latter.

In the case of the gust velocity field (Ref. 10 and 12), the theory assumes that the wave lengths of all significant spectral components of a gust are larger than twice the corresponding dimensions of the aircraft. We expect the same assumption to apply here; namely, that the ground wavelengths on the two axes ( $\hat{X}_1, \hat{X}_2$ ) should exceed twice that of the equivalent diameter.

By including Matrix  $[\hat{F}]$  in equation (45), at least 17 extra derivatives, above those existing in matrix  $[V]$ , must be determined. Since the errors involved in deducing any derivatives are a direct function of the number of derivatives involved (see Sections 5 and 6) our experiment was conducted with  $[\hat{F}] = 0$ .

After finding the coefficients of  $[V]$  by an experiment such as described herein, further experiments over a wavy ground surface could in principle yield the coefficients of  $[G_s]$ . Such experiments were beyond the scope of this investigation.

#### 4. 9. The Nondimensional Equations

In the literature, information about aerodynamic derivatives is usually presented in non-dimensional form. The major problem for ACV's is that a proper nondimensionalizing quantity must be selected. If the forces are divided by the usual  $\frac{1}{2} \rho U^2$  the derivatives become infinite at  $U = 0$ . If  $(J + \frac{1}{2} \rho U^2 \cdot S)$  is used as in Ref. 13, the coefficients vary nonlinearly both with pitch and  $q/q_J$ .

When an ACV is harnessed rigidly at some specific height, lift is



# Contrails

directly proportional to jet momentum flux (Ref. 2 and 3). J was thus used to nondimensionalize lift. Table 2 lists the dimensional quantities, the divisors and the nondimensional quantities. On use of this table the nondimensional equations become, (for  $[\hat{F}] = 0$ )

$$[\nabla] = \left\{ \begin{array}{c} H \\ \theta \\ \varphi \\ \psi \end{array} \right\} = 0 \quad (48)$$

where

$$\begin{aligned}
 & \left[ C_{ZH} + C_{ZH}^* + (C_{ZH}) \hat{D} + (\mu) \hat{D}^2 + C_{ZH} H \right], [C_{Z\varphi} + C_{Z\varphi}^*], \left[ C_{Z\varphi} + C_{Z\varphi}^* - \frac{D_{eq} U_0}{R} \frac{C_{Zq}}{V_J} \right], 0 \\
 & \left[ C_{NH} + C_{NH} \hat{D} + C_{NH} \theta \right], \left[ C_{M\theta} - \frac{D_{eq}^2 q}{R^2 q_J} (i_c - i_q) - \frac{D_{eq} U_0}{R} \frac{i_c i_q}{V_J} + C_{Mq} \hat{D} + (-i_b) \hat{D}^2 \right], \left[ \left[ \frac{D_{eq} U_0}{R} \frac{C_{Mq}}{V_J} + C_{Mq} \right] \hat{D} \right], 0 \\
 & \left[ C_{\theta H}^* \right] \left[ \frac{D_{eq} U_0}{R} \frac{C_{\theta\varphi}}{V_J} + \left( \frac{D_{eq} U_0}{R} \frac{i_c - i_q}{V_J} + i_c i_q \right) \hat{D} \right], \left[ C_{\theta\varphi} + C_{\theta\varphi}^* - \frac{D_{eq}^2 q}{R^2 q_J} (i_c - i_b) - \frac{D_{eq} U_0}{R} \frac{i_c i_q}{V_J} + C_{\theta H} \hat{D} + (-i_q) \hat{D}^2 \right], [C_{\theta\varphi} + C_{\theta\varphi}^* \hat{D}] \\
 & 0, \left[ \frac{D_{eq} U_0}{R} \frac{C_{NP}}{V_J} \right], [C_{N\varphi} + C_{NP} \hat{D}], [C_{N\varphi} + C_{N\varphi}^* + C_{NP} \hat{D} + (-i_c) \hat{D}^2]
 \end{aligned}$$

## 5. DERIVATIVE EXTRACTION TECHNIQUE

### 5.1. Introduction

By applying the analysis of Section 3 to the film measurements, we experimentally determined the vehicle's variables as functions of time. In Section 4, we developed the equations of motion. By substituting the flight records into the equations of motion, we can deduce the magnitudes of the flight derivatives. The mathematical analysis, however, can be done by many different analytical techniques (Refs. 14 to 20). Thus, a study had to be performed to determine which specific method was most suitable for our application.

This survey was conducted using the simple equation

$$a\ddot{\chi} + b\dot{\chi} + c\chi = f(t) \quad (49)$$

Given  $F(t)$ , the various techniques can be applied and  $a$ ,  $b$ , and  $c$ , determined. By comparing the various deduced  $a$ ,  $b$  and  $c$ 's with known values, an accuracy evaluation can be made.

### 5.2. A Survey of the Techniques

The frequency domain or transfer function method (Ref. 17 and 18) was discarded immediately since it cannot be applied to a nonlinear system. The power in this technique lies in the fact that  $\mathcal{L}[\dot{\chi}] = S\{\mathcal{L}[\chi]\}$  where  $\mathcal{L}$  is the Laplacian operator. Such a simple relationship does not exist for nonlinearities (i. e.  $C_{ZHH} H^2$ ,  $C_{M\theta H} \theta H$  and  $C_{L\varphi H} \varphi H$  of equation 46). This then leaves the time domain methods (Refs. 14 and 16) as the only means for an analytical solution. As Shinbrot (Ref. 14) illustrated, this family of techniques are similar to the following. Each method multiplies equation (49) by a weighting function  $Y_\nu(t)$  and integrates with respect to time producing

$$a \int_0^t Y_\nu(t) \ddot{\chi} dt + b \int_0^t Y_\nu(t) \dot{\chi} dt + c \int_0^t Y_\nu(t) \chi dt = \int_0^t Y_\nu(t) f(t) dt. \quad (50)$$

where  $a$ ,  $b$ , and  $c$  are considered to be constants.

For  $Y_\nu = e^{-st}$  and  $t$  varying from 0 to  $\infty$ , we have the Laplace method which can be converted into the Fourier technique by letting  $s = i\omega$ . The derivative method is obtained when  $Y_\nu = \dot{\chi}$  forming one equation. By letting  $Y_\nu = \dot{\chi}$  and finally  $Y_\nu = \chi$  we obtain 3 equations in all, for the 3 unknowns  $a$ ,  $b$  and  $c$  ( $0 \leq t \leq \infty$ ). When  $Y_\nu(t) = \sin \omega_\nu^n t$ , we have the Shinbrot technique and finally with  $Y_\nu(t) = 1$  we have the unit weight method.

The survey of the literature (Ref. 14 to 20) indicated that the Laplace method was inferior to the Fourier technique (Ref. 14) and that the Shinbrot method became very inaccurate when applied to equations more complicated than equation (49) (Ref. 15). This reduced the number of available analytical techniques to three; namely, the Fourier, the derivative and the unit weight methods. Our flight records, however, eliminated the derivative method. In the experiment, only displacements were measured (i. e.  $\chi(t)$  for Equation 49). Consequently, if  $\dot{\chi}(t)$  or  $\ddot{\chi}(t)$  are required, a mathematical differentiation of  $\chi(t)$  must be performed. The errors in numerically determining  $\dot{\chi}(t)$  and  $\ddot{\chi}(t)$  would create large inaccuracies in a, b and c.

We examine the remaining 2 techniques. The Fourier technique has been used successfully in determining derivatives (Ref. 16, 20 and 22) and, as such, had to be tested (see section 5.1). The unit weight technique, however, presented some problems. Let us illustrate these by developing the method completely. Integrating equation (50) with respect to time ( $\gamma_p = 1$ ) or doubly integrating equation (49) (w. r. t. time) produces

$$a \left[ \chi(t) - \chi(0) - \dot{\chi}(0)t \right] + b \left[ \int_0^t \chi dt - \chi(0)t \right] + c \int_0^t \int_0^v \chi(u) du dv \quad (51)$$

$$= \int_0^t \int_0^v f(u) du dv$$

The following procedure is then followed. We let t, in the upper limit of the integral, equal  $t_1, t_2, \dots, t_n, \dots, t_N$  and then substitute the  $\chi(t)$  time history into equation (51) (see Fig. 14 for a typical record); we thus obtain N equations. The method of least squares is then used (Ref. 23) and the number of equations reduced to the required 3 for a, b and c in the usual manner.

The first difficulty lies in the coefficient of "a" (Eq. 51). For  $t = t_1$ , and  $\chi(0) = 0$  this quantity becomes  $\chi(t_1) - \chi(0) \Delta t$  while, for  $t = t_N$ , we obtain  $\chi(t_N) - \chi(0) N \Delta t$  (Fig. 14). We see that the  $\chi(0)$  term becomes increasingly important until it is completely dominant in this coefficient (i. e. at  $t = t_N$  where  $\chi(t_N) = 0$ , point G of Figure 14). An error in numerically evaluating  $\chi(0)$  could, then, result in huge errors in the deduced values of a, b and c.

The second difficulty lies in evaluating the integrals. When deducing  $\int_0^t \chi dt$  for each equation, the first part of the flight record is used most often while that element of record between  $t_{N-1}$  and  $t_N$  is used just once, namely in the last equation; the final results are weighted in favor of the initial part of the flight record.

The final difficulty arises from use of the double integral. Our flight record measurements (see section 3) consist of  $\chi_{total}(t) = \chi_e(t) + \underline{\chi}(t)$  where  $\chi_e(t)$  is the equilibrium value (i. e. equilibrium height above the ground).

We then deduce  $\underline{\chi}(t)$ , the perturbed value, by subtracting  $\chi_e(t)$  from  $\chi_{total}(t)$ . If, due to experimental scatter, an error is made in the evaluation of  $\chi_e(t)$ , the first integral of our deduced perturbation becomes  $\int_0^t \chi(t) dt \pm (\Delta\chi)t$  where  $\Delta\chi$  is the error (either positive or negative). And the error in the double integration becomes  $\pm(\Delta\chi)t^2/2$ . This drift, especially if  $t$  is quite large, could produce large errors in our deduced derivatives.

As a result of this, we revised the unit weight technique to form the finite difference method. Performing the second integration from  $t - t_{n-1}$  to  $t_n$  instead of from 0 to  $t$  in equation (51) results in (Fig. 14)

$$\begin{aligned}
 a \left[ \chi(t_n) - \chi(t_{n-1}) - \dot{\chi}(0) \Delta t \right] + b \left[ \int_{t_{n-1}}^{t_n} \int_0^t \chi(u) du dt - \chi(0) \Delta t \right] \\
 + c \int_{t_{n-1}}^{t_n} \int_0^t \chi(u) du dt = \int_{t_{n-1}}^{t_n} \int_0^t f(u) du dt
 \end{aligned} \tag{52}$$

where  $\Delta t = t_n - t_{n-1}$

and  $N$  equations are obtained when (52) is applied successively to the intervals 0 to  $t_1$ ,  $t_1$  to  $t_2$ , ...,  $t_{n-1}$  to  $t_n$ , ...,  $t_{N-1}$  to  $t_N$  of  $\chi(t)$ . When  $t_n - t_{n-1}$  is kept constant, the  $\chi(0) (t_n - t_{n-1})$  term in coefficient "a", does not increase with time as above. Since the equation is applied to  $t_n - t_{n-1}$  of the record, each part of  $\chi(t)$  bears equal weight, and finally drift seems to be small (for the first integral -  $\Delta\chi(t_n - t_{n-1})$  and for the second integral  $\pm \frac{\Delta\chi}{2}(t_n^2 - t_{n-1}^2)$ ).

Dr. D. G. Gould of NAE suggested another revision to the unit weight method. If the first equation of (51) (0 to  $t_1$ ) is multiplied by  $t_N$ , the second equation (0 to  $t_2$ ) by  $t_{N-1}$  etc., the final set of equations would be weighted in such a manner as to reduce the contribution of  $\chi(0)t$  to coefficient "a". Let us call this revision the weighted unit weight technique.

### 5.3. A Comparison of the 4 Selected Methods

We then decided that a test had to be performed to determine which of the above techniques (Fourier, unit weight, finite difference or weighted unit weight) was most suitable for the ACV's equations of motion. The equation selected for the test was

$$\ddot{\chi} + 3.6 \dot{\chi} + 36 \chi = 0 \tag{53a}$$

The exact solution, to equation 53a, was taken and programmed for the digital computer. The output values were deduced at the same time intervals as the

movie camera's recording rate, and the results are shown in Figure 14, the coefficients  $a = 1$ ,  $b = 3.6$ , and  $c = 36$  were selected so that the damping and natural frequency of the theoretical output were roughly similar to that of the track data (Fig. 14).

The manner of testing was as follows. We assumed that the computed  $\chi(t)$  history of Fig. 14 was given. We further assumed that the equation producing this output was

$$\ddot{\chi} + b\dot{\chi} + a\chi = 0 \quad (53)$$

We then applied the 4 techniques to equation (53) and, using the  $\chi(t)$  of Fig. 14, determined the values of  $b$  and  $a$ . A comparison of the deduced  $b$  and  $a$  with  $b = 3.6$  and  $a = 36$  of equation (53a) yielded the accuracy of that particular method.

Other factors considered in this analysis were:

- 1) The effect of a small change in  $\dot{\chi}(0)$  on the final results (a 10% error in  $\dot{\chi}(0)$  can easily occur if one graphically determines this initial condition by means of a straight edge and Fig. 14).
- 2) The effect of initiating the integration at a minimum initial velocity point (i. e. B) - a minimum  $\dot{\chi}(0)$  might improve the deduced values of  $a$  and  $b$ .
- 3) The effect of scatter in the raw data,  $\chi(t)$ , on the final results - this included an examination of whether retaining a portion of the record after point G in Fig. 14, or whether presmoothing the  $\chi(t)$  data improved the final results.

The numerical integrations required for this study were performed as follows. Since a wavelength of the output is defined by approximately 32 data points, a trapezoidal evaluation of  $\int_{t_i}^{t_n} \chi dt$  was adequate (the error between the exact solution and the approximate trapezoidal approximation never exceeded 1% provided that the  $\Delta t$  shown in Fig. 14 never exceeded 1/32 of a second).

Thus

$$\int_{t_{n-1}}^{t_n} \chi(t) dt = \left[ \frac{\chi(t_n) + \chi(t_{n-1})}{2} \right] \Delta t = J_n^{\chi} \quad (54)$$

For the unit weight technique (eq. 51)

$$\int_{t_i}^{t_N} \chi(t) dt = \sum_{i+1}^N J_n^{\chi} \quad (55)$$

In Fig. 14, let  $t_i = t_1$  and  $t_N = t_4$ , for example. One can easily prove that

$$\int_{t_3}^{t_4} \int_{t_3}^t \chi(u) du dt = \left[ J_2^{\chi} + J_3^{\chi} + \frac{1}{2} J_4^{\chi} \right] \Delta t.$$

when we double integrate  $\chi(t)$ . Rewriting this in a more general form

$$\int_{t_{N-1}}^{t_N} \int_{t_i}^t \chi(u) du dt = \left[ \sum_{i+1}^{N-1} J_n^{\chi} + \frac{1}{2} J_N^{\chi} \right] \Delta t = \overline{J}_N^{\chi} \quad (56)$$

whence

$$\int_{t_i}^{t_N} \int_{t_i}^t \chi(u) du dt = \sum_{i+1}^N \overline{J}_n^{\chi} \quad (57)$$

Equations 54 and 56 were used for the finite difference technique while equations 55 and 57 were used in the other methods (in the Fourier technique,  $\chi(t)$  is multiplied by a trigonometric quantity before the summing procedure is initiated - see equation 63).

An artificial device was used to introduce scatter to the  $\chi(t)$  time history (see equation 53a). The University of Toronto Institute of Computer Science has a library program that generates random numbers following the Gaussian or Normal distribution; the standard deviation  $\sigma$  is unity. By generating a set of these numbers and dividing each by a number  $L$ , the standard deviation of the computed random numbers became  $1/L$ . By properly selecting  $L$  and then adding the altered random numbers to the exact computed output of equation (53a), we obtained a simulated experimental  $\chi(t)$  time history where the third, second or first significant figure was changed, at will, by the Gaussian error. An illustration of this is provided by the points in the lower part of Fig. 14 ( $\sigma = 1/L = .00275$ ).

For presmoothing the "experimental"  $\chi(t)$  time history, the moving arc

method was used (Ref. 26). This technique employs a series of polynomial least-squares arcs, each of which smooths only the midpoint of the arc by using a limited number of points disposed symmetrically about it (7 points of Fig. 14 say). The arc "moves" by dropping one point from the left end and adding the next successive point on the right end; the process yields a curve without sudden fluctuations. Furthermore, this approach deduces a least squares evaluation of the initial velocity  $\dot{\chi}(t_i)$ . From examining Fig. 14, we see that a parabola adequately describes any portion of the curve described by a series of 7 points (i. e.  $\chi(t)$  for  $t_n - 7$  to  $t_n$ ). We thus used the parabola-to-seven-point smoothing in determining the least squares time history of  $\chi(t)$ .

The unit weight, weighted unit weight, finite difference and Fourier methods were applied to equation (53). The actual procedures in utilizing the  $Y_\mu = 1$  method and all its revisions have already been discussed in developing equations (51) and (52) - see also the discussion preceding section 5.3. The Fourier equations are now presented for completeness.

Integrating by parts, one can show that

$$\int_{t_i}^{t_N} Y_\mu \dot{\chi} dt = Y_\mu(t_N)\chi(t_N) - Y_\mu(t_i)\chi(t_i) - \int_{t_i}^{t_N} \dot{Y}_\mu \chi dt$$

$$\int_{t_i}^{t_N} Y_\mu \ddot{\chi} dt = Y_\mu(t_N)\dot{\chi}(t_N) - Y_\mu(t_i)\dot{\chi}(t_i) - \dot{Y}_\mu(t_N)\chi(t_N) + \dot{Y}_\mu(t_i)\chi(t_i) + \int_{t_i}^{t_N} \ddot{Y}_\mu \chi dt$$
(58)

when  $Y_\mu = e^{-i\omega t}$  (59)

these become

$$\int_{t_i}^{t_N} Y_\mu \dot{\chi} dt = \chi(t_N)\cos\omega t_N - \chi(t_i)\cos\omega t_i + \omega \int_{t_i}^{t_N} \chi(t)\sin\omega t dt + i \left[ \chi(t_i)\sin\omega t_i - \chi(t_N)\sin\omega t_N + \omega \int_{t_i}^{t_N} \chi(t)\cos\omega t dt \right]$$

$$\int_{t_i}^{t_N} Y_\mu \ddot{\chi} dt = \dot{\chi}(t_N)\cos\omega t_N - \dot{\chi}(t_i)\cos\omega t_i + \omega \chi(t_N)\sin\omega t_N - \omega \chi(t_i)\sin\omega t_i - \omega^2 \int_{t_i}^{t_N} \chi(t)\cos\omega t dt + i \left[ \dot{\chi}(t_i)\sin\omega t_i - \dot{\chi}(t_N)\sin\omega t_N + \chi(t_N)\omega \cos\omega t_N - \chi(t_i)\omega \cos\omega t_i + \omega^2 \int_{t_i}^{t_N} \chi(t)\sin\omega t dt \right]$$
(60)

Multiplying equation (53) by equation (59) and integrating from  $t_i$  to  $t_N$  (see Fig. 14)



$$\int_{t_i}^{t_N} Y_{\nu} \ddot{\chi} dt + b \int_{t_i}^{t_N} Y_{\nu} \dot{\chi} dt + a \int_{t_i}^{t_N} Y_{\nu} \chi dt = 0 \quad (61)$$

Substituting equations (58) into (61) finally produced

$$\begin{aligned} a A \omega + b B \omega &= C \omega \\ a A' \omega + b B' \omega &= C' \omega \end{aligned} \quad (62)$$

where

$$\begin{aligned} -C \omega &= \dot{\chi}(t_N) \cos \omega t_N - \dot{\chi}(t_i) \cos \omega t_i + \omega \chi(t_N) \sin \omega t_N \\ &\quad - \omega \chi(t_i) \sin \omega t_i - \omega^2 \int_{t_i}^{t_N} \chi(t) \cos \omega t dt . \\ -C' \omega &= \chi'(t_i) \sin \omega t_i - \dot{\chi}(t_N) \sin \omega t_N + \chi(t_N) \cos \omega t_N \\ &\quad - \chi(t_i) \omega \cos \omega t_i + \omega^2 \int_{t_i}^{t_N} \chi(t) \sin \omega t dt . \\ B \omega &= \chi(t_N) \cos \omega t_N - \chi(t_i) \cos \omega t_i + \omega \int_{t_i}^{t_N} \chi(t) \sin \omega t dt . \\ B' \omega &= \chi(t_i) \sin \omega t_i - \chi(t_N) \sin \omega t_N + \omega \int_{t_i}^{t_N} \chi(t) \cos \omega t dt . \\ A \omega &= + \int_{t_i}^{t_N} \chi(t) \cos \omega t dt . \\ A' \omega &= - \int_{t_i}^{t_N} \chi(t) \sin \omega t dt . \end{aligned} \quad (63)$$

The least squares technique reduces the equations of (62) to the required 2.

Two distinct advantages are self-evident when this technique is examined. Firstly, at  $t_N$  (Fig. 14),  $\chi(t_N) = \dot{\chi}(t_N) = 0$  and each equation developed, by letting  $\omega = \omega_1, \omega_2, \dots, \omega_N$ , gives equal weight to the whole record. Secondly, only one integration is required eliminating the problem of parabolic drift.

## 5.4. Selection of the Most Appropriate Technique

Figure 15 presents the effect of scatter in the  $\chi(t)$  data. One can see that the finite difference technique is inferior to the other methods when more than the third significant figure of the raw data ( $\chi(t)$ ) was in error. Even presmoothing (for  $\sigma \geq .000275$ ) the output did not produce the accuracies in coefficients that the other techniques produced. An explanation of this may be that the scatter, though small in comparison to  $\chi(t_n)$ , becomes extremely large in comparison to  $\chi(t_n) - \chi(t_n - 1)$ .

The Fourier and weighted unit weight techniques were approximately .5% to 2% more accurate than the unweighted method. However, the Fourier method did have one disadvantage. The 7090 requires 400 microseconds for the computation of a sine or cosine. Because of this, the IBM time required for this method was more than twice that required for the weighted unit weight method (see equation 63). We thus decided to apply the latter technique in the final deduction of the ACV's flight derivatives.

Further conclusions reached during the survey were as follows:

- 1) Initiating the integration at a minimal velocity point (B in Fig. 14) improved the results by approximately  $\frac{1}{4}$  to  $\frac{1}{2}$  percent.
- 2) Both the Fourier and unit weight techniques were relatively insensitive to presmoothing (an improvement of only about .5 to 1 percent was realized.).
- 3) By ending the integration at G instead of G + 1 seconds (Fig. 14) all results were improved up to 3%.
- 4) If the initial velocity was altered by 10% in the exact solution, an error of approximately 16% was obtained in b indicating that great care must be exerted in the evaluation of the initial condition derivative.
- 5) When we initiated integration at C, D, or E of Fig. 14 (for  $\sigma > 0$ ), the results deteriorated with the amount of deterioration highest at E.

All the above conclusions were kept in mind when the weighted technique was applied to our final ACV equations.

## 6. EXPECTED ACCURACIES IN FINAL RESULTS

### 6.1. Introduction

The survey conducted in the last section indicated that the weighted unit weight method was most suitable for our application. Any accuracies quoted (Fig. 15) however, applied strictly to the simple equation used in the test and could not be utilized for estimating the accuracy of the derived aerodynamic derivatives. The tests, then, were repeated with the selected technique applied to the equations of motion developed in section 4.

### 6.2. Application of the Technique to the Equations of Motion

The time differentials in equations (48) are nondimensional (i. e.  $\hat{D}$  in table 2). Since our flight records were recorded as a function of true time  $t$ , we converted the nondimensional equations of motion back into the dimensional time domain for consistency.

The plunge or Z equation becomes

$$\begin{aligned} (C_{zH} + C_{zH}^*) \underline{A}_n + C_{z\dot{h}} \underline{B}_n + C_{zHH} \underline{D}_n + C_{z\theta} \underline{E}_n \\ + C_{zq} \underline{F}_n + (C_{z\varphi} + C_{z\varphi}^*) \underline{G}_n = \underline{H}_n^z \end{aligned} \quad (64)$$

where

$$\begin{aligned} \underline{A}_n &= \left[ \frac{1}{\text{Deq}} \sum_{i+1}^n \bar{J}_m h \right] \cdot W_n \\ \underline{B}_n &= \frac{t^*}{\text{Deq}} \left[ \sum_{i+1}^n J_m h - h(t_i) [t_n - t_i] \right] \cdot W_n \\ \underline{D}_n &= \left[ \frac{1}{\text{Deq}^2} \sum_{i+1}^n \bar{J}_m h^2 \right] \cdot W_n \\ \underline{E}_n &= \left[ \sum_{i+1}^n \bar{J}_m^\theta \right] \cdot W_n \\ \underline{F}_n &= \left[ t^* \left[ \sum_{i+1}^n J_m^\theta - \theta(t_i)(t_n - t_i) \right] - \frac{\text{Deq}}{R} \frac{U}{V_J} \sum_{i+1}^n \bar{J}_m^\varphi \right] \cdot W_n \\ \underline{G}_n &= \left[ \sum_{i+1}^n \bar{J}_m^\varphi \right] \cdot W_n \\ \underline{H}_n^z &= \left[ -\frac{\mu t^*}{V_J} \left[ h(t_n) - h(t_i) - \dot{h}(t_i)(t_n - t_i) \right] + \frac{\text{Deq}}{R} \frac{g}{q_J} \mu \sum_{i+1}^n \bar{J}_m^\varphi \right] \cdot W_n \end{aligned}$$

# Contrails

where  $\sum_{i+1}^n J_m^\chi$  and  $\sum_{i+1}^n \bar{J}_m^\chi$  are defined by equations (55) and (57) ( $\chi = \theta(t), h(t), \varphi(t)$  or  $\psi(t)$  records),  $W_n = (N+1-n)\Delta t$  and is the weighting function required for the weighted unit weight technique.  $N$  and  $n$  are defined in Figure 14.

By applying equation (64) for  $t_i \dots t_n \dots t_N$  of the flight records,  $N-i$  equations are obtained which by least squares (Ref. 23) reduce to

$$\begin{bmatrix} C_{ZH} + C_{ZH}^* \\ C_{Z\dot{h}} \\ C_{ZH\dot{h}} \\ C_{Z\theta} \\ C_{Zq} \\ C_{Z\varphi} + C_{Z\dot{\varphi}}^* \end{bmatrix} = \begin{bmatrix} \sum_{i+1}^N \underline{A}_n^2, \sum_{i+1}^N \underline{B}_n \underline{A}_n, \sum_{i+1}^N \underline{D}_n \underline{A}_n, \dots \dots \sum_{i+1}^N \underline{G}_n \underline{A}_n \\ \vdots \quad \sum_{i+1}^N \underline{B}_n^2 \\ \vdots \quad \sum_{i+1}^N \underline{D}_n^2 \\ \vdots \\ \vdots \\ \sum_{i+1}^N \underline{A}_n \underline{G}_n \quad \dots \quad \sum_{i+1}^N \underline{G}_n^2 \end{bmatrix}^{-1} \begin{bmatrix} \sum_{i+1}^N \underline{A}_n \underline{H}_n^Z \\ \vdots \\ \vdots \\ \vdots \\ \vdots \\ \sum_{i+1}^N \underline{G}_n \underline{H}_n^Z \end{bmatrix} \quad (65)$$

Similarly, the pitching motion equation is

$$C_{m_H} \underline{A}_n + C_{m_{\dot{h}}} \underline{B}_n + C_{m_\theta} \underline{E}_n + C_{m_q} \underline{F}_n + C_{m_{\theta\dot{h}}} \underline{P}_n = \underline{H}_n^m \quad (66)$$

where

$$\underline{P}_n = \left[ \frac{1}{\text{Deq}} \sum_{i+1}^n \bar{J}_m^\theta \frac{\theta^k}{h} \right] \cdot W_n$$

and

$$\underline{H}_n^m = \left[ \left\{ \frac{\text{Deq}^2}{R^2} \frac{q}{q_J} (i_c - i_q) + \frac{\text{Deq}}{R} \frac{U}{V_J} i_{cf} \gamma_f \right\} \sum_{i+1}^n \bar{J}_m^\theta + i_b t^{*2} \left\{ \theta(t_n) - \theta(t_i) - \dot{\theta}(t_i)(t_n - t_i) \right\} + t^* \left\{ \frac{\text{Deq}}{R} \frac{U}{V_J} (i_c - i_q - i_b) + i_{cf} \gamma_f \right\} \left\{ \sum_{i+1}^n \bar{J}_m^\varphi - \varphi(t_i)(t_n - t_i) \right\} \right] \cdot W_n$$

Coefficients  $\underline{A}_n$ ,  $\underline{B}_n$ ,  $\underline{E}_n$  and  $\underline{F}_n$  are defined by equation (64). Equation (66) gives

$$\begin{bmatrix} C_{mH} \\ C_{m\dot{H}} \\ C_{m\theta} \\ C_{mq} \\ C_{m\theta H} \end{bmatrix} = \begin{bmatrix} \sum_{i+1}^N \frac{A_n^2}{|I_n^2} & \sum_{i+1}^N \frac{B_n A_n}{|I_n^2} & \sum_{i+1}^N \frac{E_n A_n}{|I_n^2} & \sum_{i+1}^N \frac{F_n A_n}{|I_n^2} & \sum_{i+1}^N \frac{P_n A_n}{|I_n^2} \\ \cdot & \sum_{i+1}^N \frac{B_n^2}{|I_n^2} & \cdot & \cdot & \cdot \\ \cdot & \cdot & \sum_{i+1}^N \frac{E_n^2}{|I_n^2} & \cdot & \cdot \\ \cdot & \cdot & \cdot & \sum_{i+1}^N \frac{F_n^2}{|I_n^2} & \cdot \\ \sum_{i+1}^N \frac{A_n P_n}{|I_n^2} & \cdot & \cdot & \cdot & \sum_{i+1}^N \frac{P_n^2}{|I_n^2} \end{bmatrix}^{-1} \begin{bmatrix} \sum_{i+1}^N \frac{A_n H_n^3}{|I_n^3} \\ \cdot \\ \cdot \\ \cdot \\ \sum_{i+1}^N \frac{P_n H_n^3}{|I_n^3} \end{bmatrix} \quad (67)$$

The same analysis on the roll and yaw equations of motion produces

$$\begin{aligned} C_{l_p} \underline{A}_n^l + C_{l_{\psi H}} \underline{B}_n^l + C_{l_{\psi}} \underline{C}_n^l + C_{l_r} \underline{D}_n^l + (C_{l_{\varphi}} + C_{l_{\varphi}}^*) \underline{E}_n^l \\ + C_{l_H}^* \underline{G}_n^l = \underline{H}_n^l \end{aligned} \quad (68)$$

and

$$C_{N_p} \underline{A}_n^l + (C_{N_{\psi}} + C_{N_{\psi}}^*) \underline{C}_n^l + C_{N_r} \underline{D}_n^l + C_{N_{\varphi}} \underline{E}_n^l = \underline{H}_n^y \quad (69)$$

# Contrails

where

$$\begin{aligned}
 \underline{A}_n^e &= \left[ \frac{Deq}{R} \frac{U}{V_J} \sum_{i+1}^m \bar{J}_m^\theta + t^* \left\{ \sum_{i+1}^n J_m^\varphi - \varphi(t_i)(t_n - t_i) \right\} \right] \cdot W_n \\
 \underline{B}_n^e &= \left[ \frac{1}{Deq} \sum_{i+1}^n \bar{J}_m^{\theta h} \right] \cdot W_n \\
 \underline{C}_n^e &= \left[ \sum_{i+1}^n \bar{J}_m^\psi \right] \cdot W_n \\
 \underline{D}_n^e &= t^* \left[ \sum_{i+1}^n J_m^\psi - \psi(t_i)(t_n - t_i) \right] \cdot W_n \\
 \underline{F}_n^e &= W_n \sum_{i+1}^n \bar{J}_m^\varphi \\
 \underline{G}_n^e &= \left[ \frac{1}{Deq} \sum_{i+1}^n \bar{J}_m^h \right] \cdot W_n \\
 \underline{H}_n^e &= W_n \cdot \left[ -t^* \left\{ \frac{Deq}{R} \frac{U}{V_J} (i_c - i_q - i_b) + i_{cf} \gamma_f \right\} \left\{ \sum_{i+1}^n J_m^\theta - \theta(t_i)(t_n - t_i) \right\} \right. \\
 &\quad + \left. \left\{ \frac{Deq^2}{R^2} \frac{q}{q_J} (i_c - i_b) + \frac{Deq}{R} \frac{U}{V_J} i_{cf} \gamma_f \right\} \sum_{i+1}^n \bar{J}_m^\varphi \right. \\
 &\quad \left. + i_q t^{*2} \left\{ \varphi(t_n) - \varphi(t_i) - \dot{\varphi}(t_i)(t_n - t_i) \right\} \right] \\
 \underline{H}_n^Y &= i_c t^{*2} \left[ \psi(t_n) - \psi(t_i) - \dot{\psi}(t_i)(t_n - t_i) \right] \cdot W_n
 \end{aligned}$$

whence the final roll equation is

$$\begin{bmatrix} C_{Lp} \\ C_{L\varphi H} \\ C_{L\psi} \\ C_{Lr} \\ C_{L\varphi} + C_{L\varphi}^* \\ C_{LH}^* \end{bmatrix} = \begin{bmatrix} \sum_{i+1}^N (A_n^e)^2 & \sum_{i+1}^N B_n^e A_n^e & \sum_{i+1}^N C_n^e A_n^e & \sum_{i+1}^N D_n^e A_n^e & \sum_{i+1}^N F_n^e A_n^e & \sum_{i+1}^N G_n^e A_n^e \\ \cdot & \sum_{i+1}^N (B_n^e)^2 & \cdot & \cdot & \cdot & \cdot \\ \cdot & \cdot & \sum_{i+1}^N (C_n^e)^2 & \cdot & \cdot & \cdot \\ \cdot & \cdot & \cdot & \cdot & \cdot & \cdot \\ \cdot & \cdot & \cdot & \cdot & \cdot & \cdot \\ \cdot & \cdot & \cdot & \cdot & \cdot & \cdot \\ \sum_{i+1}^N A_n^e G_n^e & \cdot & \cdot & \cdot & \sum_{i+1}^N (G_n^e)^2 & \sum_{i+1}^N G_n^e H_n^e \end{bmatrix} \begin{bmatrix} \sum_{i+1}^N A_n^e H_n^e \\ \cdot \\ \cdot \\ \cdot \\ \cdot \\ \cdot \\ \sum_{i+1}^N G_n^e H_n^e \end{bmatrix} \quad (70a)$$

and for yaw

$$\begin{bmatrix} C_{N\hat{p}} \\ C_{N\psi} + C_{N\psi}^* \\ C_{Nr} \\ C_{N\varphi} \end{bmatrix} = \begin{bmatrix} \sum_{i+1}^N (\underline{A}_n^e)^2 & \sum_{i+1}^N \underline{C}_n^e \underline{A}_n^e & \dots & \dots & \sum_{i+1}^N \underline{F}_n^e \underline{A}_n^e \\ \cdot & \sum_{i+1}^N (\underline{C}_n^e)^2 & & & \cdot \\ \cdot & & \cdot & & \cdot \\ \cdot & & & \cdot & \cdot \\ \sum_{i+1}^N \underline{A}_n^e \underline{F}_n^e & \dots & \dots & \dots & \sum_{i+1}^N (\underline{F}_n^e)^2 \end{bmatrix}^{-1} \begin{bmatrix} \sum_{i+1}^N \underline{A}_n^e \underline{H}_n^e \\ \cdot \\ \cdot \\ \cdot \\ \sum_{i+1}^N \underline{F}_n^e \underline{H}_n^e \end{bmatrix} \quad (70b)$$

These equations were programmed for the IBM 7090 Computer.

### 6.3. The Conditioning Check

Before performing the error survey on how scatter in the raw data affected the final results, (Section 6.5), a preliminary study was made on the basic equations themselves. For example, if the determinants of the square matrices, whose inverted forms are shown above, ever became zero the final deduced flight derivatives would be nonsensical. These errors are not a function of scatter in the raw data but of matrix conditioning.

As an illustrative example, let a simple dynamic system lead to the equations

$$\begin{aligned} \underline{A}_n C_{x_a} + \underline{B}_n C_{x_b} &= \underline{B}_n C_{x_c} \\ \underline{A}_n C_{y_a} + \underline{B}_n C_{y_b} &= L_n \end{aligned} \quad (71)$$

when the method is applied to its equations of motion.

The first of equations (71) can be rewritten as

$$\underline{A}_n C_{x_a} + \underline{B}_n \{C_{x_b} - C_{x_c}\} = 0$$

producing

$$[M] \begin{Bmatrix} C_{x_a} \\ C_{x_b} - C_{x_c} \end{Bmatrix} = 0 \quad (72)$$

while the second equation becomes

$$\begin{Bmatrix} C_{y_a} \\ C_{y_b} \end{Bmatrix} = [M]^{-1} \begin{Bmatrix} \sum_{i=1}^N \underline{A}_n \underline{L}_n \\ \sum_{i=1}^N \underline{B}_n \underline{L}_n \end{Bmatrix} \quad (73)$$

where

$$[M] = \begin{bmatrix} \sum_{i=1}^N \underline{A}_n^2 & \sum_{i=1}^N \underline{A}_n \underline{B}_n \\ \sum_{i=1}^N \underline{A}_n \underline{B}_n & \sum_{i=1}^N \underline{B}_n^2 \end{bmatrix}$$

on applying the method of least squares.

If  $C_{x_a}$  and  $C_{x_b} - C_{x_c}$  are not zero, the determinant of  $[M]$  must be. As a result,  $[M]^{-1} = \infty$  and no solution is possible. This linear dependence of coefficients was first discussed by H. Greenberg (Ref. 27). If the above occurs, additional information or assumptions are required to determine all the derivatives individually. Fortunately such a situation never occurred for our set; sizeable nonlinearities ( $C_{Z_{HH}} H^2$ ,  $C_{m_{\theta H}} \theta H$  and  $C_{L_{\varphi H}} \varphi H$ ) eliminated the possibility.

Note that coefficients  $\underline{A}_n$ , to  $\underline{E}_n$  of equation (64) and  $\underline{C}_N^{\ell}$  to  $\underline{G}_n^{\ell}$  of equations (68) and (69) each require only one of the 4 flight records ( $\theta$ ,  $\varphi$ ,  $\psi$  or  $h$ ) for their evaluation. If any of these variables are small in comparison to the others, a row or column in the Least Squares matrices, developed above, could become relatively small in comparison to the other elements; bad conditioning would result, producing poor accuracy in the deduced derivatives.

An available library program was used to evaluate equations (65), (67),



(70a) and (70b). This program provided an estimate of the reciprocal of the determinant of the square matrix involved, with estimates of expected computational accuracies. This source of error was never more than 5% for the cases calculated.

#### 6.4. The Effects of Data Scatter on the Final Results

The steps followed in this section parallel those described in section 5.3, namely;

- 1) Obtain representative values for the derivatives.
- 2) Substitute these into the equations of motion and determine the output histories (an analogue computer was used for this step).
- 3) Degrade this data by adding random errors, and determine the derivatives by applying the selected technique to the equations of motion.

A comparison between the results of step 1 and step 3 above, then indicates the amount of error induced in the final results because of scatter in the raw data.

From preliminary runs, a full set of aerodynamic derivatives were deduced using the computer program described above (call these the set A values). These derivatives (see step 1 above) were then substituted into the equations of motion and the equations were scaled and mechanized for the UTIAS Analogue Computer (a PACE 231R). The scaled equations of motion are given in Appendix C while the Analogue schematic is shown in Figure 16. The variable resistors on the Analogue Computer were adjusted for the Set A derivatives and some representative curves obtained (step 2). These records substituted for the experimental records that would otherwise be used in the digital computer program and a set of derivatives were deduced from them. (Set B and step 3). A comparison between Set A and Set B derivatives, then, produces a measure of our accuracy.

The same procedure as in section 5.3 was used to introduce artificial scatter to the analogue records with only one addition. The set of random numbers generated by the computer program was initiated by a number selected by the programmer. If we generated a second set using the same initial value, the numbers in the new series would be the same as the previous ones. For this investigation, three initiating numbers were selected producing 3 different sets of random numbers with a standard deviation of  $\sigma = 1/L$ . When each of these was added to the analogue records in turn, we obtained 3 different simulated experimental curves. Our error analysis then can be thought of as based on 3 separate simulated experiments, with the same initial vehicle conditions, instead of just one as in section 5.3.

We transferred the analogue records to the digital computation by firstly, reading the time histories from the graph paper, and then punching the results on data cards. Since there are errors associated with the electronics of the analogue and further errors in reading the variables from the graph paper the total error was certainly more than just that generated by the random number program. An estimate of the total scatter was obtained by the following method. The analogue data was taken and presmoothed as in Section 5 and the standard deviation between the presmoothed and degraded curve was computed.

## 6.5. Preliminary Error Analysis

Figures 17a and b illustrate the results. The ordinate is the % error between set A and set B derivatives while the abscissa is the Deviation Index (the X can be  $\theta$ , h,  $\phi$  or  $\psi$  depending upon which derivative is being examined --- i. e.  $X = \theta$  for the Cz curve). If our developed equations of motion represent the vehicle's dynamic system adequately, these curves can be used for determining the % error to be expected in each deduced derivative due to scatter in the raw data. This presupposes that there are no inputs from small irregularities in the ground (see section 2.1 - leveling) or from small engine rpm fluctuations (see section 4.7). A further discussion of these errors is continued in section 7.

## 7. FINAL RESULTS AND DISCUSSION

### 7.1. Testing Procedure

A test program was selected to illustrate the lightline cabling technique and to determine how all the ACV derivatives varied with height. As a result, 9 runs were performed at three different heights with 3 runs per height. The model's all up weight (see section 2.4) was selected by the following procedure. By prearranging at what engine r. p. m. a test would be conducted (see section 2.5), and selecting a test  $h/Deq.$  ratio Fig. 34 (available data) was used to determine A for  $q/q_J = 0$  and the vehicle's weight became  $W = L = JA$ . The velocity U was kept constant ( $U = 10.2 \pm 3\%$ ) by maintaining the model's c. g. position at  $.42 \pm .007$  inches ahead of mid chord.

On weighting the vehicle with lead, the body side attachment point was adjusted so that it lay in the vehicle's X'Y' plane (see Fig. 7) and the model's principal moments of inertia relative to the body fixed axes were then measured (see Section 4.2). Knowing vehicle velocity, weight and expected c. g. equilibrium height above ground for any run, the centerpost height was then adjusted so that the cable, near the vehicle, lay parallel to the model's X'Y' plane minimizing the cable derivatives (see Ref. 4). After starting the engine, its r. p. m. was "tuned" by adjusting the needle valve until the prearranged r. p. m. was obtained; the vehicle was then launched by hand. The flight itself consisted of the following:

- 1) One circuit of the track while only engine r. p. m. was recorded. This provided adequate time for the vehicle to accelerate to equilibrium and permitted an inflight check on the steadiness of the engine r. p. m.
- 2) The three subsequent circuits were then filmed (Section 2.2) and used in the data reduction.

If the vehicle behaved erratically in the above allotted time or if the engine r. p. m. fluctuated during part 1 of the above, the test was terminated and another initiated. This schedule was strictly maintained for two reasons. Firstly, the head of the engine usually worked loose, after the vehicle has completed 5 circuits around the track, creating a loss in engine compression and in vehicle height. Secondly, by keeping our flight time to a minimum, the fuel consumption was negligible; no correction had to be applied for change in vehicle weight or c. g. position.

While in flight, the vehicle was perturbed from equilibrium by a 1-1/4" down step on the ground. After an adequate length of level track to allow the transient to decay, a gently sloping ramp raised the vehicle again to its original height.

## 7.2. Reduced Data and Analogue Comparison

Figs. 18 to 29 present the time histories of  $\theta$ ,  $h$ ,  $\phi$  and  $\psi$  as determined by the analysis of Section 3. The reduction was initiated after the tailpoint of the vehicle had passed the step by  $\frac{1}{2}$  ft. From experiments conducted in reference 6, a "ground" pulse does not influence the vehicle's dynamic system if this perturbation occurs at least 6 inches from the rear target point (we can say that  $[\hat{F}] = 0$  in equation 47).

Each figure presents the results of 3 consecutive runs. The differences illustrated are not a result of changes in vehicle weight, H, r. p. m., or c. g. position since these remained constant during any three circuits around the track. They can be attributed to changes in the initial conditions (e. g.  $\theta(t_1)$  and  $\dot{\theta}(t_1)$ ). We had no control over these once the vehicle was released.

The flight histories were subsequently used in the equations of motion (Section 6.2) and all the aerodynamic derivatives were determined (table 3). These values were then substituted into the equations of Appendix C and an analogue comparison performed. Figures 30 to 33 are the results of this investigation. A discussion of these analogue comparisons will be presented in Section 7.5.

## 7.3. Equilibrium Data

Figs. 37 to 41, excluding 38b, present the derivatives as determined from the equations of motion; the results are corrected for cable effects. Figs. 34 to 36 were obtained by analyzing the equilibrium flight paths after all perturbations had decayed.

At equilibrium, lift equals weight. Thus plotting  $L/J$  for the various experimental H ratios produced the augmentation curve shown in Fig. 34. A comparison of the curve for  $q/q_j \neq 0$  and Gowans curve for  $q/q_j = 0$  (see Ref. 6) indicates that we obtained a loss in lift due to forward flight. This effect is also indicated by Figs. 35 and 36. This trend can be attributed to the following.

In hover, the pressure under the vehicle equals  $p_a + \Delta p$  (see Appendix B) while for forward flight this pressure becomes  $p_c + p_a + \Delta p$  where  $p_c$  is the static pressure on the external surface of the curtain induced by the forward velocity  $U$ . While suction pressures ( $p_c < 0$ ) are to be expected along the external sides of the vehicle, positive pressures ( $p_c > 0$ ) may occur on other parts of the annular jet. L. K. Mack and Ben-chie Yen (Ref. 2) indicated that the integrated effect of  $p_c$ , on the pressure under the vehicle, tended to create a loss of lift for forward flight.

In Fig. 35, we have a comparison of  $L/L_S$  vs.  $C_\mu$ . P. E. Colin suggested that the boundary layer on the wind tunnel ground board interacts strongly with the vehicle's cushion air creating an optimistic evaluation of lift with respect to forward speed ( $L/L_S = 1$  for  $C_\mu > 4$ ). R. Kuhn and A. W. Carter (Ref. 2), however, found negligible differences between towed-model and wind tunnel results. Furthermore, G. D. Boehler (Ref. 2 and Fig. 36) indicated that there is a loss of lift with forward speed when experimentation is conducted in a wind tunnel ( $L/L_S < 1$ ). This is in contradiction to the results of P. E. Colin.

This point was further investigated at UTIAS. After our experimental tests, the vehicle was mounted in the UTIAS wind tunnel (Ref. 32) and another lift evaluation made. The results (Fig. 34) indicate that there are negligible differences in the Augmentation curve ( $q/q_J = .034$ ) between the track and wind tunnel data. This substantiates the results of R. Kuhn and A. W. Carter. Fig. 35 shows that the differences between the track and the wind tunnel lift, as a function of  $C_\mu$ , are not as large as predicted by P. E. Colin.

The fair agreement between our results and P. E. Colin's pendulum results indicates a further point; namely, our vehicle was not too large in comparison to the dimensions of the track. With  $U = \Omega R$  (see Fig. 11) the relative wind over the tethering side of the vehicle becomes  $\Omega(R - b/2)$ , while that over the opposite side is  $\Omega(R + b/2)$ , where  $b$  is the span of the ACV. The velocity difference between the two sides can then be given as  $\Delta U/U = b/R$ .

When this factor is too large, the velocity gradient along the vehicle's Y axis could so disturb the pressure distribution over the vehicle as to make longitudinal flight simulation impossible. The fair agreement of our and P. E. Colin's  $L/L_S$  data indicates that the above effect was small even though our  $\Delta U/U$  ratio was larger than that of P. E. Colin (our  $\Delta U/U = .19$  as compared to his  $\Delta U/U = .05$ ).

#### 7.4. The Extracted Derivatives

Figure 37 shows a plot of  $C_{z_H}$  vs.  $H$ . A comparison was made with the results of the augmentation curve. By fitting a parabola to the data in Fig. 34 ( $q/q_J \neq 0$ ),

$$\frac{L}{J} = 6.16 - 124H + 809H^2$$

Differentiating this expression with respect to  $H$  gives

$$C_{z_H} = 124 - 1618H, \quad C_{z_{HH}} = -1618$$

A similar analysis on B. Gowans' results ( $q/q_J = 0$ ) produced

$$C_{z_H} = 87.5 - 1000H, \quad C_{z_{HH}} = -1000$$

Fig. 37 indicates that the agreement between extracted, theoretical (see Appendix B), and evaluated  $C_{z_H}$  is only fair (the black dots indicate extracted derivatives).

Due to scatter the extracted  $C_{z_{HH}}$  varied as  $-3000 \leq C_{z_{HH}} \leq 2000$  (see table 3). This qualitatively agrees with the values  $C_{z_{HH}} = -1618$  and  $C_{z_{HH}} = -1000$  above (see section 7.5). Comparing the  $q/q_J = .034$  and  $q/q_J = 0$  values obtained from the augmentation curves indicates that forward speed increases the curvature of the augmentation curve;  $C_{z_{HH}}$  was increased by 60%. This analysis clearly shows that the more reliable way of getting  $C_{z_{HH}}$  is from the augmentation curve (i. e. the value -1618), and that the value obtained from the general analysis procedure should be discarded.

Figure 37 also presents the variation of  $C_{z_{\dot{H}}}$  with  $H$ . Agreement between experimental and theoretical results is again only fair (see Appendix B).

Figure 38a is a plot of  $C_{z_{\varphi}}$ ,  $C_{z_{\theta}}$  and  $C_{z_q}$  vs.  $H$ . Theory predicts that both  $C_{z_{\varphi}}$  and  $C_{z_{\theta}}$  should be zero when the equilibrium angles are zero. In Fig. 38b (a figure reproduced from Ref. 13),  $C_L^*_{\alpha}$  is negative valued at  $\alpha = 0$  (for  $q/q_J = 0$  and  $q/q_J = .07$ ). Since  $Z = -L$ , this suggests that, even though Dau's configuration is very different,  $Z_{\theta}$  and  $Z_{\varphi}$  would be positive. This is consistent with the results shown in Fig. 38a (K. Dau's definition of  $C_L^* = L/(qs + J)$ ).

Figure 39 shows the variation of  $C_{m_{\theta}}$  and  $C_{m_q}$  with  $H$ . Because of the scatter, it is difficult to be certain whether forward speed had a substantial effect on these derivatives; B. Gowans' data was obtained at  $q/q_J = 0$  (Ref. 6) however, the data suggests that both derivatives become more negative with forward speed. H. Chaplin on the contrary (Ref. 30), indicates that forward velocity has little effect on  $C_{m_{\theta}}$  when  $0 \leq U \leq 20$  fps.

$C_{m_H}$  and  $C_{m_{\dot{H}}}$  are depicted in Figure 40. Due to the large scatter one cannot determine whether  $C_{m_H}$  is a function of  $H$ . Inclinations are, however, that  $C_{m_{\dot{H}}}$  increases with decrease in height.

$C_{l_{\varphi}}$ ,  $C_{l_p}$ ,  $C_{l_{\psi}}$ ,  $C_{l_H}^*$  and  $C_{l_r}$  are shown in Figures 40 and 41. As can be seen,  $C_{l_{\varphi}}$ ,  $C_{l_p}$ , and  $C_{l_H}^*$  are qualitatively consistent with the theoretical predictions; the cable derivative  $C_{l_H}^*$  is known exactly, (see Eq. 40) and is given in table 3 while the theory for  $C_{l_{\varphi}}$  and  $C_{l_p}$  is given in Appendix B. For airplanes,  $C_{l_r}$  is estimated by considering the lift on the

fin. Since our fin lay in the wake of the intake, no such estimate could be made. The figure indicates that  $C_{l_r}$  decreases with a reduction in H.

The yaw derivatives are also presented in Figure 41. The excessive scatter however precludes any conclusions as to whether these are functions of H.

The extracted nonlinear derivatives  $C_{m_{\theta H}}$  and  $C_{l_{\phi H}}$  are presented in Table 3. Due to scatter,  $C_{m_{\theta H}}$  varies as  $-38 < C_{m_{\theta H}} < 58$  while  $C_{l_{\phi H}}$  lies in the range  $-165 \leq C_{l_{\phi H}} \leq 437$ . By computing the mean theoretical slope of  $C_{m_{\theta}}$ , in Fig. 39, and  $C_{l_{\phi}}$ , in Fig. 40 ( $C_{m_{\theta H}} \sim 17$ ,  $C_{l_{\phi H}} \sim 15$ ), we see that the experimental results qualitatively agree with the theoretical predictions. As with  $C_{z_{HH}}$ , it appears that the more satisfactory method of determining  $C_{m_{\theta H}}$  and  $C_{l_{\phi H}}$  is from plots of  $C_{m_{\theta}}$  and  $C_{l_{\phi}}$  as H.

To our knowledge,  $C_{m_q}$ ,  $C_{m_H}$ ,  $C_{m_{\dot{H}}}$ ,  $C_{l_p}$ ,  $C_{l_{\psi}}$ ,  $C_{l_r}$  and all the yaw derivatives, presented above, have not been previously presented in the literature.

## 7.5. Error Analysis

Scatter in our time histories, Figs. 18 to 29 inclusive, was due to both film measurement errors (see Section 2.2), and inaccuracies in the level of the reference gridlines (see Fig. 1). The film measurement errors occurred because of the following. With the camera, lighting, and film used in recording our data, a clear image of the vehicle was obtained when the film was projected to  $\frac{1}{2}$  full scale; the image deteriorated if we projected to a larger size. All Distances (see Figure 6) were then measured to an accuracy of  $\pm 1/100$  inches. The reference gridlines, on the other hand, were level to an accuracy of  $\pm 1/64$  inches. The combination of these two errors resulted in an angular measurement error of approximately  $\pm .003$  radians and a height error of approximately  $\pm .03$  inches.

In section 6.5 (see Figs. 17a and b for the results) an analysis was performed to determine the effect of the above errors, or scatter, on the final deduced derivatives. This theoretical error evaluation was related to our experimental results as follows. The time histories (Figs. 18 to 29) were presmoothed by the moving arc technique (Section 5.3), and the experimental standard deviation between the raw and smoothed data was determined. The mean experimental Deviation Index was then computed and is shown in Figures 17a and 17b. For the amount of scatter associated with our flight records (indicated by the experimental Deviation Index) Figs. 17a and 17b were used to predict the expected percentage errors for the deduced aerodynamic derivatives (see Table 4). The mean percentage errors of the ACV's flight deri-

# Conclusions

vatives, (Table 3) were also determined and are shown in Table 4 for comparison (see Table 4 for the definition of these errors) Fig. 41a is a plot of predicted versus experimental errors. An examination of the longitudinal derivatives indicates that these are quantitatively consistent with the expected theoretical error except for  $C_{z_{HH}}$ ,  $C_{\eta_{HH}}$ ,  $C_{z_{\theta}}$  (see Fig. 41a). For the asymmetrical derivatives, the differences between predicted and actual errors is at least a factor of 2 except for  $C_{L_{\psi}}$ ,  $C_{L_{\psi}}$  and  $C_{N_{\psi}}$  (see Fig. 41a). Other factors, not accounted for in Section 6.5, then produced these discrepancies. One cause for the differences in Table 4 could be the following. In determining the experimental Deviation Index, we used the difference between a smoothed approximation to the output and the actual data (Figs. 18 to 29); we could not compare with the true (unknown) curves. This index, then could be an erroneous estimate of the true deviation; the experimental mean shown in Figs 17a and b could be different from that shown increasing the predicted theoretical error. Another source for this difference, between theoretical and actual derivative errors, lies in the use of Equation 45. We assumed that the vehicle's dynamic system was not subjected to inputs during analysis (for  $\dot{f}(t) = 0$  in Eq. 49). Small fluctuations in ground height (Section 2.1) and small changes in r. p. m. (Section 4.7) could provide such inputs affecting the final accuracies of the extracted derivatives, producing a progressive increase, with time, in the difference between the analogue and experimental curves.

Fig. 30 indicates that, for pitch ( $t \leq 20/32$ ) this effect was small. Some influence, however can be seen when  $t > 20/32$ . This factor is more evident in the plunging results shown in Fig. 31 and is especially so for  $H = .054$  and  $H = .043$ . With the vehicle subjected to the same ground fluctuations and inputs for each run, the large differences between analogue and experimental records, for  $H = .05$  and  $H = .043$  ( $t \leq 30/32$ ) may not be attributable entirely to "ground" effects in light of the good agreement for  $H = .070$  ( $t \leq 30/32$ ) This indicates, however, that r. p. m. fluctuations and jet momentum flux inputs, though evidently small for the  $H = .070$  run shown in Fig. 31, may have been sizeable for the  $H = .054$  and  $H = .043$  runs shown. The engine frequency must be controlled more accurately than that for this investigation (i. e. our r. p. m. was accurate to  $\pm 1$  cps.). Finally, the  $\sigma$ 's used in developing this error analysis were based on the results of only 3 runs for each height. With more runs for analysis, we would expect better consistency between predicted and experimental errors. Namely, the derivative points shown in Fig. 41a would lie closer to the predicted = experimental line.

The method of vehicle harnessing affected derivative accuracy. The side body cable attachment point minimized the longitudinal cable derivatives while creating large cable restoring moments in the yaw and roll equations (see  $C_{N_{\psi}}$  and  $C_{L_{\psi}}$  in Table 3). This effect can be generalized as follows (see  $H = .043$  of Fig. 32). The aerodynamic terms in the roll equation are determined from the curve  $f_1(t)$ . The scatter, then, may be small with



# Conclusions

respect to  $\dot{\psi}(t)$  yet large with respect to  $f_1(t)$  increasing the error in the final results. In Figure 32, the inertia, cable and gyro terms constitute 40% of the roll output; the analogue comparison was made for  $C_{\dot{x}\dot{\psi}}^* = -.62$  and  $C_{\dot{y}\dot{\psi}}^* = -.37$  (Table 3). When  $C_{\dot{x}\dot{\psi}}^* = -.03$  and  $C_{\dot{y}\dot{\psi}}^* = -.62$  ( $H = .043$  in Table 3) the aerodynamic derivatives could be swamped by the cable restraint producing up to, or more than, 100% errors in the extracted asymmetrical (Table 4) results. Figure 33 ( $H = .054$ ) illustrates this fact. In this case  $C_{N_x}^* = -.52$  and  $C_{N_y}^* = 0$ . The inertia and cable terms have completely dominated the output so that little accuracy can be expected. This could account for the rather large errors associated with the yaw equation (i. e.  $C_{N_y}$  error predicted  $\sim 70\%$ ). We would expect maximum accuracy for these derivatives since this equation has the smallest number of derivatives to be determined (i. e. 4). This would also account for the large differences in error between the  $C_{\dot{\psi}}$  and  $C_{z_{\dot{h}}}$  derivatives. Both plunge and roll equations had 6 unknown derivatives (see Table 4 and Fig. 41a).

## 7.6 Track Improvements

Assuming that cable influences are small, the accuracies of the final deduced derivatives could be 95% if the Deviation Index were reduced by a factor of at least 10 and if the equations of motion represented the vehicle's dynamic system adequately (Fig. 17a and b). This means that the time records must be obtained (see section 3) with a higher degree of precision than in this investigation. This can be done by either improving the photography technique, or by recording the data by means of accelerometers.

Assuming, for argument's sake, that  $\frac{b_3 - b_5}{k_1 + k_3}, \psi, \dot{\psi}$ , and  $d$  are negligible, equation 12 becomes

$$\theta \doteq \frac{2(\bar{z}_1 - \bar{z}_3)}{k_1 + k_3} + \text{original error}$$

where  $\bar{z}_1$  and  $\bar{z}_3$  are measured from a 1/2 full size projected picture (see Section 7.5). If a lower ASA rated film (finer grain) and a 35 mm camera (double the size of the one used) recorded the data, one could project the vehicle image to double full size reducing the original error by 4, assuming the same  $\pm 1/100$  of an inch error in measurement. Meanwhile, by selecting a new vehicle ( $b_1 + b_3 = 10$  ft.), a further reduction of approximately 3 (our  $b_1 + b_3 \sim 3$  ft.) can be achieved (for  $\theta \sim 2^\circ$ ) reducing the total pitch error by a factor of 12.

Thus, with the pitch angle equation as an indicator, the required precision in the flight histories can be obtained. A new track, however, would be required (see  $\Delta y/d$  in section 7.3), about 60' in diameter. This would present new problems of model development, especially in relation to motors.

By placing an accelerometer at the c. g., and at points corresponding to  $P_1$  and  $P_2$  of our vehicle (Fig. 7), all variable accelerations could be determined; from our flight records the total accelerations would be less than  $32.2 \text{ ft./sec.}^2$  if a vehicle the size of ours were used. In our analyses, the

# *Contrails*

selected derivative extraction technique required the use of the double integral and the evaluation of the initial velocities for all flight records (only displacements were obtained). With acceleration histories, both of these error producing computations could be avoided resulting in better derivative accuracy than that predicted by our error analysis. Thus another evaluation of the various techniques presented (see Sections 5 and 6) and another error analysis would have to be made to evaluate fully the gains to be expected from including accelerometers in the instrumentation.

## 8. CONCLUSIONS

The feasibility study initiated in Ref. 3 has now been completed. A relatively inexpensive technique has been developed whereby an ACV's aerodynamic derivatives can be determined. We found that the large inaccuracies obtained in our final derivatives were caused by inadequacies in our data recording and reduction system; these errors are not intrinsic in light line tethering technique itself. We found, further, that the method of tethering can influence the final results. In our case, the vehicle was harnessed such that the longitudinal cable effects were minimal while strong yaw and roll cable effects existed. This literally "swamped" the aerodynamic asymmetrical derivatives, for some runs, producing large errors in the deduced asymmetrical derivatives; this effect, however, can be avoided if the cable is attached at the c. g.

With additional development, either photography or accelerometers can be used to record the data accurately enough so that all derivatives would be extracted to an accuracy of 95%. This presupposes that there are no inputs either from irregularities in the ground, or fluctuations in the vehicle's jet momentum flux.

## APPENDIX I

### The General Equations of Motion

The dynamic and kinematic equations produced in Ref. 6 are collected below for convenience.

The force equations in the X, Y, and Z axes directions are

$$\begin{aligned}
 X - mg \sin \theta &= m(\dot{U} + QW - RV) \\
 Y + mg \cos \theta \sin \phi &= m(\dot{V} + RU - PW) \\
 Z + mg \cos \theta \cos \phi &= m(\dot{W} + PV - QU)
 \end{aligned}
 \tag{A-1}$$

The moment equations for the X, Y, and Z axes are

$$\begin{aligned}
 L &= A\dot{P} - E\dot{R} + QR(C-B) - EPQ + Qh'_z - Rh'_y \\
 M &= B\dot{Q} + RP(A-C) + E(P^2 - R^2) + Ph'_x - Ph'_z \\
 N &= -E\dot{P} + C\dot{R} + QP(B-A) + EQR + Ph'_y - Q'h_x
 \end{aligned}
 \tag{A-2}$$

where  $h'_x$ ,  $h'_y$  and  $h'_z$  terms are spinning rotor contributions.

The angular velocities about these axes become

$$\begin{aligned}
 P &= \dot{\phi} - \dot{\psi} \sin \theta \\
 Q &= \dot{\theta} \cos \phi + \dot{\psi} \cos \theta \sin \phi \\
 R &= \dot{\psi} \cos \theta \cos \phi - \dot{\theta} \sin \phi
 \end{aligned}
 \tag{A-3}$$

where

$$\begin{aligned}
 \dot{\theta} &= Q \cos \phi - R \sin \phi \\
 \dot{\phi} &= P + Q \sin \phi \tan \theta + R \cos \phi \tan \theta \\
 \dot{\psi} &= (Q \sin \phi + R \cos \phi) \sec \theta
 \end{aligned}
 \tag{A-4}$$

# Contrails

Referring to Prof. B. Etkin's definition of fixed and vehicle axes systems (Ref. 6)

$$\frac{dx'}{dt} = U \cos \theta \cos \psi + V (\sin \phi \sin \theta \cos \psi - \cos \phi \sin \psi) \\ + W (\cos \phi \sin \theta \cos \psi + \sin \phi \sin \psi)$$

$$\frac{dy'}{dt} = U \cos \theta \sin \psi + V (\sin \phi \sin \theta \sin \psi + \cos \phi \cos \psi) \\ + W (\cos \phi \sin \theta \sin \psi - \sin \phi \cos \psi) \quad \text{A-5}$$

$$\frac{dz'}{dt} = U \sin \theta + V \sin \phi \cos \theta + W \cos \phi \cos \theta$$

APPENDIX II

A Theoretical Evaluation of Some Aerodynamic Derivatives

B.1 The  $C_{z_H}$  and  $C_{z_H}$  Derivatives

The momentum equation when applied to the curtain air flow gives

$$\Delta p h = \rho V_j^2 G (1 - \sin \gamma) \frac{\eta_A}{\eta_J} \quad \text{B-1}$$

when we assume an incompressible, inviscid flow with the curtain air behaving as in Figure 42a. The  $\eta_A$  and  $\eta_J$  are included as a correction factor; they take into account various influences which are not considered in inviscid flows, i.e. viscosity.  $\eta_A/\eta_J$ , then, should not be considered as some form of an efficiency but as an empirical quantity which corrects the ideal pressure rise to that obtained in the actual vehicle.

Now, with augmentation given as

$$A = \frac{L}{J} = \cos \gamma + \frac{\Delta p S}{J} \quad \text{B-2}$$

where S is the base area of the vehicle, the lift force can be written as

$$L = J \cos \gamma + \frac{\rho V_j^2 G S}{h} (1 - \sin \gamma) \frac{\eta_A}{\eta_J} \quad \text{B-3}$$

when B-1 is substituted into B-2.

The non-dimensional Z reaction then becomes

$$C_z = -\cos \gamma - \frac{S}{C} \frac{1}{D_{eq} H} (1 - \sin \gamma) \frac{\eta_A}{\eta_J} \quad \text{B-4}$$

where C is the total length of annular jet, and

$$C_{z_H} = \frac{S}{C} \frac{1}{D_{eq} H^2} (1 - \sin \gamma) \frac{\eta_A}{\eta_J} \quad \text{B-5}$$

In Ref. 2 (paper 8) M. P. Tulin presents the basic concepts for evaluating the heave damping derivatives for an ACV.

Suppose the vehicle approaches the ground (Fig. 42f). A pressure build-up under the vehicle may then be too high for the given annular jet and some pressurized air will escape out to atmosphere between the ground and the curtain.

Assuming no mixing between escaping and annular jet air, the pressure rise across the curtain becomes

$$\Delta p = \frac{G \rho V_j^2 (1 - \sin \gamma)}{h'} \left( \frac{\eta_A}{\eta_J} \right) \quad \text{with } h' = h_e + \dot{h} t - G u, \quad \dot{h} < 0 \quad \text{B-6}$$

where  $h_e$  is the equilibrium height above ground.

With incompressibility, the volume flow of the air passing under the curtain is

$$G_u V_u C \sim - \dot{h} s \quad \text{for } \dot{h} < 0 \quad \text{and} \quad \text{B-7}$$

for a three-dimensional vehicle.

After applying Bernoulli's equation to the escaping curtain air

$$\Delta p = \frac{1}{2} \rho V u^2 \quad \text{B-8}$$

where  $\Delta p$  is given by equation B-6. Substituting equation B-8 and B-7 into B-6 gives

$$h' = h_e + \dot{h} t + \frac{\dot{h} s}{c \sqrt{\frac{2}{\rho} \Delta p}}$$

and

$$\Delta p = \frac{\rho V_j^2 G (1 - \sin \gamma)}{\left[ h_e + \dot{h} t + \frac{\dot{h} s}{c \sqrt{\frac{2}{\rho} \Delta p}} \right]} \left( \frac{\eta_A}{\eta_J} \right) \quad \text{B-9}$$

From equation (B-2), we know that

$$\left[ \frac{\partial}{\partial \dot{h}} (L) \right] = S \left[ \frac{\partial}{\partial \dot{h}} (\Delta p) \right] \quad \text{B-10}$$

Thus

$$\frac{\partial}{\partial \dot{h}} \left[ \frac{L}{J} \right] = - \frac{S^2}{C^2 h_e^2} \frac{(1 - \sin \gamma)}{\sqrt{\frac{2}{\rho} \Delta p}} \left( \frac{\eta_A}{\eta_J} \right) \quad \text{B-11}$$

when equation (B-9) is substituted into equation (B-10). Since  $C_z = - \Delta L/J$ , the heave damping derivative for a falling vehicle is

$$\frac{\partial}{\partial \dot{h}} (C_z) = \left( \frac{\eta_A}{\eta_J} \right) \frac{(1 - \sin \gamma)}{\sqrt{\frac{2}{\rho} \Delta p}} \frac{S^2}{C^2 h^2} \quad \text{B-12}$$

If the vehicle rises, the pressure under the vehicle decreases and if this pressure is less than that necessary for the balanced operation of a given edge jet, air will be sucked into the space under the vehicle. The physical situation is illustrated by Fig. 42. The pressure rise through the curtain is given by

$$\Delta p = \left[ \frac{G_A}{h} \rho V_j^2 - \frac{G \rho V_j^2 \sin \gamma}{h} - \frac{G_u \rho V_u^2}{h} \right] \frac{\eta_A}{\eta_J} \quad \text{B-13}$$

where  $G_A$  and  $G_u$  are defined in the figure and

$$h = h_e + \dot{h} t \quad \text{B-14}$$

By continuity  $\dot{h} s \sim V_u G_u C \quad \text{B-15}$

thus  $G_u = \frac{\dot{h} s}{V_u C}$  and  $\frac{G_u \rho V_u^2}{h} = \frac{\dot{h} s}{C h} \rho V_u \quad \text{B-16}$



The total pressure at the annular jet exit is given by

$$p_o - p_a = \frac{\Delta p}{2} + \frac{1}{2} \rho V_j^2 \quad \text{B-17}$$

when a linear variation of pressure is assumed through the curtain. Furthermore, for inviscid flow, the total pressure at point B is

$$p_o - p_a = \Delta p + \frac{1}{2} \rho V_u^2 \quad \text{B-18}$$

On combining equations (B-17) and (B-18)

$$V_u = \sqrt{V_j^2 - \frac{\Delta p}{\rho}} \quad \text{B-19}$$

and from equation (B-16)

$$\frac{G_u \rho V_u^2}{h} = \frac{\dot{h} s \rho}{C h} \sqrt{V_j^2 - \frac{\Delta p}{\rho}} \quad \text{B-20}$$

By continuity, the flow of curtain air becomes

$$G C V_j = G_A C V_j + G_u C V_u \quad \text{B-21}$$

substituting (B-16) into (B-21) for  $G_u$  reduces to

$$G_A = G - \frac{\dot{h} s}{C V_j} \quad \text{B-22}$$

On substituting equation (B-22) and (B-20) into (B-13), we obtain

$$\Delta p = \left[ \frac{\left(G - \frac{\dot{h}_s}{CV_j}\right)}{(h_e + \dot{h}t)} \rho V_j^2 - \frac{G \rho V_j^2}{(h_e + \dot{h}t)} \rho V_j^2 \sin \gamma - \frac{\dot{h}_s \rho}{C(h_e + \dot{h}t)} \sqrt{V_j^2 - \frac{\Delta p}{\rho}} \right] \left( \frac{\eta_A}{\eta_J} \right) \quad \text{B-23}$$

where  $\Delta p$  is the pressure under the vehicle operating in the overfed condition (Fig. 42C).

From equation (B-10)

$$\frac{\partial}{\partial \dot{h}} (L) = \frac{\eta_A}{\eta_J} \left[ -\frac{S^2 \rho V_j}{C h_e} - \frac{S^2 \rho}{C h_e} \sqrt{V_j^2 - \frac{\Delta p}{\rho}} \right] \quad \text{B-24}$$

Again, with  $C_z = -\Delta L/J$ , the heave damping derivative for a rising vehicle becomes

$$\frac{\partial}{\partial \dot{h}} (C_z) = \frac{1}{J} \left( \frac{\eta_A}{\eta_J} \right) \frac{\rho S^2}{C h_e} \left[ V_j + \sqrt{V_j^2 - \frac{\Delta p}{\rho}} \right] \quad \text{B-25}$$

In the development of the equations of motion,  $C$  was assumed constant. Thus the damping derivative deduced from the flight records was the mean between equation (B-25) and (B-12), namely

$$C_{z\dot{h}} = \frac{1}{2} \left[ \frac{1}{Deqt^*} \left( \frac{\eta_A}{\eta_J} \right) \frac{(1 - \sin \gamma) S^2}{\frac{2}{\rho} \Delta p C^2 H^2} + \frac{1}{t^*} \left( \frac{\eta_A}{\eta_J} \right) \frac{\rho S^2}{JCH} \left\{ V_J + \sqrt{V_J^2 - \frac{\Delta p}{\rho}} \right\} \right] \quad \text{B-26}$$

where  $C_{z\dot{h}}$  is in the final non-dimensional form. This expression is shown in Figure 37.

The plunge damping derivative for a rising vehicle is .3 that of a falling vehicle by the above theory. Further investigations should be conducted to

determine whether such a large difference actually does occur physically, and, if so, an allowance for this must be made in the equations of motion - the above predictions are based on a very simple mathematical model.

## B.2. The $C_{m\theta}$ , $C_{\ell\varphi}$ , $C_{z\theta}$ and $C_{z\varphi}$ Derivatives

In Figure 42d, we have a view of a compartmented vehicle perturbed in pitch. If we assume that the stability jets prevent air exchange between compartments, compartment 3 will have a higher pressure than compartment 1 because its mean height above ground has been reduced.

We can, then, say

$$\Delta p_1 = \frac{\rho V_J^2 G}{h_e + l_\theta} \left[ 1 + \sin(|\gamma|) - \theta \cos(|\gamma|) \right] \frac{\eta_A}{\eta_J} \quad \text{B-27}$$

and

$$\Delta p_3 = \frac{\rho V_J^2 G}{h_e - l_\theta} \left[ 1 + \sin(|\gamma|) + \theta \cos(|\gamma|) \right] \frac{\eta_A}{\eta_J} \quad \text{B-28}$$

where the numbers 1 and 3 refer to compartments 1 and 3.

The pressure difference between these two compartments gives, on linearization

$$\delta(\Delta p) = \frac{2l_\theta}{h_e^2} \rho V_J^2 G \left\{ 1 + \sin(|\gamma|) \right\} \frac{\eta_A}{\eta_J} \quad \text{B-29}$$

while the restoring moment is

$$M = - \delta(\Delta p) l A_c \quad \text{B-30}$$

Substituting equation (B-29) into (B-30), non-dimensionalizing, and differentiating with respect to  $\theta$  produces a theoretical estimate of  $C_{m\theta}$ , namely

$$C_{m\theta} = - \frac{2l^2 A_c}{H^2 C D_{eq}^3} \left\{ 1 + \sin(|\gamma|) \right\} \frac{\eta_A}{\eta_J} \quad \text{B-31}$$

One can easily prove that

$$\Delta L = \Delta p_1 A_c + \Delta p_3 A_c \neq f(\theta) \quad \text{B-32}$$

whence  $C_{z\theta} = 0 \quad \text{B-33}$

If the vehicle were perturbed in roll, we would find that equation (B-31) and (B-33) provide an estimate of  $C_{\ell q}$  and  $C_{zq}$  when  $\ell$  and  $A_c$  refer to the side compartments.

These expressions are shown in Figures 39 and 40.

### B. 3. The $C_{mq}$ and $C_{\ell p}$ Derivatives

In Figure 42e, we illustrate the vehicle perturbed by a  $q$ . With no air interchange between compartments, the fore compartment 1 operates in an overfled condition (Fig. 42c) while the rear one operates in an underfled condition (Fig. 42b).

$$F_1 \doteq A_c \left| \left( \frac{\partial(\Delta p)}{\partial \dot{h}} \right)_o \right| \dot{h} \quad \text{and} \quad F_2 \doteq A_c \left| \left( \frac{\partial(\Delta p)}{\partial \dot{h}} \right)_u \right| \dot{h} \quad \text{B-34}$$

where the subscripts  $o$  and  $u$  indicate overfled and underfled and where  $\left( \frac{\partial \Delta p}{\partial \dot{h}} \right)_o$  and  $\left( \frac{\partial \Delta p}{\partial \dot{h}} \right)_u$  are determined by equations (B-9) and (B-23).

Since  $\dot{h} = q\ell$

$$M \doteq -A_c \ell^2 \left[ \left| \left( \frac{\partial \Delta p}{\partial \ell q} \right)_o \right| + \left| \left( \frac{\partial \Delta p}{\partial \ell q} \right)_u \right| \right] q$$

and

$$C_{mq} = -\frac{A_c \ell^2}{t^* J_{Deq}} \left[ \left| \left( \frac{\partial \Delta p}{\partial \dot{h}} \right)_o \right| + \left| \left( \frac{\partial \Delta p}{\partial \dot{h}} \right)_u \right| \right] \quad \text{B-35}$$

as before, this equation can be used to estimate  $C_{Lp}$  (see Figures 39 and 40).

#### B. 4. An Estimate of $\eta_A/\eta_J$

The experimental augmentation curve (Fig. 34) was obtained with a fair degree of accuracy and the  $C_{Z_H}$  derivative (Fig. 37) was deduced in two ways (see section 7.4). These two were, then, selected in establishing an empirical value for  $\eta_A/\eta_J$  in equation (B-1). In Figure 34, the augmentation curves for  $\eta_A/\eta_J = .1$  and  $\eta_A/\eta_J = .2$ , indicate that the empirical value for  $\eta_A/\eta_J$  should be approximately .15 when equation (B-2) is compared with the experimental data. In Figure 37, equation (B-5) provides fair agreement between experiment and theory when  $\eta_A/\eta_J = .2$ . A ratio of .2 was selected as being representative of our vehicle and this correction factor was applied to all of the theoretically evaluated derivatives.

# Contrails

## APPENDIX III

### The Scaled Analogue Equations of Motion

$$\{\ddot{h}\} = -H_1\{100h\} - H_2\{10\dot{h}\} + H_3\{10000h^2\} - H_4\{20\theta\} - H_5\{5\dot{\theta}\} - H_6\{20\varphi\} \quad C-1$$

$$\{\ddot{\theta}\} = -TH_1\{100h\} + TH_2\{10\dot{h}\} - TH_3\{20\theta\} - TH_4\{5\dot{\theta}\} - TH_5\{20\varphi\} - TH_6\{5\dot{\varphi}\} + TH_7\{20000\theta h\} \quad C-2$$

$$\{\ddot{\varphi}\} = -PH_1\{20\varphi\} - PH_2\{5\dot{\varphi}\} + PH_3\{20\psi\} + PH_4\{5\dot{\psi}\} - PH_5\{100h\} - PH_6\{20\theta\} + PH_7\{5\dot{\theta}\} + PH_8\{2000h\varphi\} \quad C-3$$

$$\{\ddot{\psi}\} = -PS_1\{20\psi\} - PS_2\{5\dot{\psi}\} - PS_3\{20\varphi\} - PS_4\{5\dot{\varphi}\} - PS_5\{20\theta\}$$

$$\text{where } H_1 = \frac{(C_{zH} + C_{zH}^*)\beta^2}{100\mu t^{*2}} ; H_2 = \frac{(C_{z\dot{H}} + C_{z\dot{H}}^*)\beta}{10\mu t^*} ; H_3 = \frac{-C_{zHH}\beta^2}{\mu \text{Deg } t^{*2}(10000)} \quad C-4$$

$$H_4 = \frac{C_{z\theta}\pi\beta^2 \text{Deg}}{20(180)\mu t^{*2}} ; H_5 = -\frac{C_{z\dot{\varphi}}\pi\beta \text{Deg}}{5(180)\mu t^*}$$

$$H_6 = \frac{\left\{C_{z\varphi} + C_{z\dot{\varphi}}^* - \frac{\text{Deg } q}{R} \frac{q}{q_j} \mu - \frac{\text{Deg } U}{R} \frac{U}{V_j} C_{zq}\right\} \text{Deg } \beta^2 \pi}{20(180)\mu t^{*2}}$$

$$TH_1 = -\frac{C_{mH}\beta^2(1.80)}{\pi \text{Deg } t^{*2} i_b} ; TH_2 = \frac{18.0 \beta C_{m\dot{H}}}{\pi \text{Deg } i_b t^*}$$

$$TH_3 = \left[ -C_{m\theta} + \frac{\text{Deg}^2 q}{R^2} \frac{q}{q_j} (i_c - i_a) + \frac{\text{Deg } U}{R} \frac{U}{V_j} i_{cf} \gamma_f \right] \beta^2 / 20 i_b t^{*2} ; TH_4 = C_{mq} \beta / i_b t^*(5)$$

$$TH_5 = -\frac{\text{Deg } U}{R} \frac{U}{V_j} C_{mq} \beta^2 / 20 i_b t^{*2} ; TH_6 = \left[ \frac{\text{Deg } U}{R} \frac{U}{V_j} (i_c - i_a - i_b) + i_{cf} \gamma_f \right] \beta / i_b t^*(5)$$

# Contrails

$$TH_7 = C_{m\theta H} \beta^2 / \text{Deq } t^{*2} \quad (2000)$$

$$PH_1 = \beta^2 \left[ -(C_{l\varphi} + C_{l\varphi}^*) + \frac{\text{Deq}^2 q}{R^2 q_J} (i_c - i_b) + \frac{\text{Deq } U}{R V_J} i_{cf} \gamma_f \right] / i_a t^{*2} \quad (20)$$

$$PH_2 = -\beta C_{l_p} / t^* i_a \quad (5) ; PH_3 = C_{l_\psi} \beta^2 / 20 i_a t^{*2} ; PH_4 = C_{l_r} \beta / i_a t^* \quad (5)$$

$$PH_5 = -1.80 \beta^2 C_{l_H}^* / \pi \text{Deq } i_a t^{*2} ; PH_6 = -\frac{\beta^2 \text{Deq } U C_{l_p}}{R V_J t^{*2} i_a} \quad (20)$$

$$PH_7 = \left[ \frac{\text{Deq } U}{R V_J} (i_c - i_b - i_a) + i_{cf} \gamma_f \right] \beta / t^* i_a \quad (5) ; PH_8 = C_{l_{\varphi H}} \beta^2 / \text{Deq } t^* i_a \quad (2000)$$

$$PS_1 = -\beta^2 (C_{N\psi} + C_{N\psi}^*) / i_c t^{*2} \quad (20) ; PS_2 = -C_{N_r} \beta / t^* i_c \quad (5)$$

$$PS_3 = -\beta^2 C_{N\varphi} / i_c t^{*2} \quad (20) ; PS_4 = -\beta C_{N_p} / i_c t^* \quad (5)$$

$$PS_5 = \text{Deq } U C_{N_p} \beta^2 / R \cdot V_J \cdot t^{*2} \cdot i_c \quad (20)$$

$\beta$  is the machine time constant (i. e.  $t = \beta T$ )

{ } indicates volts and should not be confused with the sign for a column matrix. This definition only applies to this section.

## REFERENCES

1. The Transportation Research Associates  
N. Y. Air Cushion Vehicles  
Transportation of the Future  
New York, N. Y., 1962
2. A Compilation of Papers Symposium on Ground Effect  
Phenomena: Princeton University, Department of Aeronautical  
Engineering, Oct. 1959
3. Curtiss, E. S. The Ground Effect Machine  
Pfister, V. R. Experimental Facilities of  
Hydronautics, Inc., AIAA  
Aerodynamic Testing Conference,  
March 1964
4. Liiva, J. A Facility for Dynamic Testing  
of Models of Airborne Vehicles  
with Ground Effects: UTIA TN  
53, Oct. 1961
5. Radford, R. C. Development of a Propulsion  
System for Powering a Self-  
Propelled GETOL Model Aircraft:  
UTIA TN 64, Dec. 1962
6. Gowans, B. W. Experimental Study of the Aero-  
dynamic Characteristics of a  
Model of an Air Cushion Vehicle  
in Hovering Flight: UTIAS TN  
74, Feb. 1964
7. Etkin, B. Dynamics of Flight, Stability  
and Control: J. Wiley & Sons,  
Inc.
8. Colin, P. E. Powered Lift Model Testing for  
Ground Proximity Effects: TC5A  
TN 14, Oct. 1963
9. Morse, P. M. Vibration and Sound:  
McGraw-Hill



10. Etkin, B. Theory of the Flight of Airplanes in Isotropic Turbulence: Review and Extension  
UTIA Rep. No. 72, Feb. 1961
11. Diederich, F. W. The Response of an Airplane to Random Atmospheric Disturbances:  
NACA TN 1345, 1958
12. Etkin, B. A Theory of the Response of Airplanes to Random Atmospheric Turbulence:  
Journ. Aerospace Sciences 26, 7, July '59
13. Dau, K. Characteristics of a Rectangular Wing with a Peripheral Jet in Ground Effect, Part I:  
UTIAS TN 56, Sept. 1961
14. Shinbrot, M. On the Analysis of Linear and Nonlinear Dynamic Systems from Transient-Response Data:  
NACA TN 3288, Dec. 1954
15. Mantle, P. J.  
Phillips, L. W. The Extraction of Stability Data by Means of Telemetry from Configurations Tested in Ballistics:  
Carde Tech. Memo AB-70, March 1961
16. Donegan, J. J.  
Huss, C. H. Comparison of Several Methods for Obtaining the Time Response of Linear Systems to Either a Unit Impulse or Arbitrary Input from Frequency-Response Data:  
NACA TN 3701, July 1956
17. Eggeleston, J. M.  
Mathews, C. W. Application of Several Methods for Determining Transfer Functions and Frequency Response of Aircraft from Flight Data:  
NACA Rep. 1204, 1954

# Contrails

18. Brown, G. S.  
Campbell, D. P. Principles of Servo-Mechanisms:  
J. Wiley & Sons Inc. N. Y.
19. Doetsch, K. H. The Time Vector Method for  
Stability Investigations:  
RAE Rept. No. Aero 2495,  
August 1953
20. Seamens, Jr., R. C.  
Blasingame, B. P.  
Clementson, G. C. The Pulse Method for the Deter-  
mination of Aircraft Dynamic  
Performance:  
Journal of Aeor. Sciences,  
January 1960
21. Stepanoff, A. J. Turboblenders  
J. Wiley & Sons Inc., N. Y.
22. Donegan, J. J.  
Huss, C. H. Method and Tables for Determining  
the Time Response to a Unit Im-  
pulse from Frequency-Response  
Data and for Determining the Fourier  
Transform of a Function of Time:  
NACA TN 3598, Oct. 1957
23. Whittaker, E.  
Robinson, G. The Calculus of Observation  
Blackie & Son Limited
24. Bendat, J. S. Principles and Application of  
Random Noise Theory:  
J. Wiley & Sons, Inc.
25. Grahame, D.  
McRuer, D. Analysis of Nonlinear Control  
Systems:  
J. Wiley & Sons, Inc.
26. Logsdon, T. S. Moving-Arc Data Smoothing for  
Flight-Analysis Programs:  
AIAA Paper (No. 64-324)  
July, 1964
27. Greenberg, H. A Survey of Methods for Deter-  
mining Stability Parameters of  
an Airplane from Dynamic Flight  
Measurements:  
NACA TN 2340, Dec. 1950



TABLE 1

Model Data

Dimensions (see Fig. 4b)

Length	29½ inches
Width	20 inches
Base Area	2.68 feet <sup>2</sup>
Equivalent Diameter	22 inches
Inlet Fan Area	0.35 feet <sup>2</sup>
Exit Area of Peripheral Jets	0.101 feet <sup>2</sup>
Exit Area of Stability Jets	0.0734 feet <sup>2</sup>
Exit Area of Propulsion ducts	0.014 feet <sup>2</sup>
Perimeter of Peripheral Jets	6.08 feet

For a Fan R. P. M. of 13, 500:

Inlet mass flow =  $39.4 \times 10^{-3}$  slugs/sec.

Jet momentum thrust = 1.84 lbs.

$$\begin{array}{llll} l_1 = 14.914 & l_2 = -10.5 & l_3 = -15.774 & l_4 = -.454 \\ l_5 = -.594 & l_6 = -.43 & & \end{array}$$

For vehicle wt. 3.08 lbs.:  $i_a = 5.1$ ,  $i_b = 16.1$ ,  $i_c = 20$ ,  
 $i_{cf} = .00425$ ,  $\gamma = 48.7$ ,  
 $t^* = .0331$

For vehicle wt. 3.75 lbs.:  $i_a = 6.2$ ,  $i_b = 17.4$ ,  $i_c = 22.25$

For vehicle wt. 4.63 lbs.:  $i_a = 7.15$ ,  $i_b = 19.2$ ,  $i_c = 24.5$

TABLE 2

The Nondimensional System

Dimensional Quantity	Divisor	Non-Dimensional Quantity
X Y Z (force)	$J = \rho V_J^2 A_J$	$C_x C_y C_z$
L M N (moment)	J. Deq.	$C_l C_m C_N$
U V W (velocity)	$U_0$	$\hat{u}, \beta, \alpha$
p q r (angular rotation)	$1/t^*$	$\hat{p} \hat{q} \hat{r}$
$\dot{\beta} \dot{\alpha}$ (angular rotation)	$1/t^*$	$\hat{D}\beta \hat{D}\alpha$
m (mass)	$\rho A_J$ Deq.	$\mu$
A B C E (inertia)	$\rho A J$ Deq. <sup>3</sup>	$i_A, i_B, i_C, i_E$
t (time)	$t^* = \text{Deq.} / V_J$	$\hat{t}$
$\omega$ (2nf)	$1/t^*$	$\gamma$
h (height)	Deq.	H

Whenever p, q or r appear as a subscript (i. e.  $C_{lp}$ ) regard the subscript as being nondimensional (i. e.  $C_{l\hat{p}} = C_{lp}$ ). Furthermore  $t^*$  is a means for nondimensionalizing time; it should not be confused as a cable influence.

TABLE 3

Experimentally Extracted Derivatives (Mean Value)

H	$C_{MH}$	$C_{M\dot{H}}$	$C_{M\theta}$	$C_{Mq}$	$C_{M\theta H}$
.070	- .4	1.1	- .8	-1.9	4.
	-1.8	1.6	-1.0	-2.3	34.
	- .2	.3	- .61	-1.3	-38
.054	-1.4	3.7	-1.1	-3.0	32.
	-1.1	2.9	-1.2	-3.0	41.
	-2.3	2.7	- .9	-2.5	-32.
.043	- .6	3.8	-1.2	-4.4	-37.
	-2.2	4.4	-1.7	-5.8	54.
	-2.5	2.2	-1.9	-3.9	58.

H	$C_{ZH}$	$C_{Z\dot{H}}$	$C_{Z\theta}$	$C_{Zq}$	$C_{Z\varphi}$
.070	12.7	32.	2.0	15.	.2
	12.5	17.	6.8	8.	11.9
	13.6	28.	3.0	12.	2.1
.054	28.9	80.	3.5	41.	15.2
	26.4	77.	5.5	36.	17.4
	33.6	75.	7.8	40.	35.0
.043	50.4	85.	10.5	60.	26.5
	33.0	24.	13.2	18.	2.9
	28.5	44.	6.9	8.	2.0

H	$C_{ZH^2}$	$C_{LP}$	$C_{L\psi}$	$C_{Lr}$	$C_{L\varphi}$
.070	-793	- .27	.07	1.6	- .24
	-1156	- .48	.81	1.6	- .94
	-627	- .52	.36	2.0	- .25
.054	1032	- .08	.06	.94	- .17
	701	- .30	.37	.89	- .37
	2000	- .68	.15	1.1	- .52
.043	- -	-1.03	.05	.51	+ .26
	-3000	- .19	.34	.50	- .37
	-2000	- .56	.34	.65	- .03

# Contrails

TABLE 3 (Cont'd)

H	$C_{LH}^*$	$C_{LH\varphi}$	$C_{N\varphi}$	$C_{N\psi}$	$C_{N\gamma}$
.070	-.01	-54.	-1.1	.11	-1.7
	-.94	-157	-1.5	.12	-.5
	-.69	95.	-1.1	-.28	-2.2
.054	-.32	-54.	-1.2	.4	-2.1
	-.09	-78.	-1.6	-.26	-2.1
	-.14	-123	-2.4	0	-2.1
.043	-.70	-165	-5.9	-.39	-.8
	-1.51	+437	-1.1	-.09	-1.4
	-.57	+264	-3.3	-.24	-1.8

H	$C_{N\varphi}$
.070	-.44
	-.24
	-.40
.054	-.20
	-.70
	-.54
.043	-.25
	-.70
	-.57

Wt.	$\mu$	$C_{ZH}^*$	$C_{LH}^*$	$C_{Z\varphi}^*$	$C_{ZH}^*$	$C_{\ell\varphi}^*$	$C_{N\psi}^*$
3.08	126.9	.180	-.086	.86	$1 \times 10^{-5}$	-.42	-.42
3.75	154.5	.219	-.105	1.05	$C_{LH}^*$	-.52	-.52
4.63	190.5	.270	-.130	1.30	$4.8 \times 10^{-6}$	-.62	-.62

# Contrails

TABLE 4

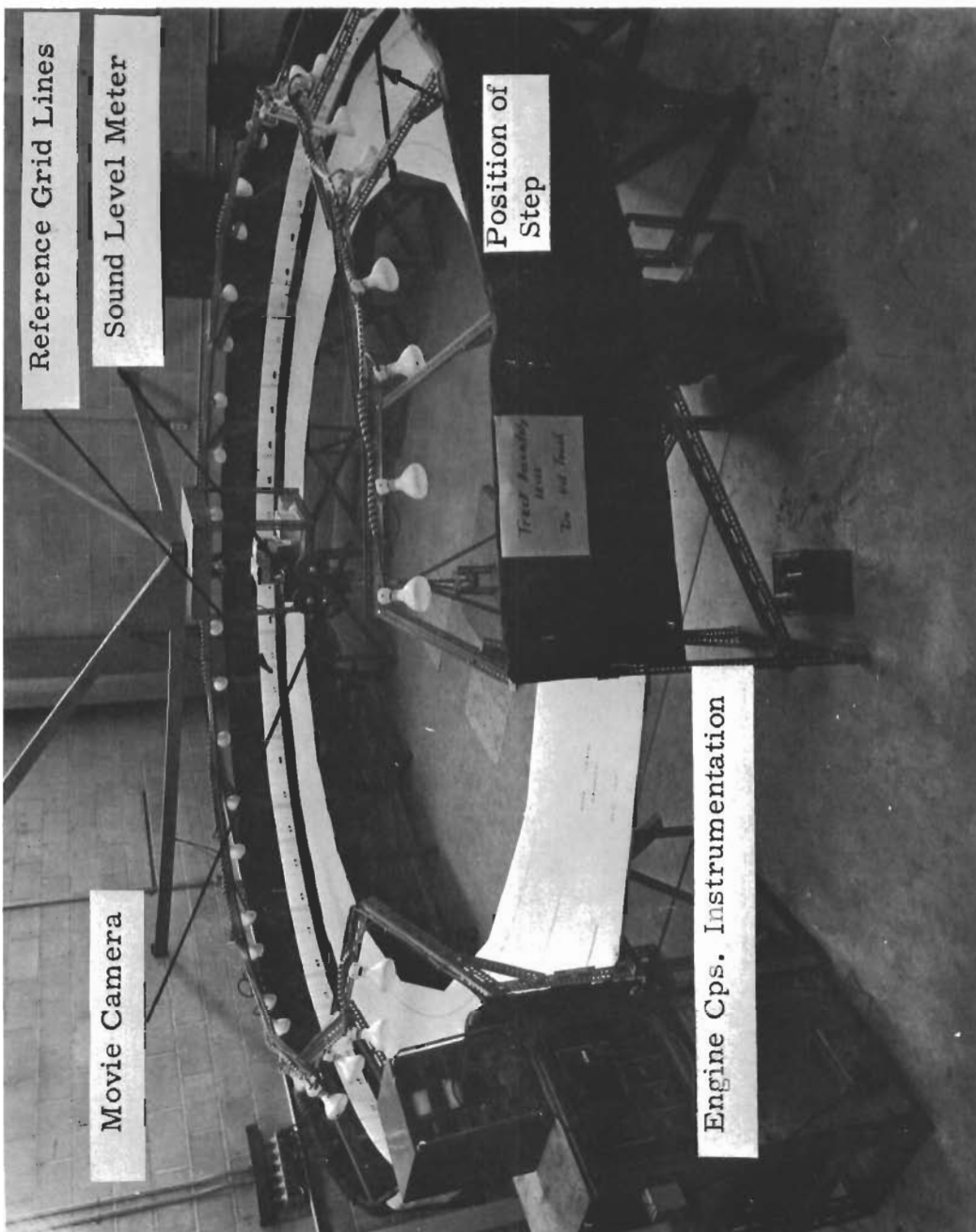
Comparison of Predicted and Experimental  
Errors (To Nearest 5%)

	(1)	(2)	(3)		(4)	(5)	(6)
Derivative	Predicted	Expt'l	$E_m$	Derivative	Predicted	Expt'l	$E_m$
	$\sigma$ (%)	$\sigma$ (%)	(%)		$\sigma$ (%)	$\sigma$ (%)	(%)
$C_{z_H}$	15	15	10	$C_{\lambda_P}$	10	80	45
$C_{z_H}$	30	35	20	$C_{\lambda_y}$	40	70	40
$C_{z_{H^2}}$	> 240	190	110	$C_{\lambda_r}$	90	15	10
$C_{z_e}$	135	45	25	$C_{\lambda_\phi}$	150	120	70
$C_{z_q}$	15	45	25	$C_{\lambda_{H\phi}}$	15	70	40
$C_{z_\phi}$	130	105	60	$C_{\lambda_{H\phi}}$	175	65	370
$C_{m_H}$	105	70	40	$C_{z_P}$	70	45	25
$C_{m_H}$	145	50	30	$C_{z_y}$	5	>345	>200
$C_{m_\theta}$	15	15	10	$C_{z_r}$	10	50	30
$C_{m_q}$	40	15	10	$C_{z_\phi}$	< 5	45	25
$C_{m_{\theta H}}$	140	165	95				

NOTES

1. In columns (1) and (4),  $\sigma$  is the r. m. s. value of the deviations from the true value,  $\sigma = (\sum x_i^2 / n)^{1/2}$ , expressed as a percentage of the true value.
2. In columns (2) and (5),  $\sigma$  is the estimate of the standard deviation of a small sample,  $\sigma = (\sum x_i^2 / (n-1))^{1/2}$ , expressed as a percentage of the mean. The value given is the average for 3 heights.
3. Columns (3) and (6) are the estimate of the standard deviation of the mean  $E_m = (\sum x_i^2 / n(n-1))^{1/2}$ , as a percentage of the mean. The value given is the average for 3 heights.





Reference Grid Lines

Sound Level Meter

Position of Step

Movie Camera

Engine Cps. Instrumentation

Track Assembly  
1000  
200 100 50

Fig.1 UTIAS CIRCULAR TRACK

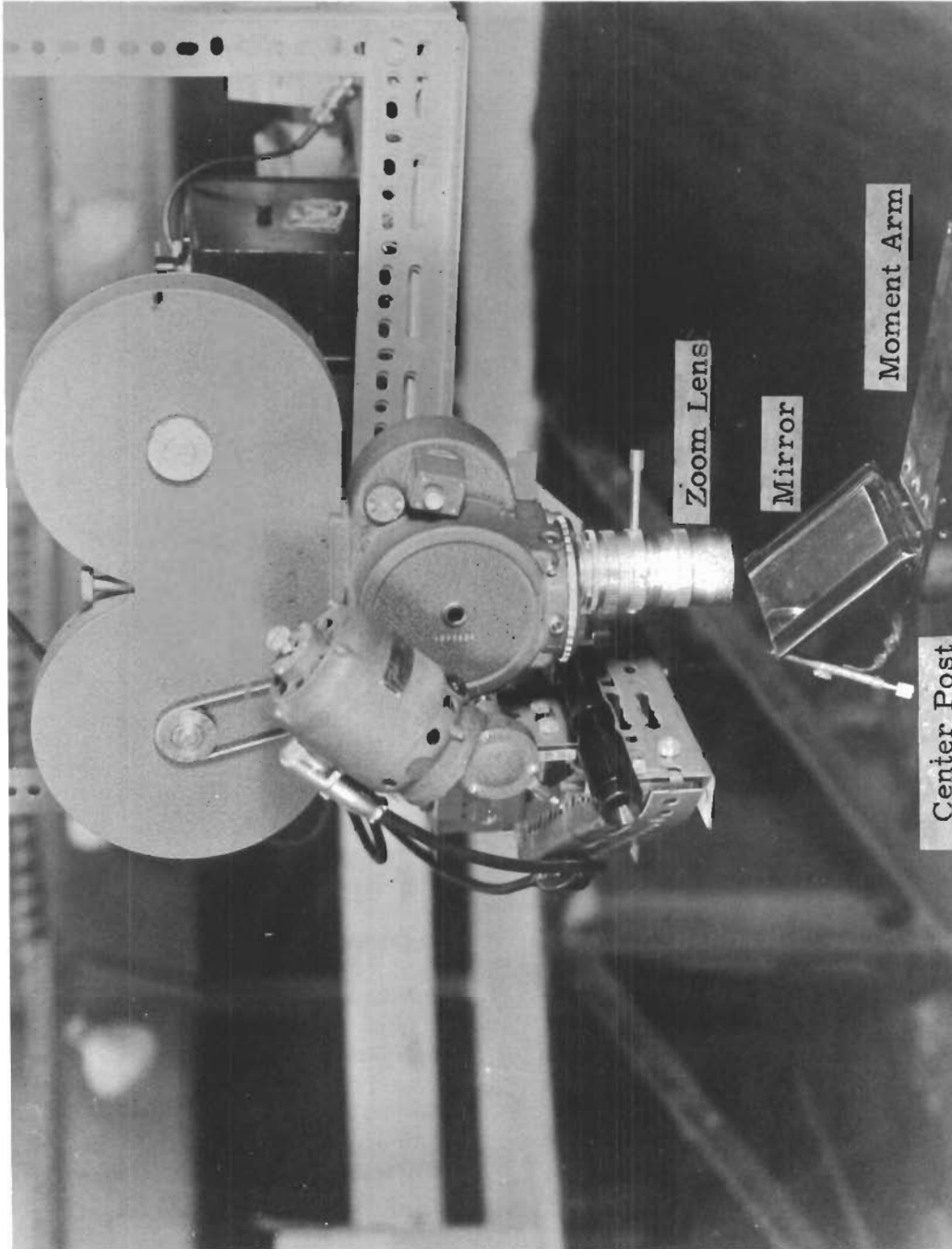
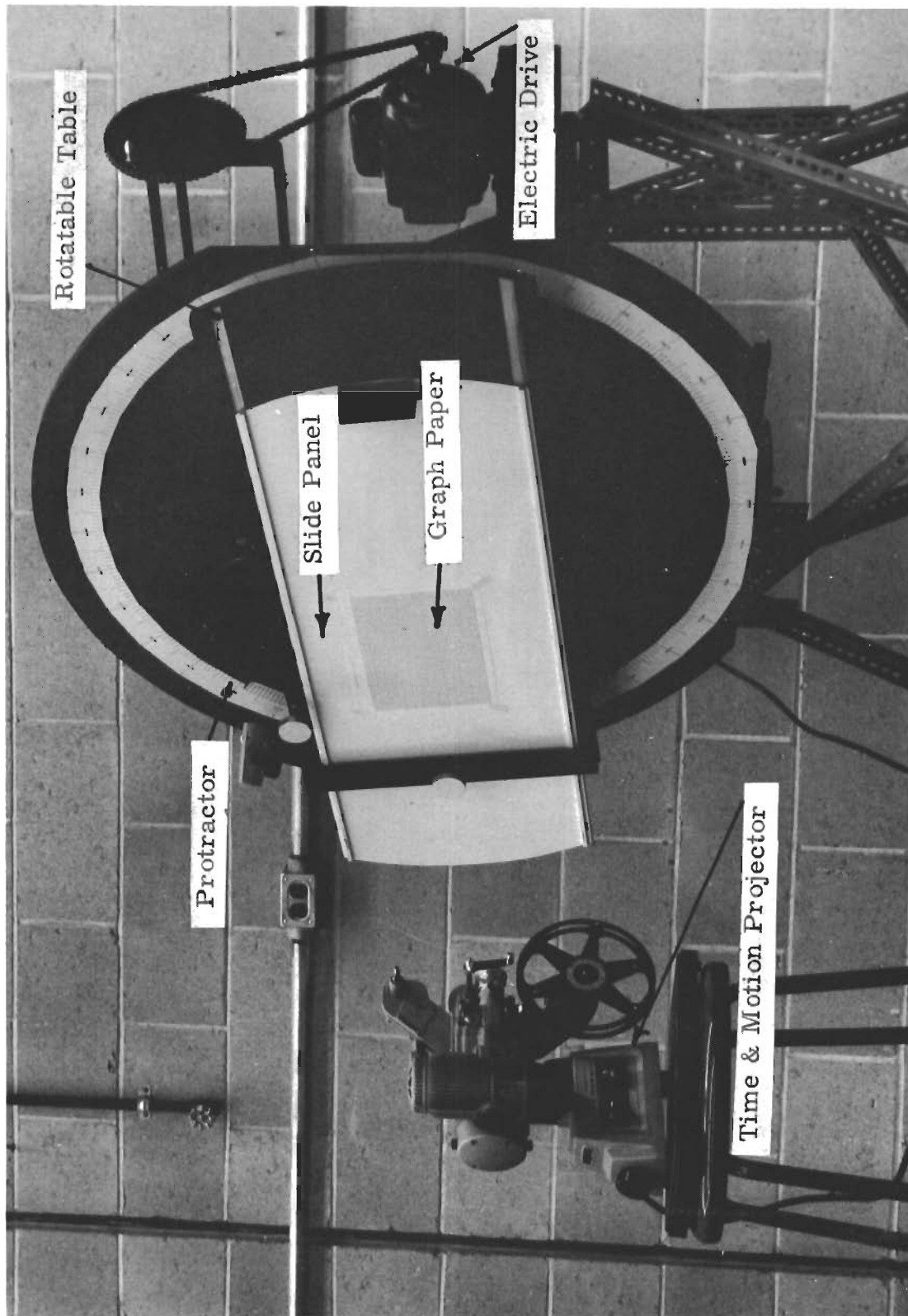


FIG. 2 THE CENTRE POST INSTALLATION



▲ FIG. 3 FILM ANALYSER

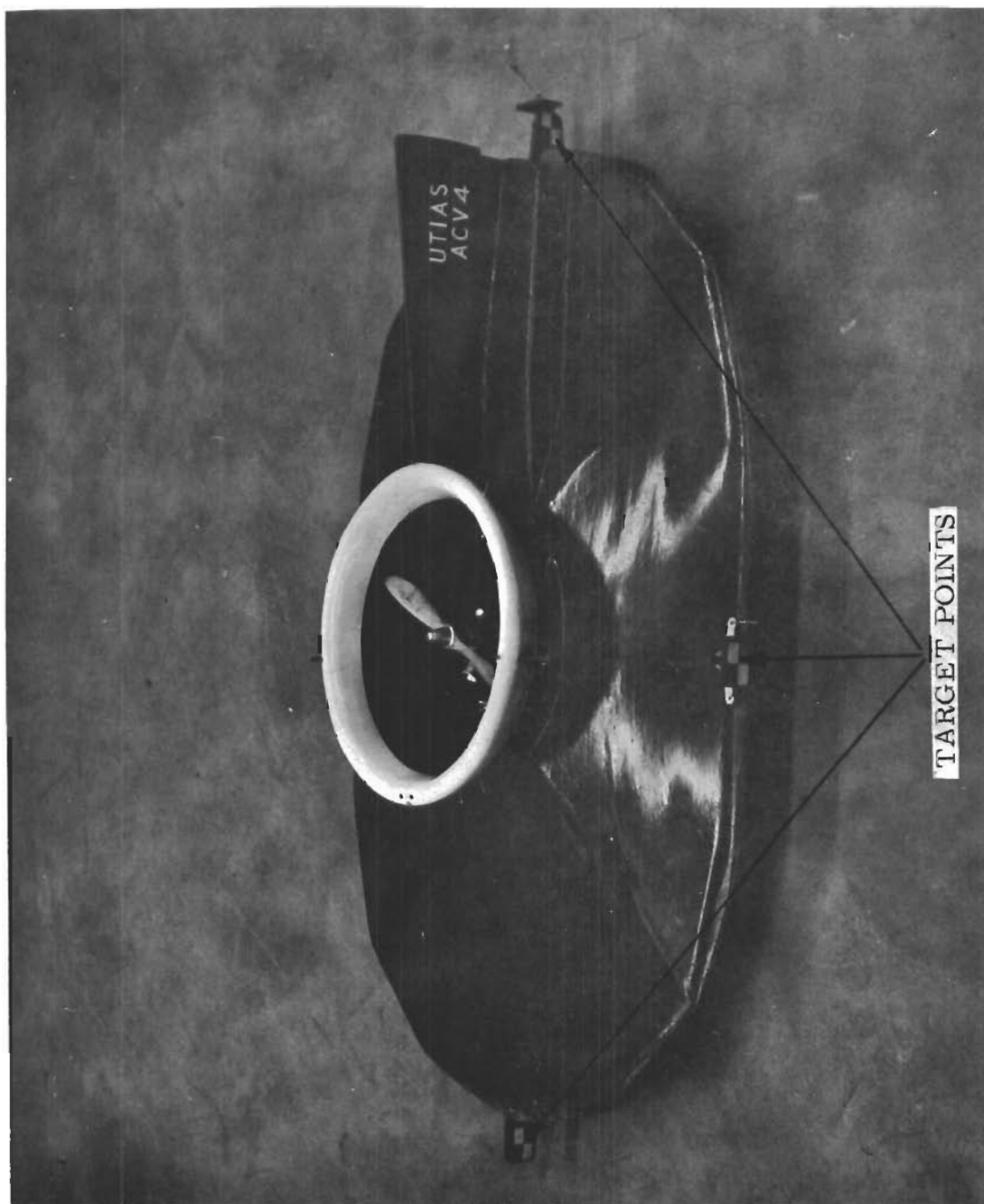


FIG. 4a THE EXPERIMENTAL ACV  
(COURTESY OF B. GOWANS - REF. 6)

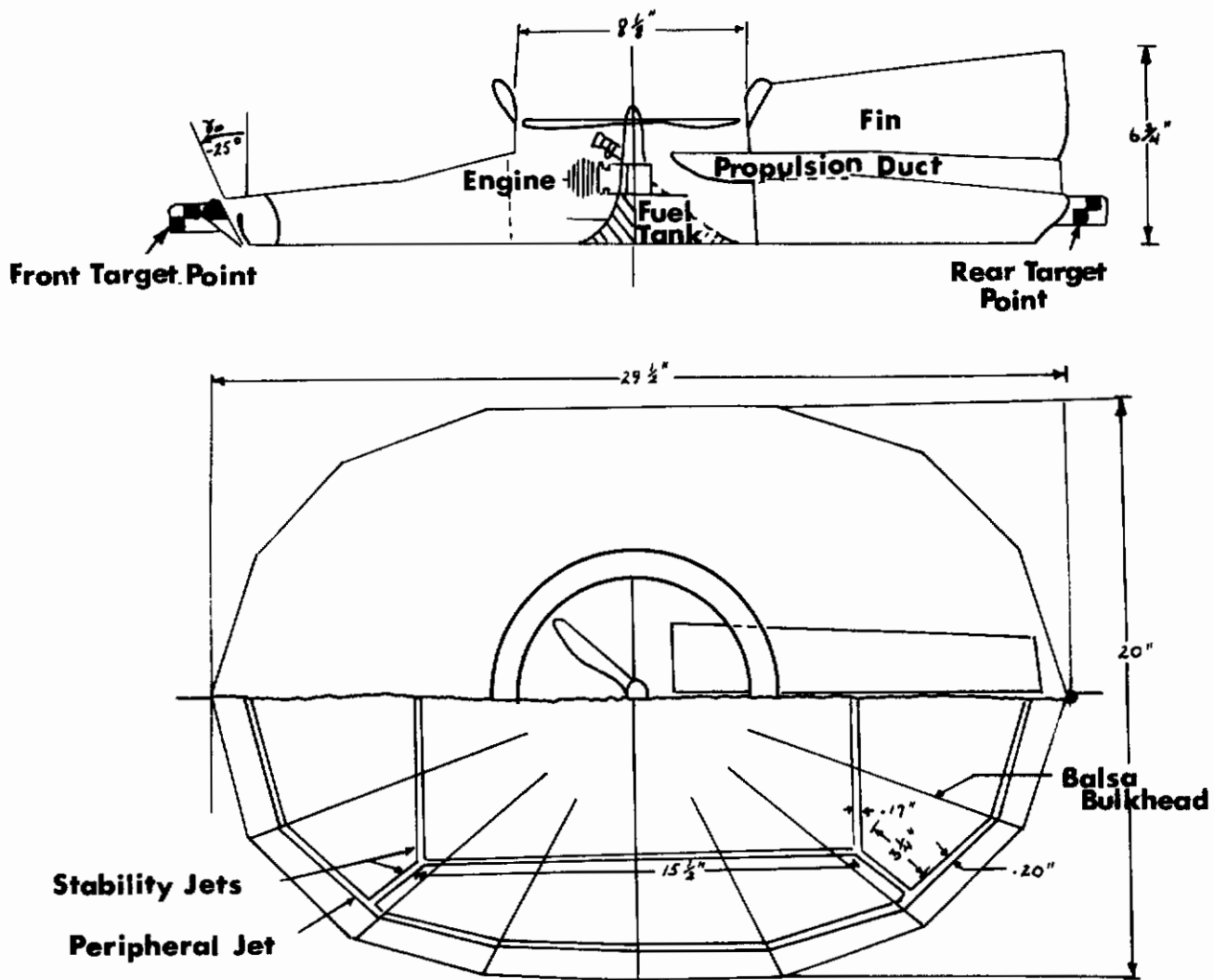


FIG. 4b THE SCHEMATIC OF THE ACV  
(COURTESY OF B. GOWANS - REF. 6)

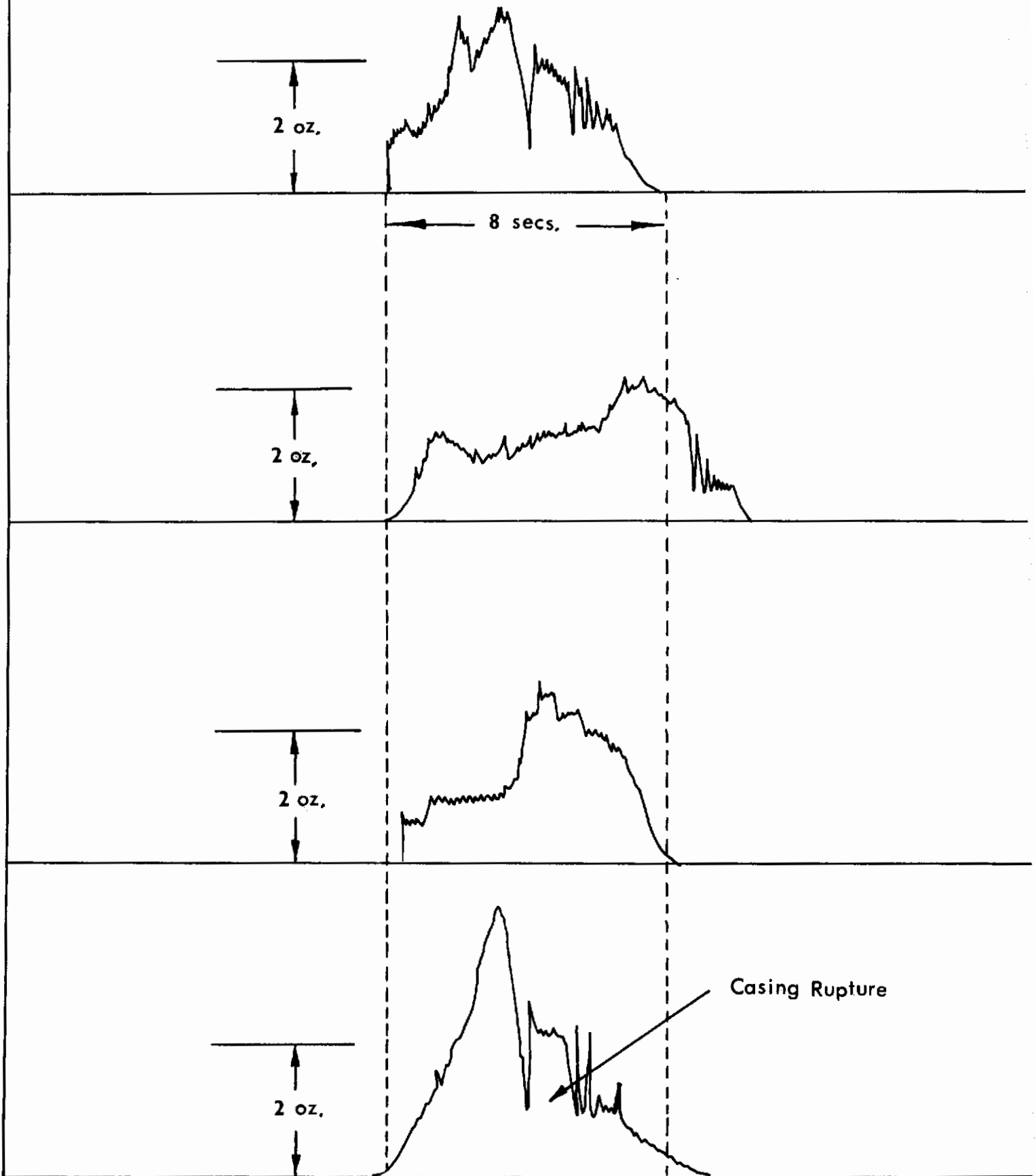


FIG. 5 TEST RESULTS OF JETEX UNIT - THRUST VS TIME

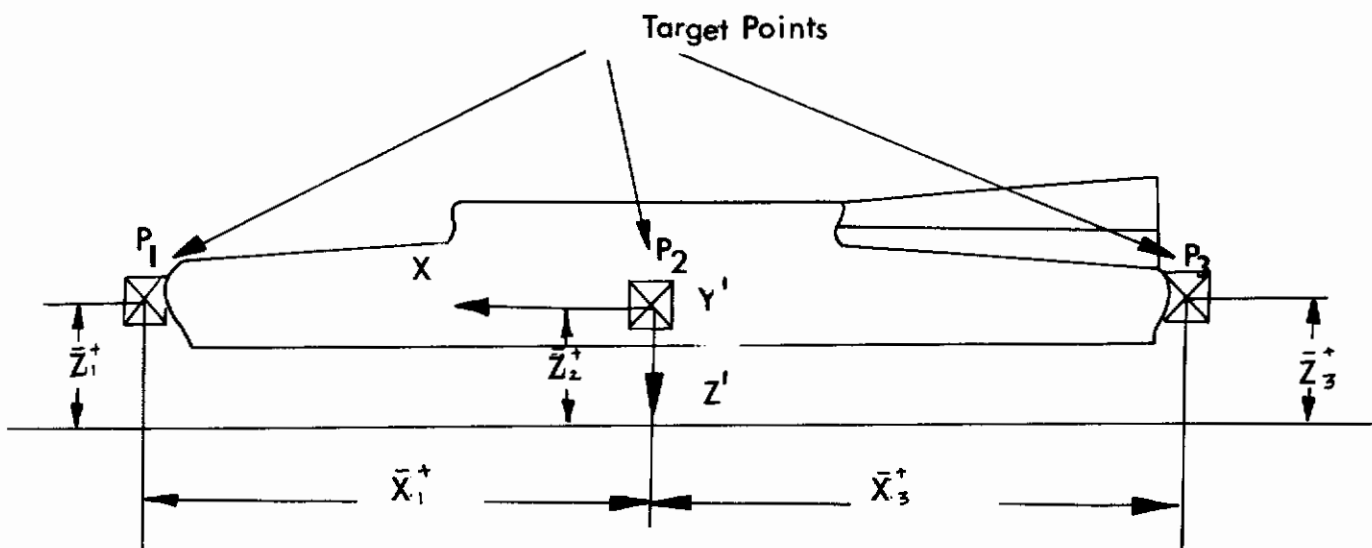


FIG. 6 THE TARGET POINT MEASUREMENTS

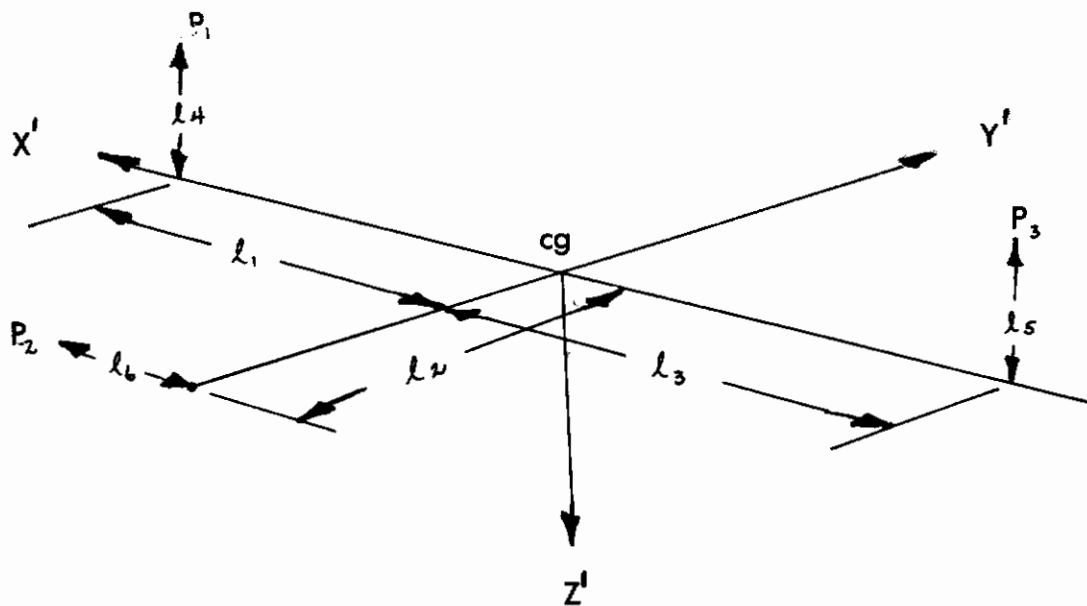


FIG. 7 TARGET POINTS RELATIVE TO BODY FIXED AXIS

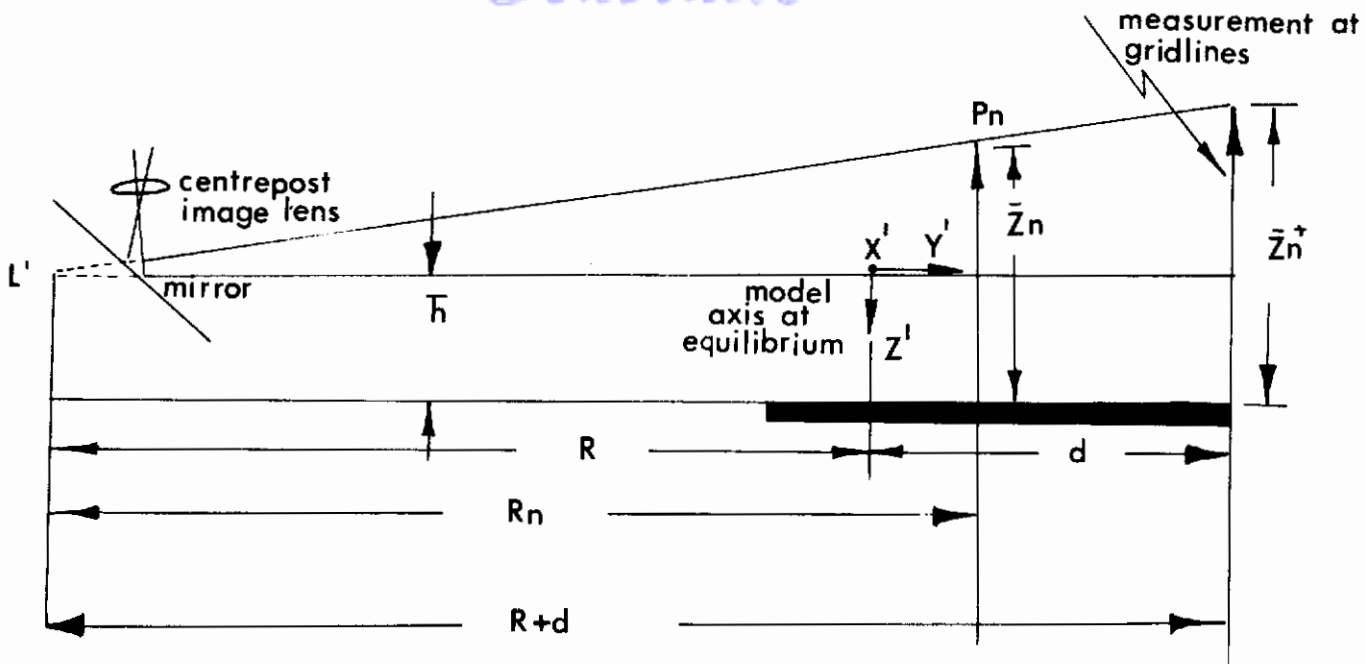


FIG. 8 VERTICAL PARALLAX CORRECTION

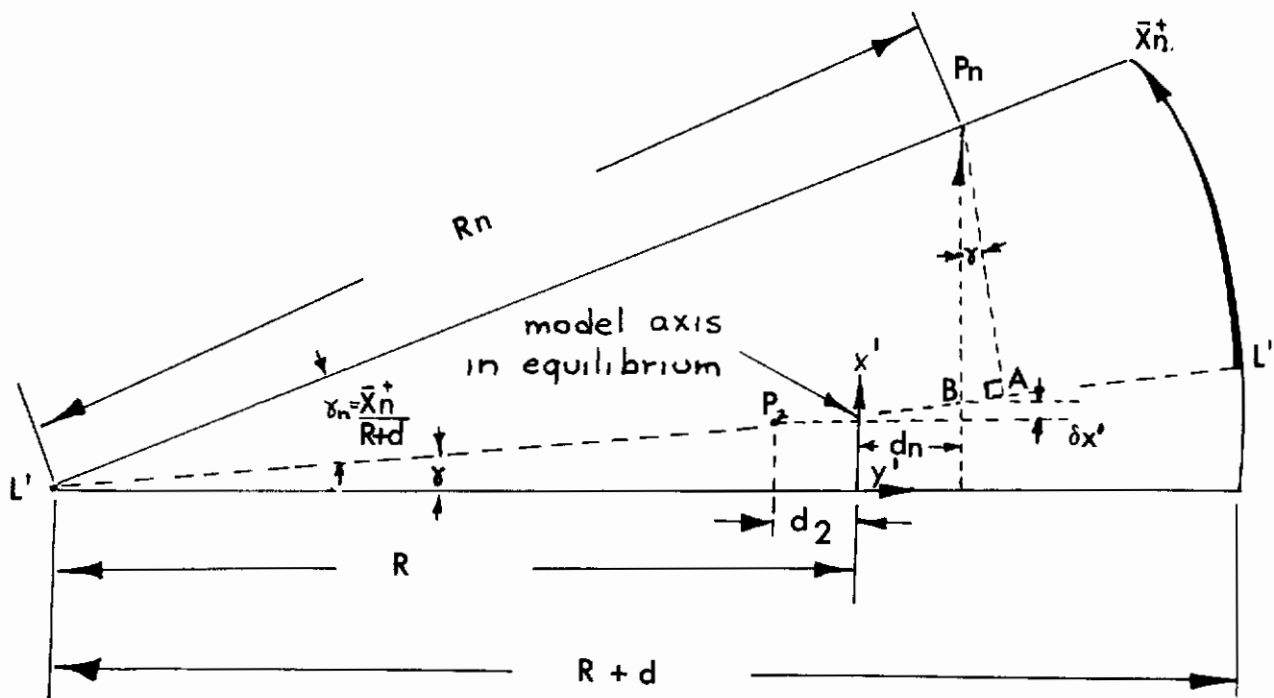


FIG. 9 HORIZONTAL PARALLAX AND GRID CURVATURE CORRECTION



# Contraails

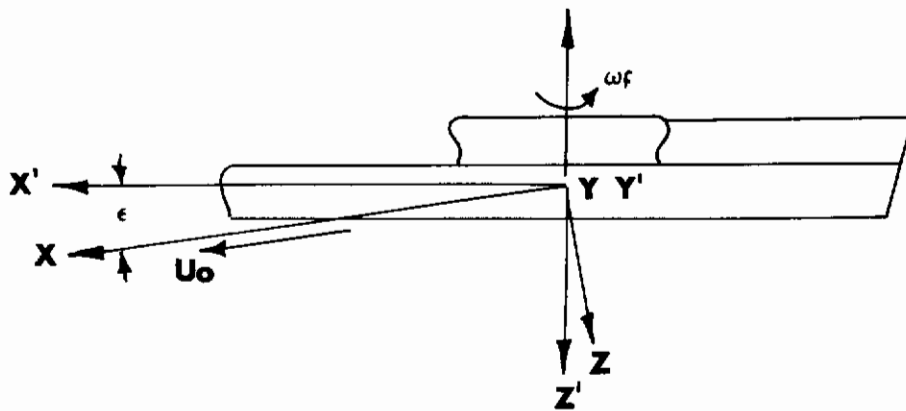


FIG. 10 AXES SYSTEMS FOR EQUATIONS OF MOTION

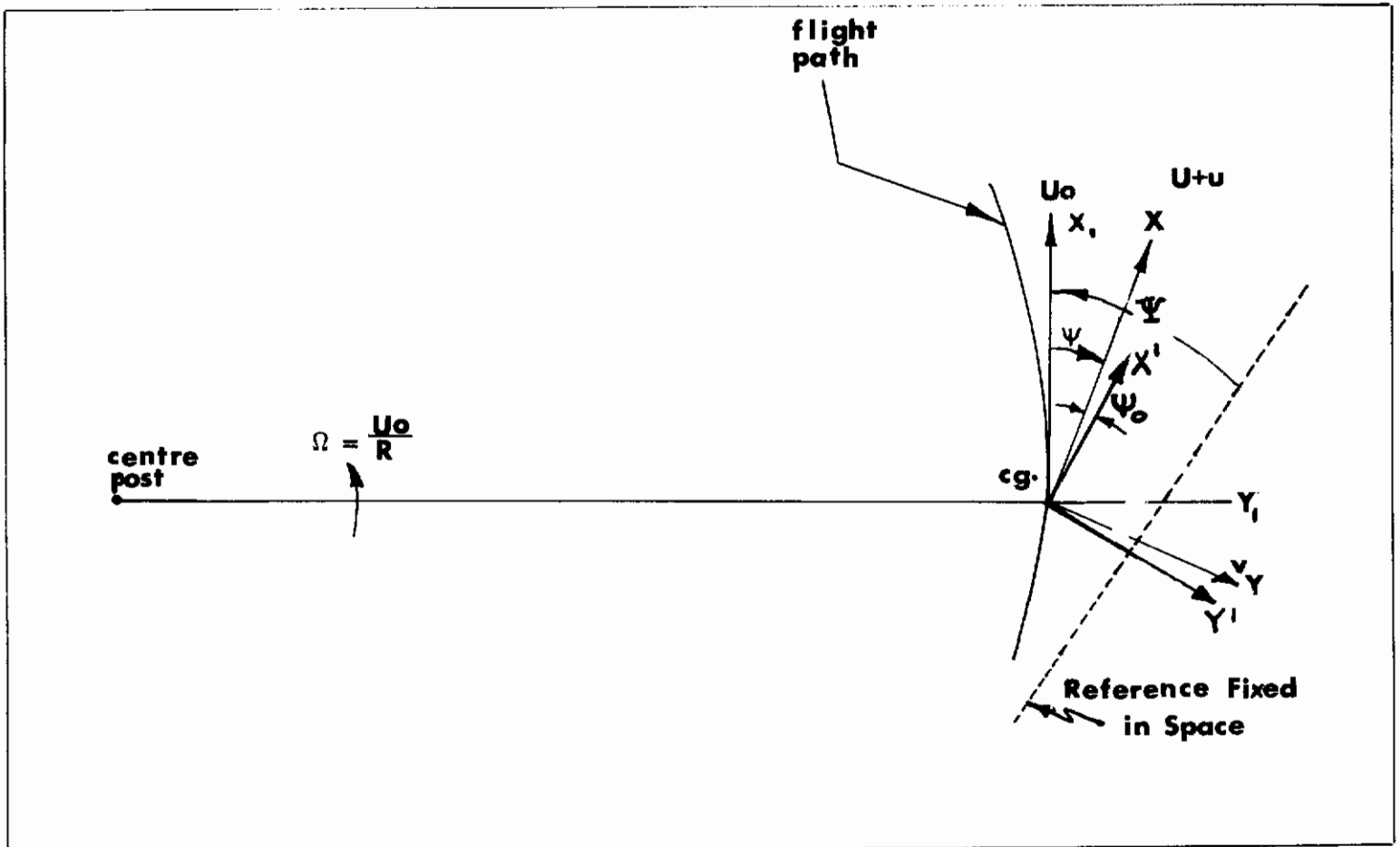


FIG. 11 THE VEHICLE'S FLIGHT PATH  
Page 85

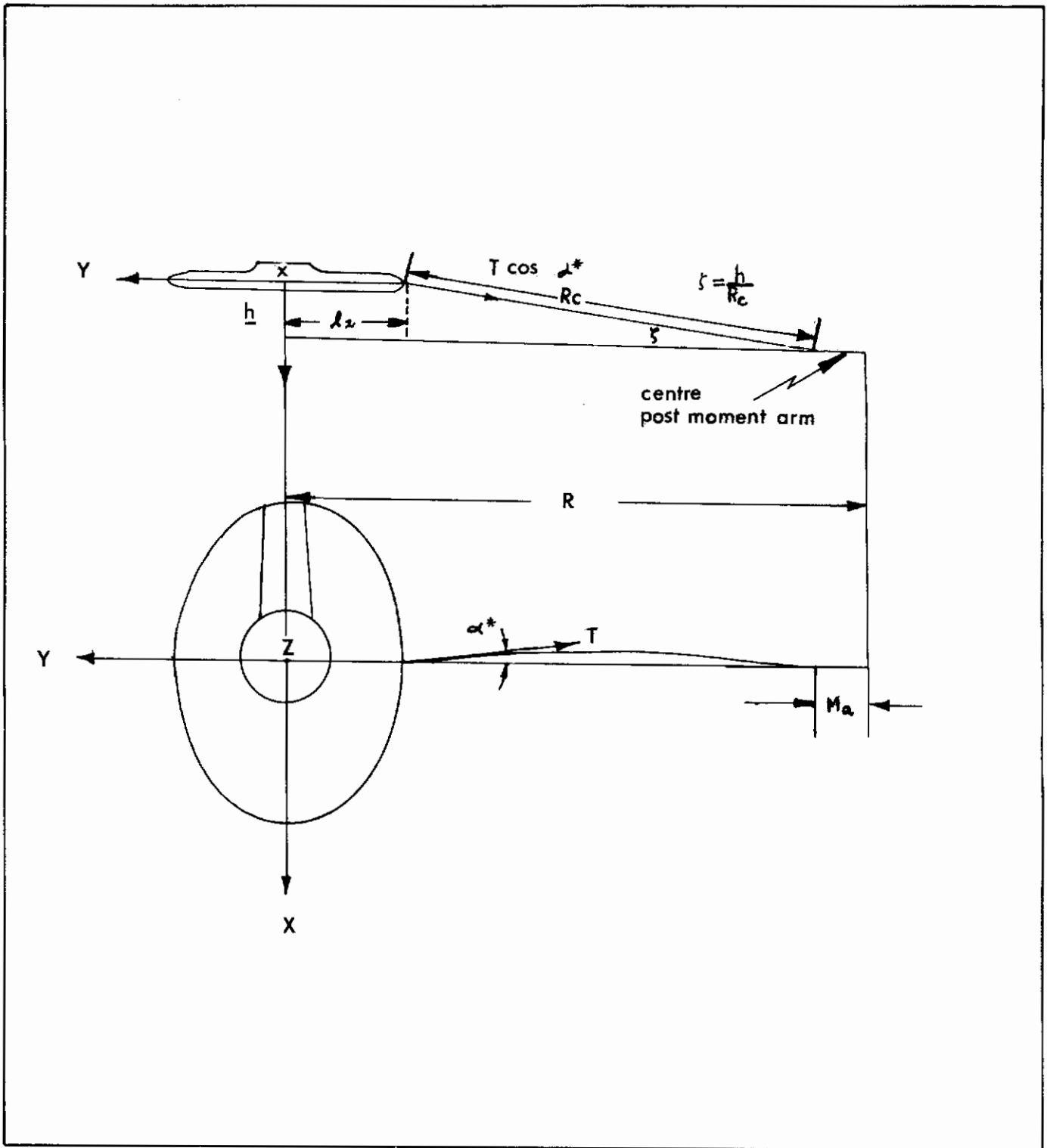


FIG. 12a THE CABLE HEIGHT DERIVATIVE



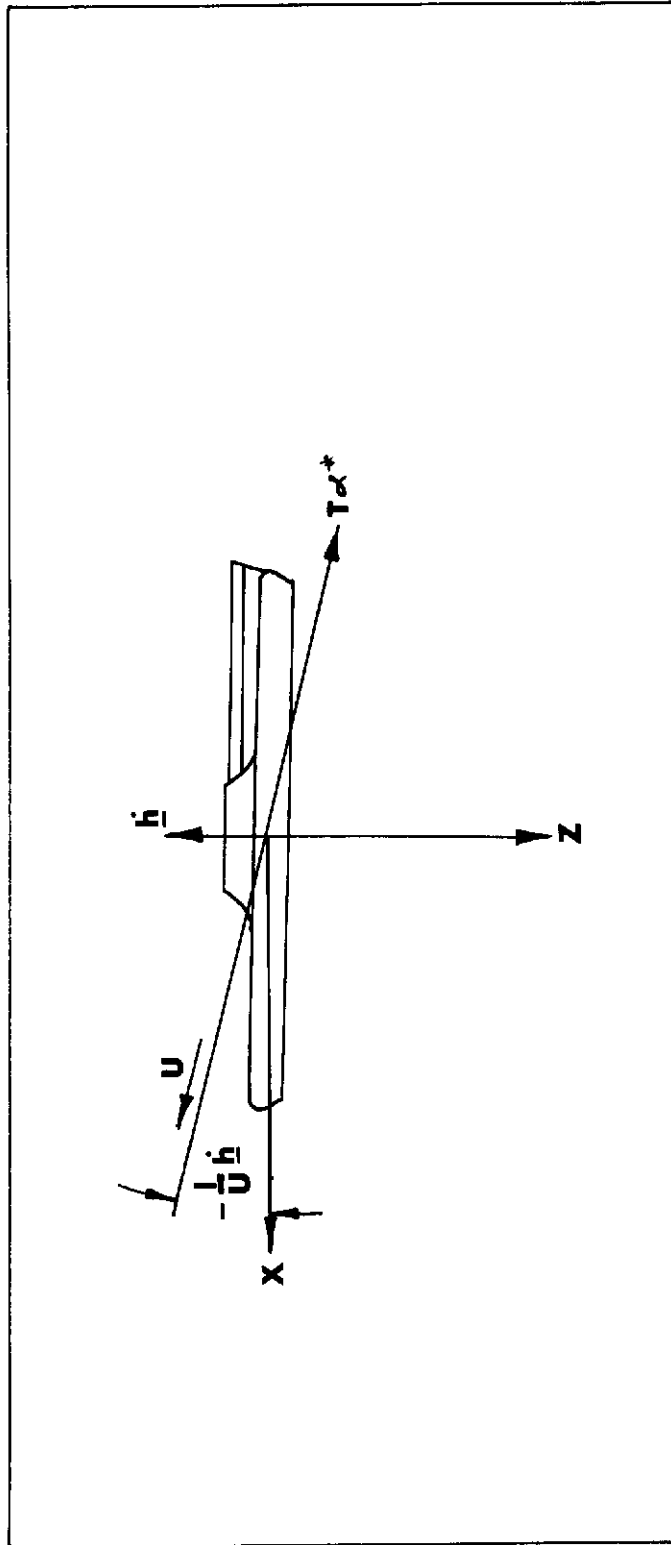


FIG. 12d THE CABLE PLUNGE DAMPING DERIVATIVE

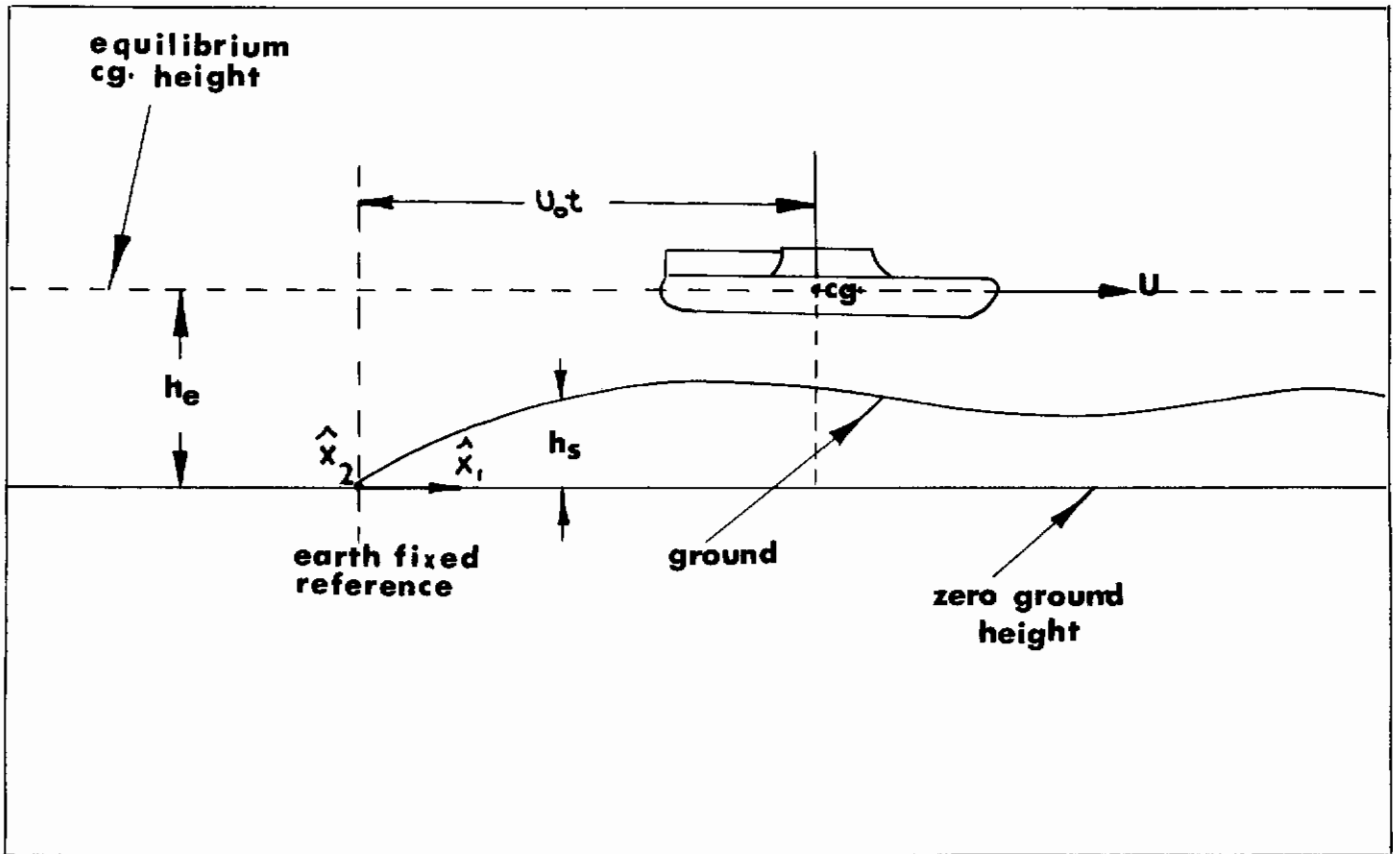


FIG. 13 GROUND INPUTS

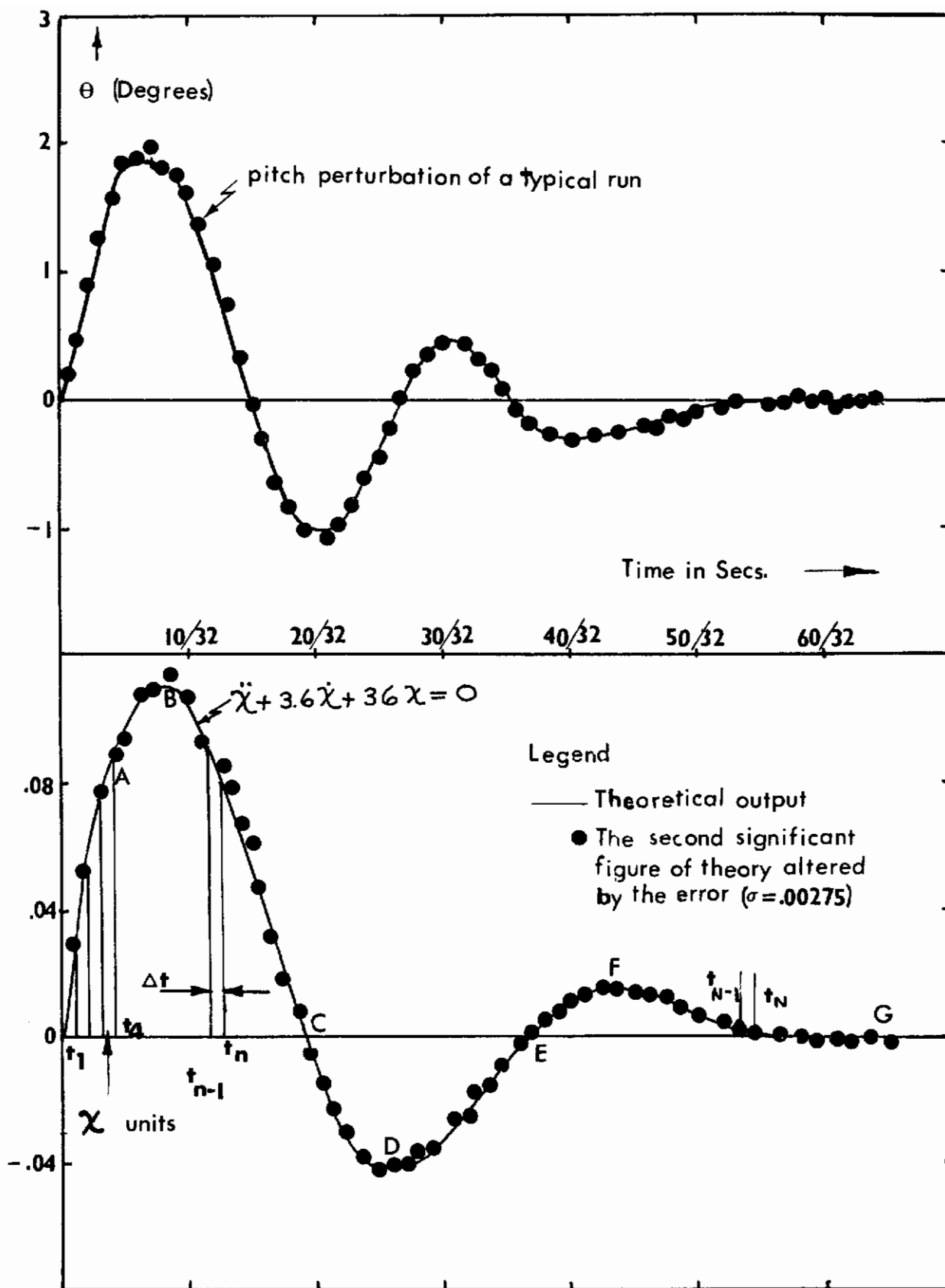


FIG. 14 A COMPARISON BETWEEN A TYPICAL PITCH PERTURBATION AND THE SIMULATED EXPERIMENTAL OUTPUT

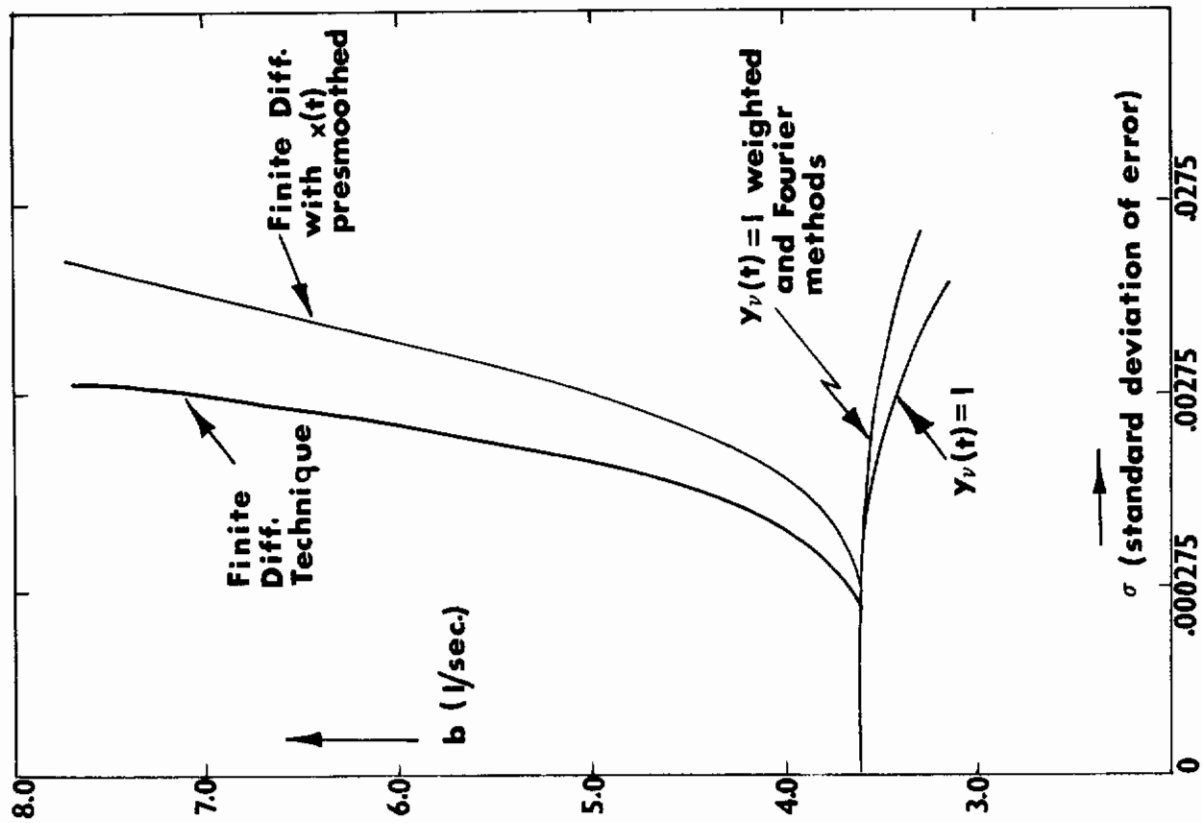
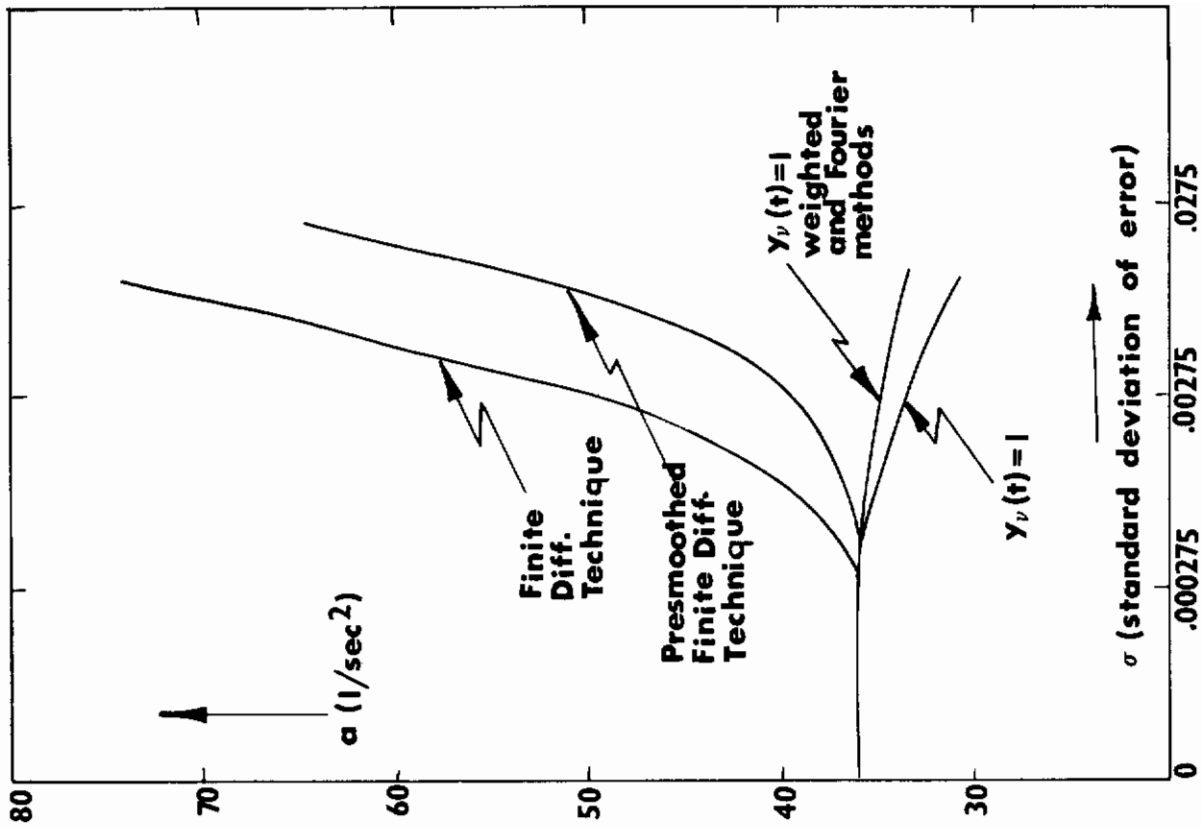


FIG. 15 THE EFFECT OF SCATTER ON COEFFICIENTS a AND b

# *Contrails*





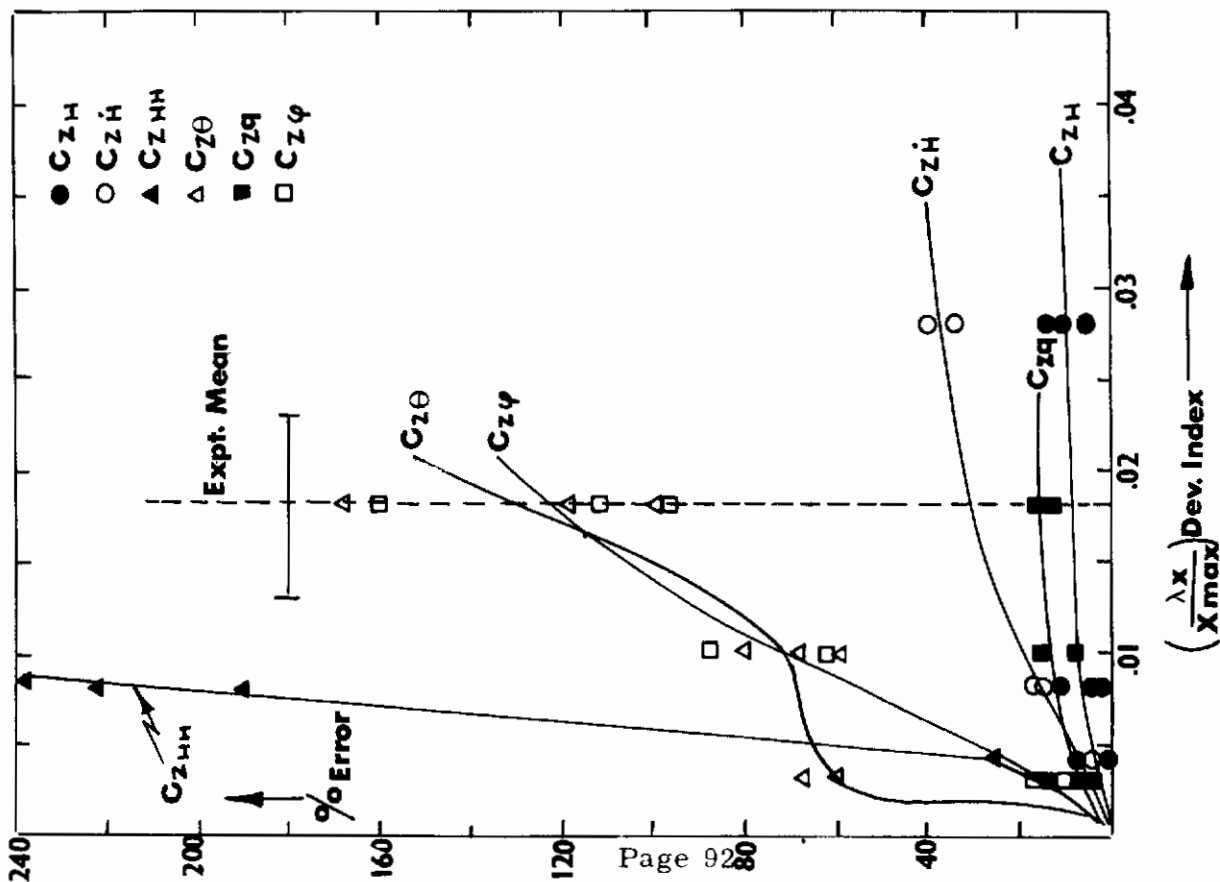
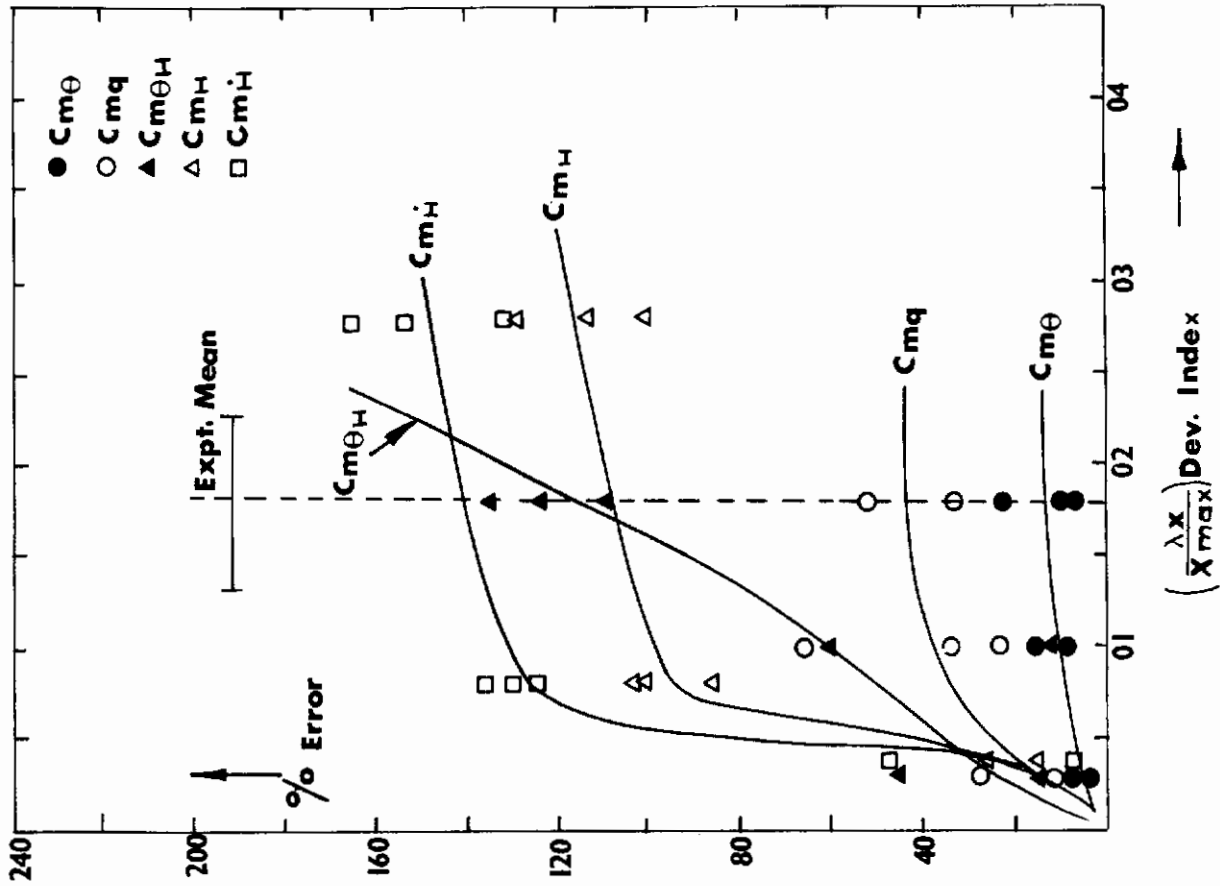


FIG. 17a THE EFFECT OF SCATTER ON THE FLIGHT DERIVATIVES

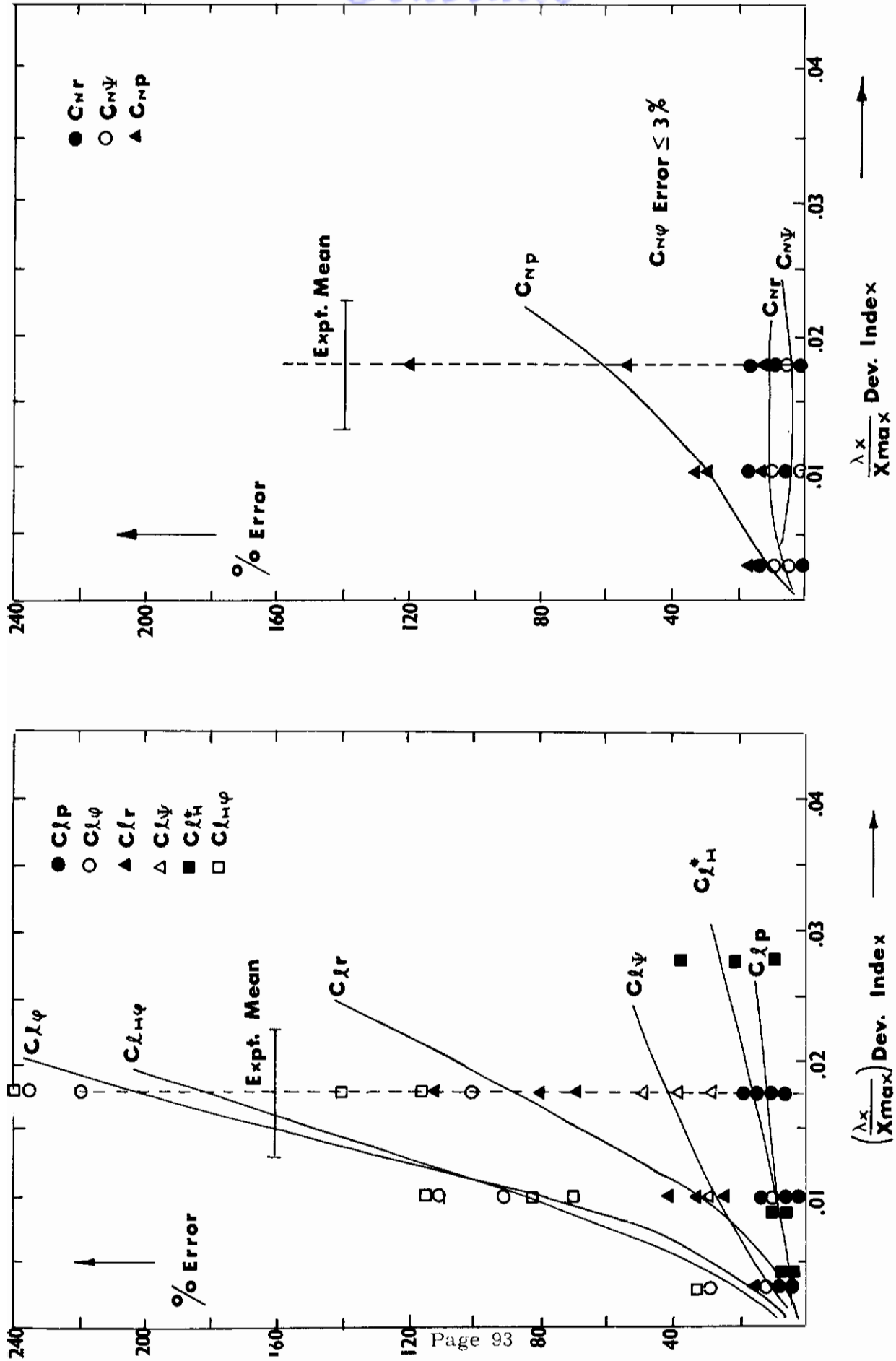


FIG. 17b THE EFFECT OF SCATTER ON THE FLIGHT DERIVATIVES

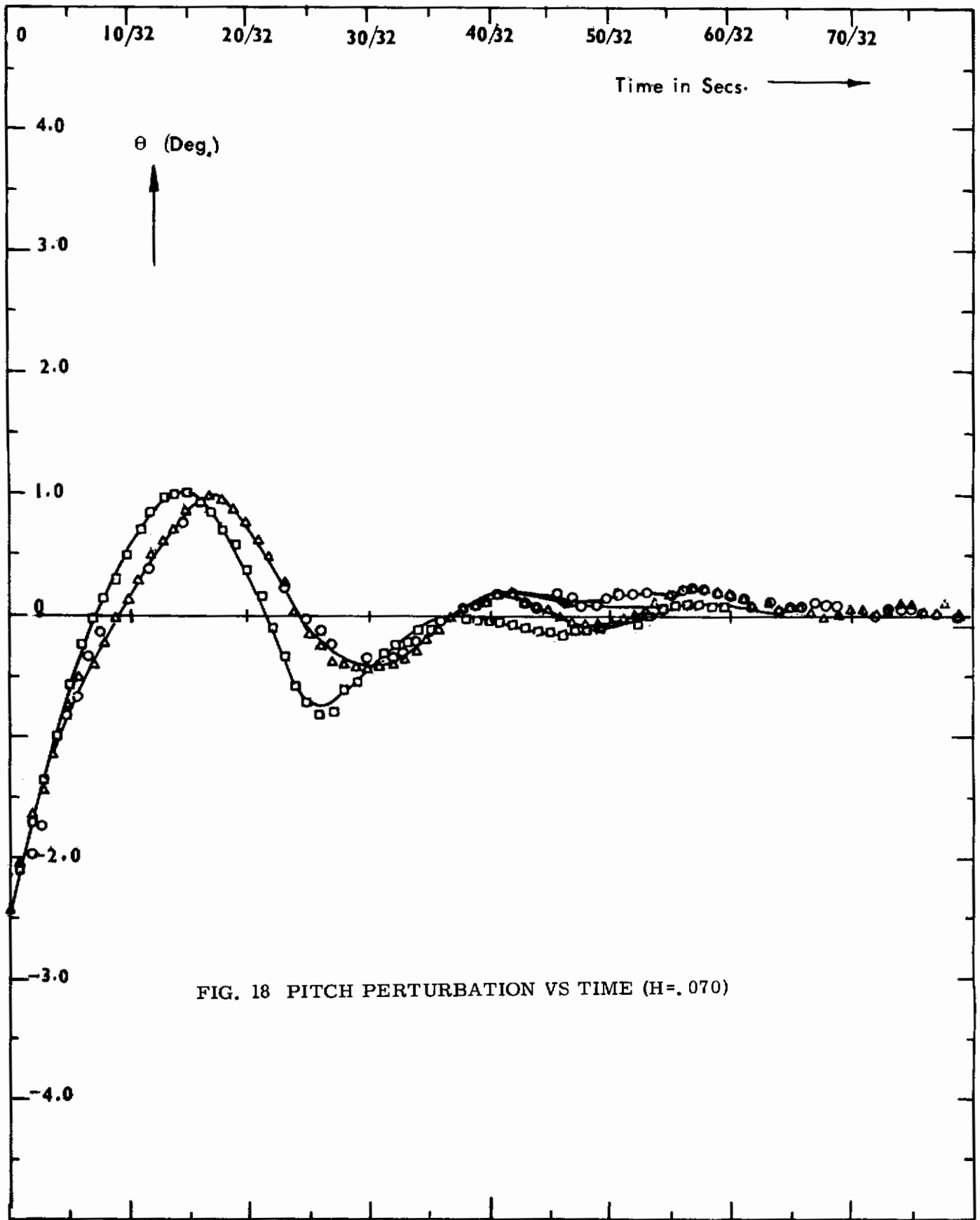


FIG. 18 PITCH PERTURBATION VS TIME (H=.070)

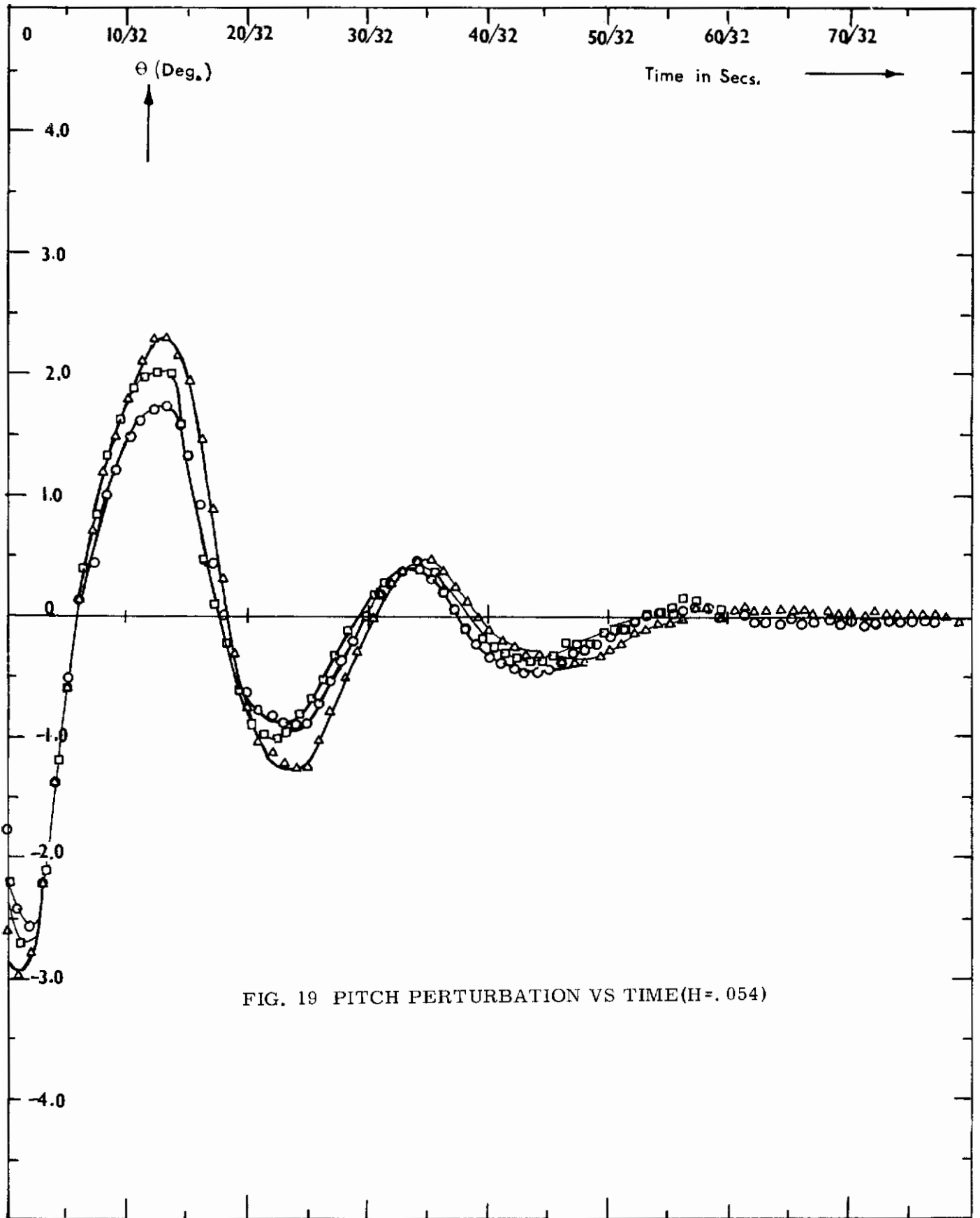


FIG. 19 PITCH PERTURBATION VS TIME(H=.054)

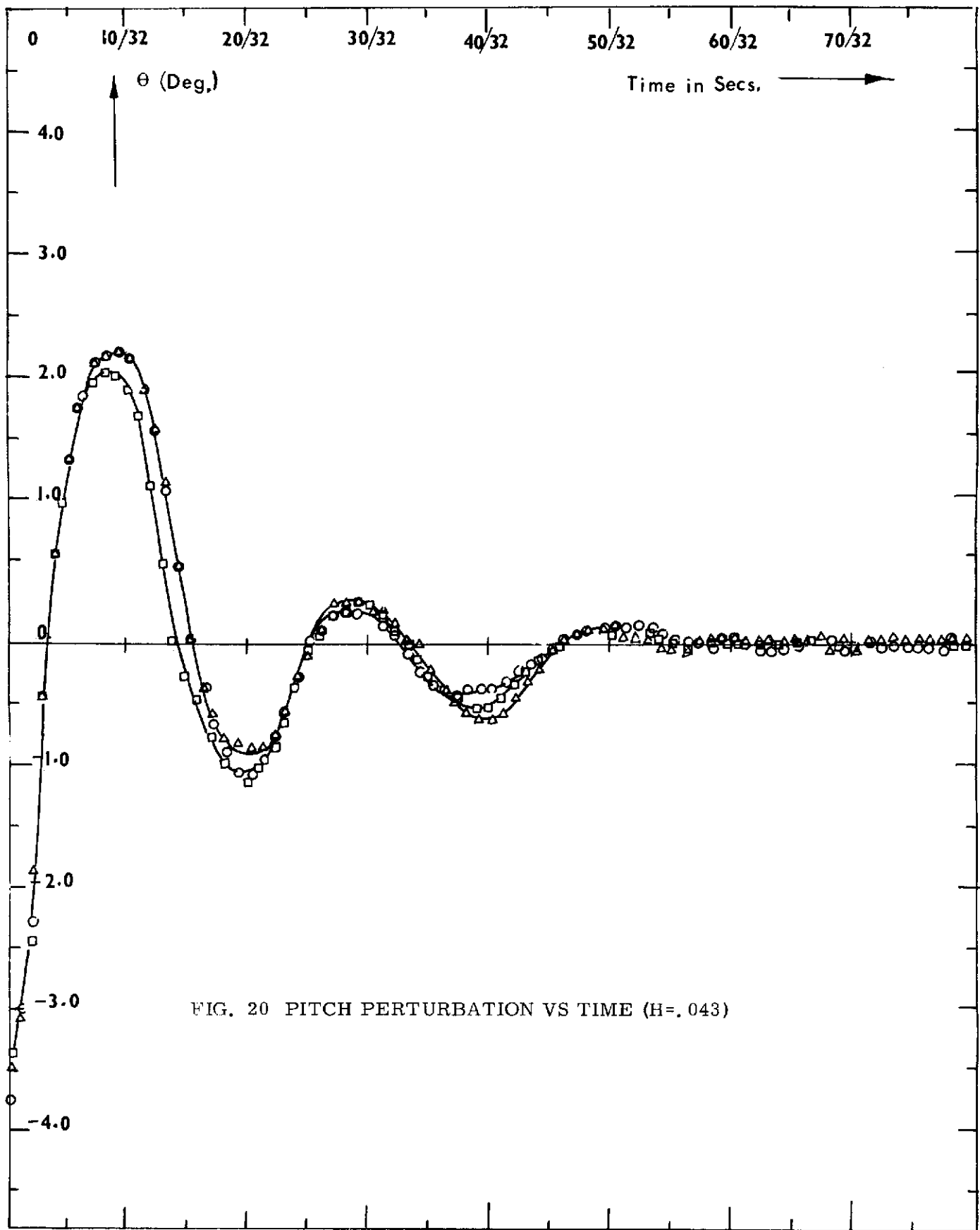


FIG. 20 PITCH PERTURBATION VS TIME (H=.043)

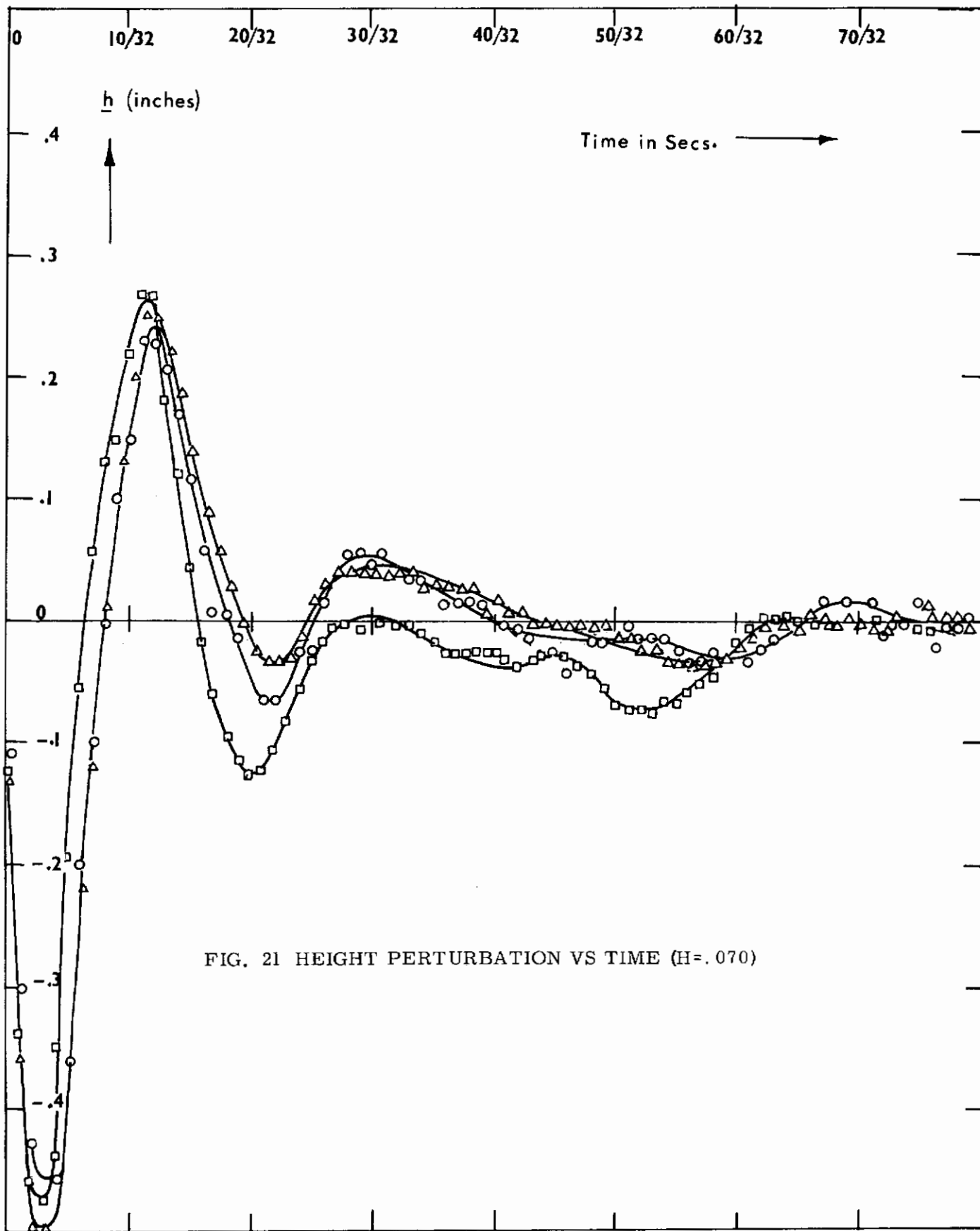


FIG. 21 HEIGHT PERTURBATION VS TIME (H=.070)

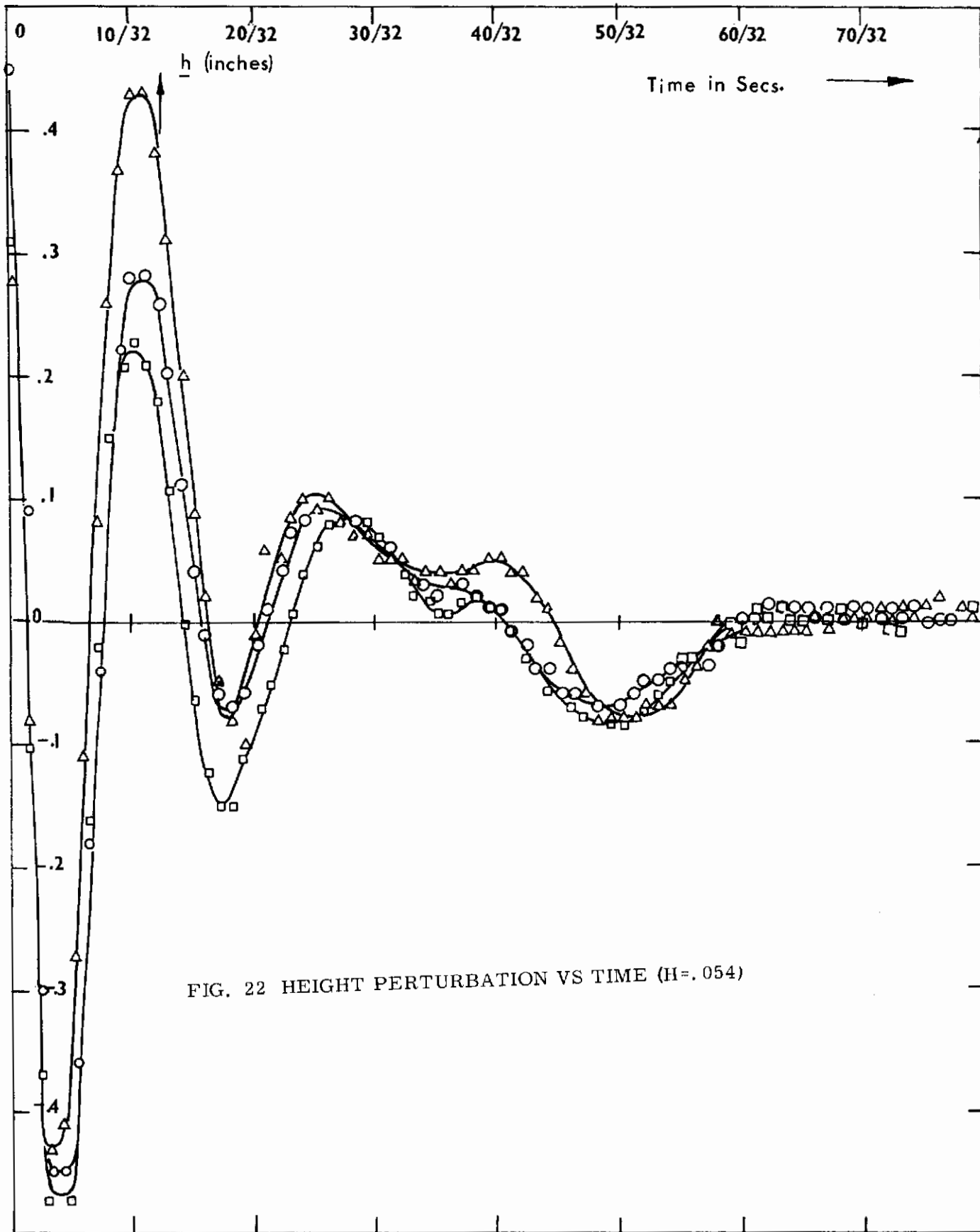


FIG. 22 HEIGHT PERTURBATION VS TIME (H=.054)



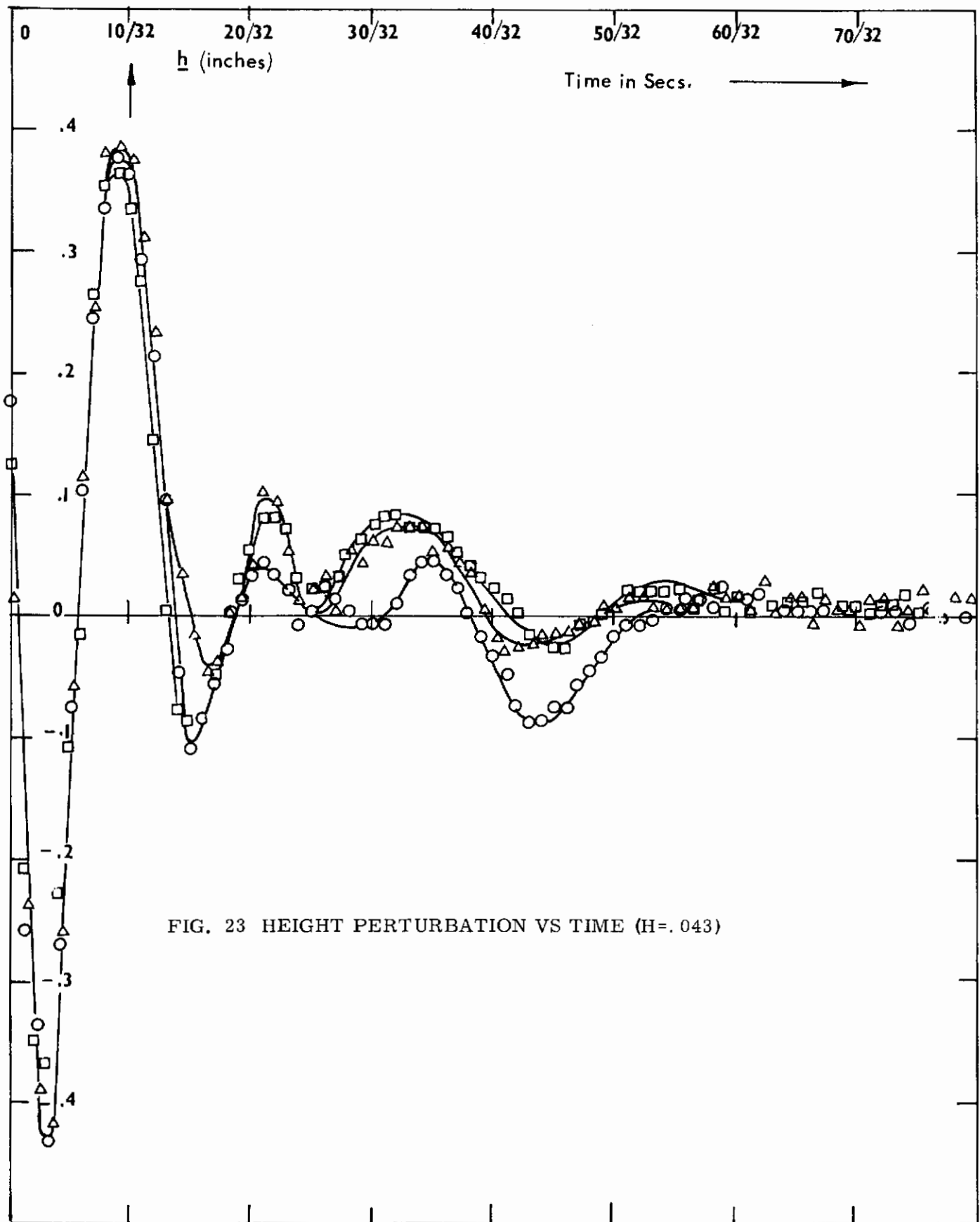


FIG. 23 HEIGHT PERTURBATION VS TIME (H=.043)

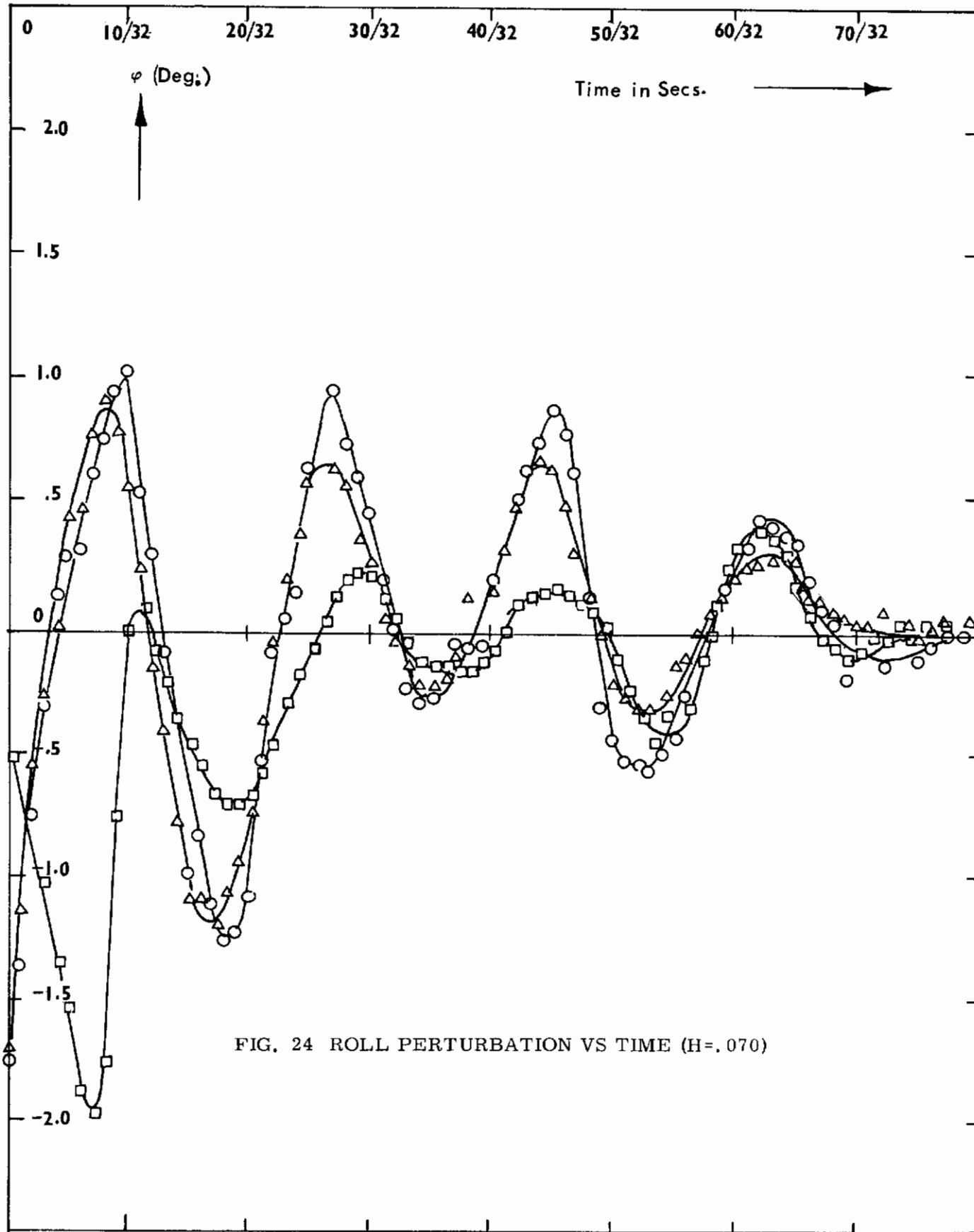


FIG. 24 ROLL PERTURBATION VS TIME (H=.070)

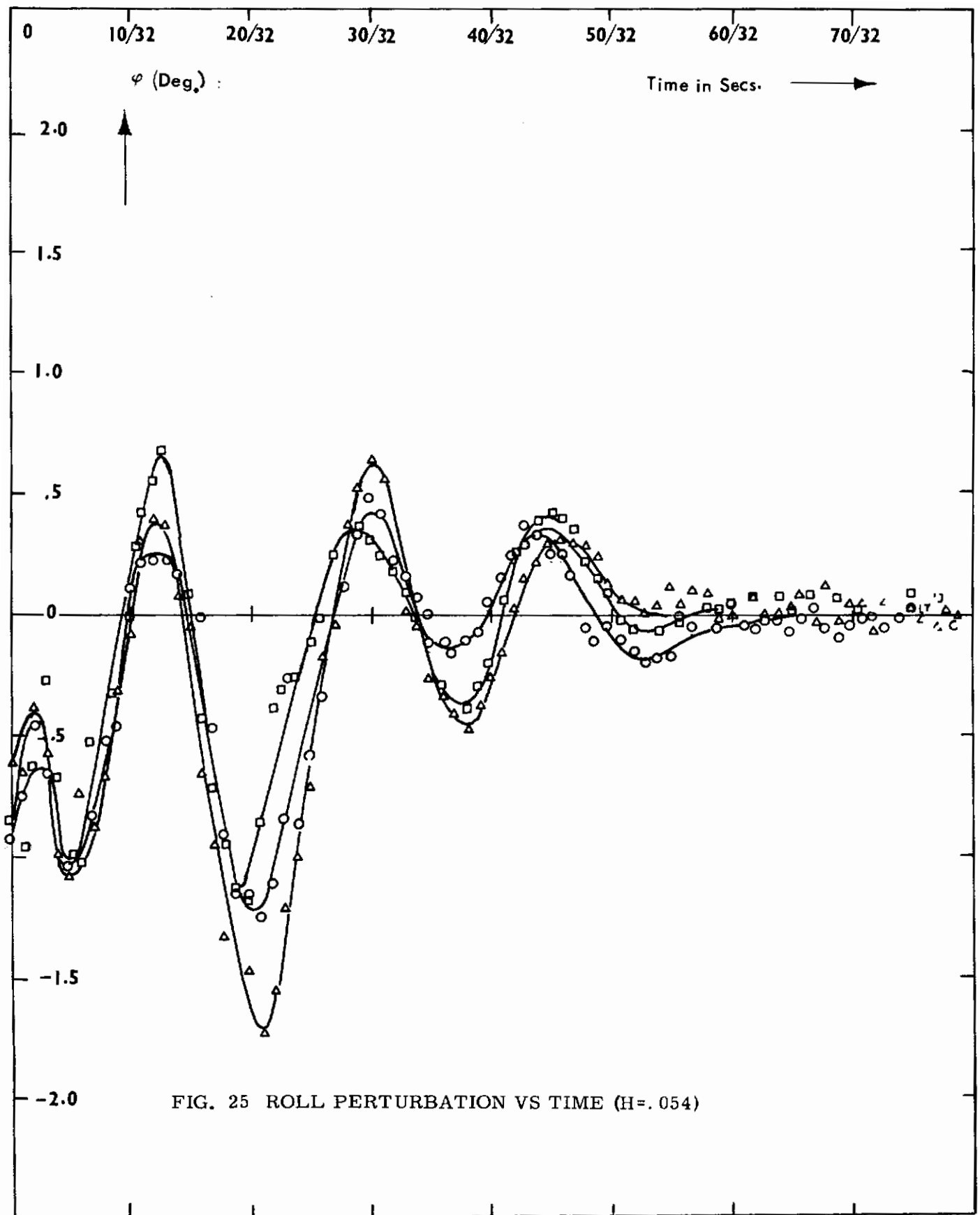


FIG. 25 ROLL PERTURBATION VS TIME (H=.054)

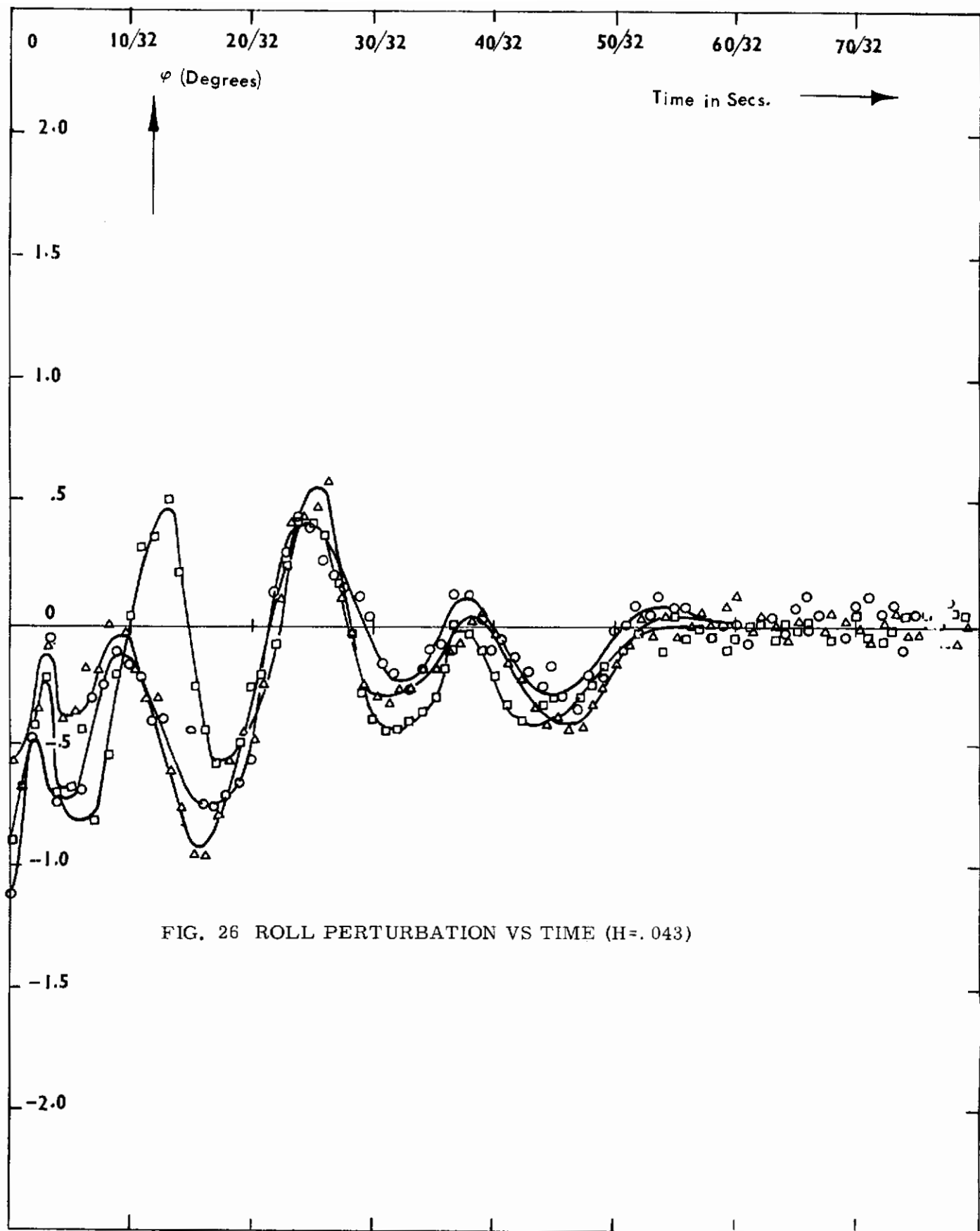


FIG. 26 ROLL PERTURBATION VS TIME (H=.043)

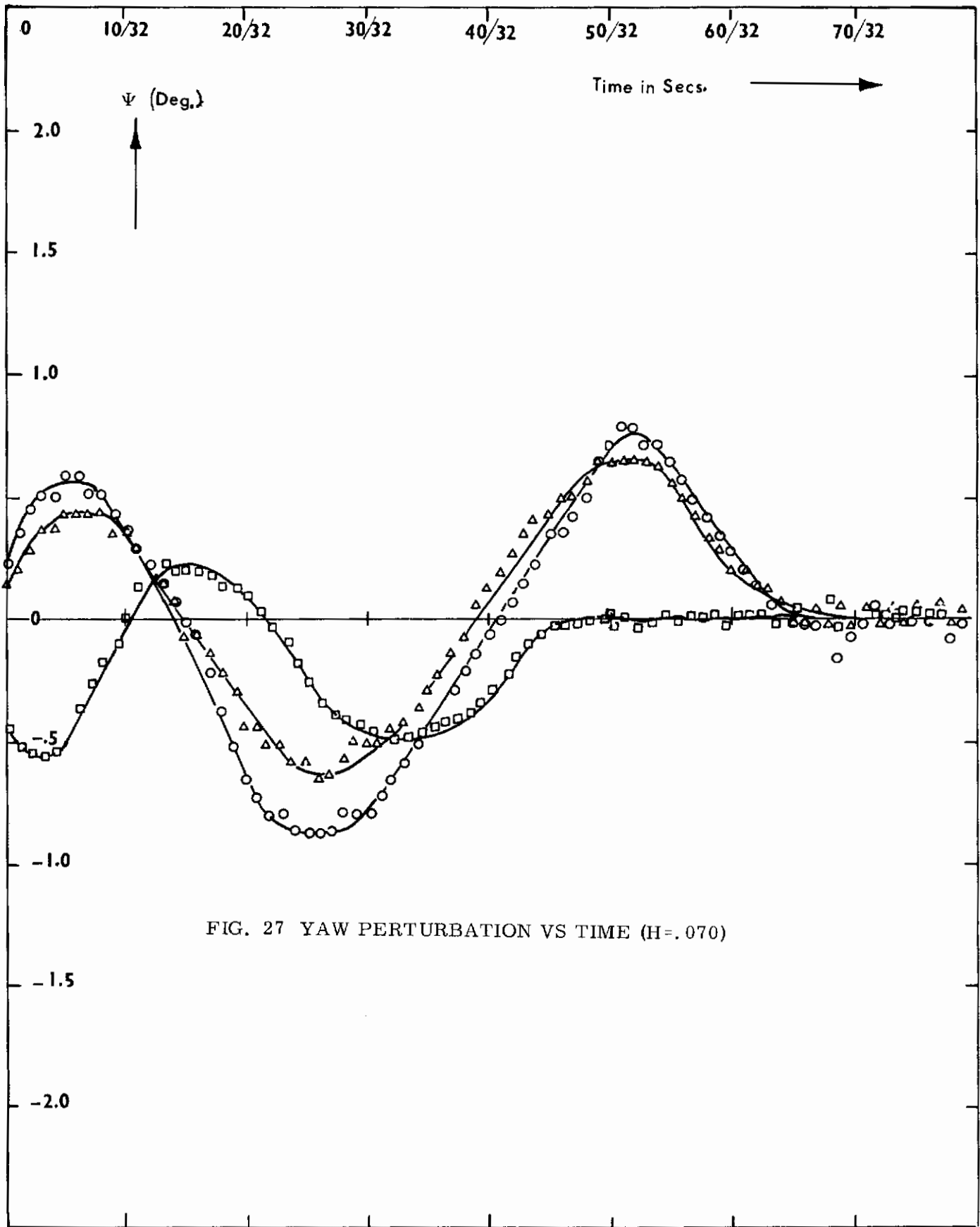


FIG. 27 YAW PERTURBATION VS TIME (H=.070)

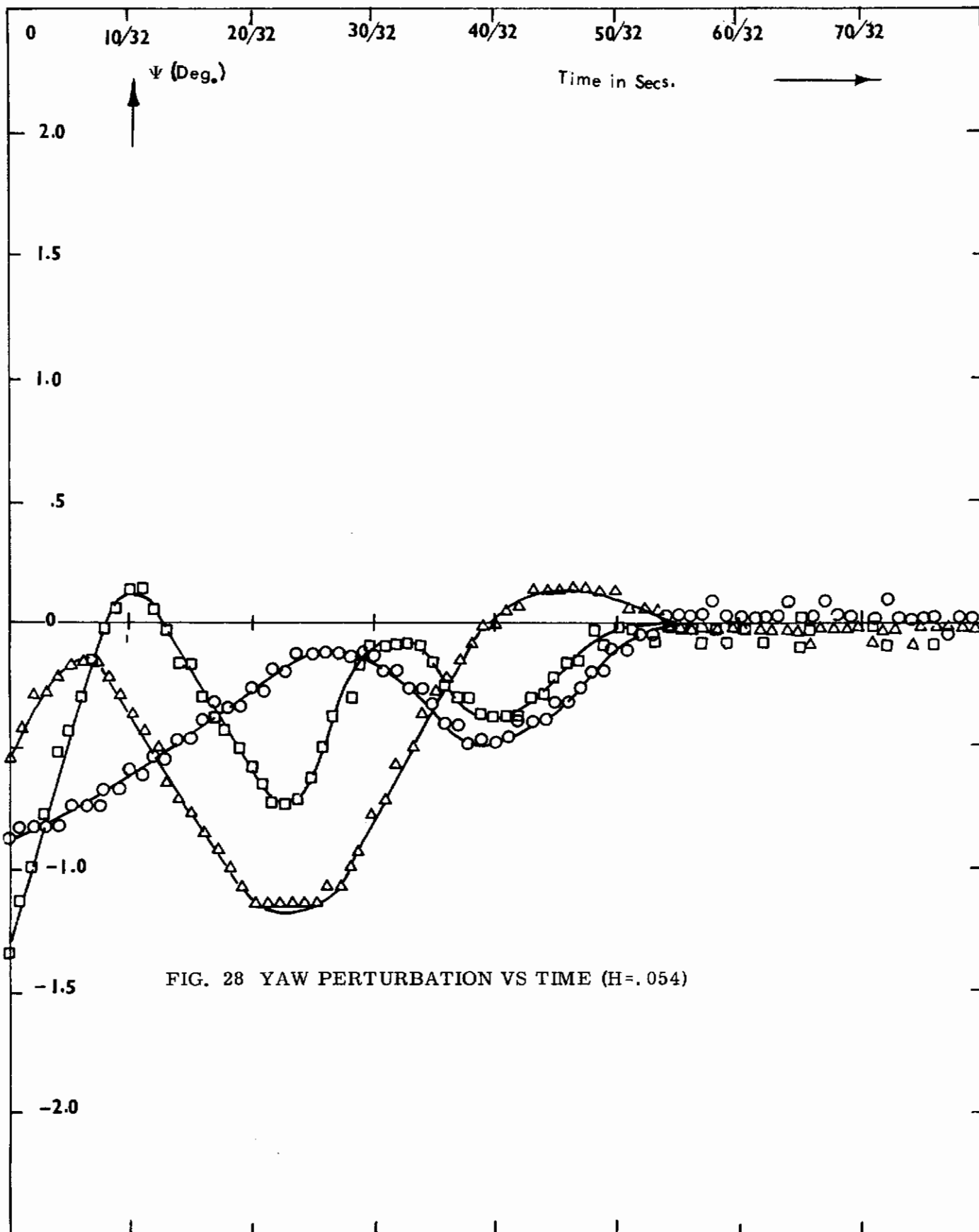


FIG. 28 YAW PERTURBATION VS TIME (H=.054)

# Contrails

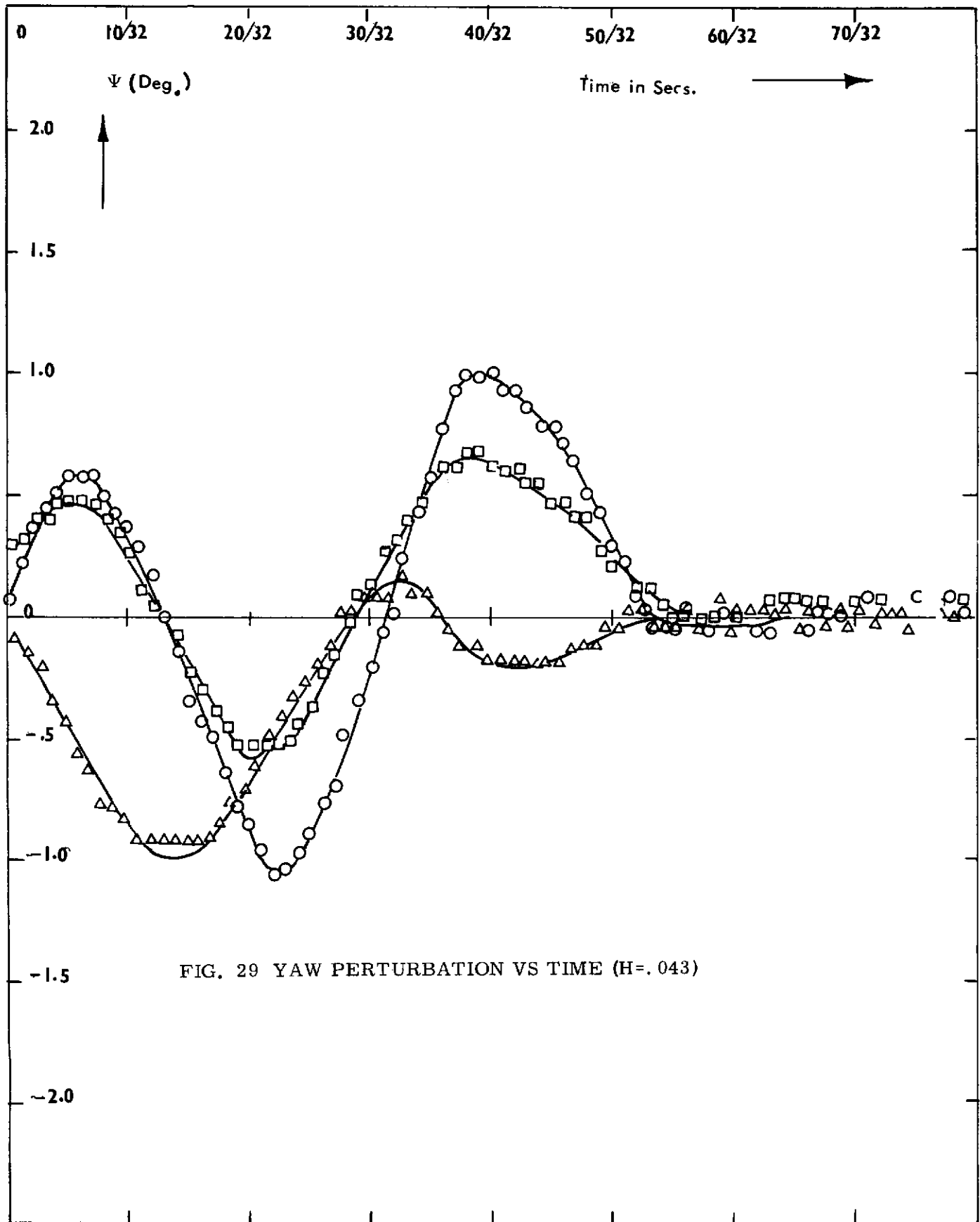


FIG. 29 YAW PERTURBATION VS TIME (H=.043)

# Contrails

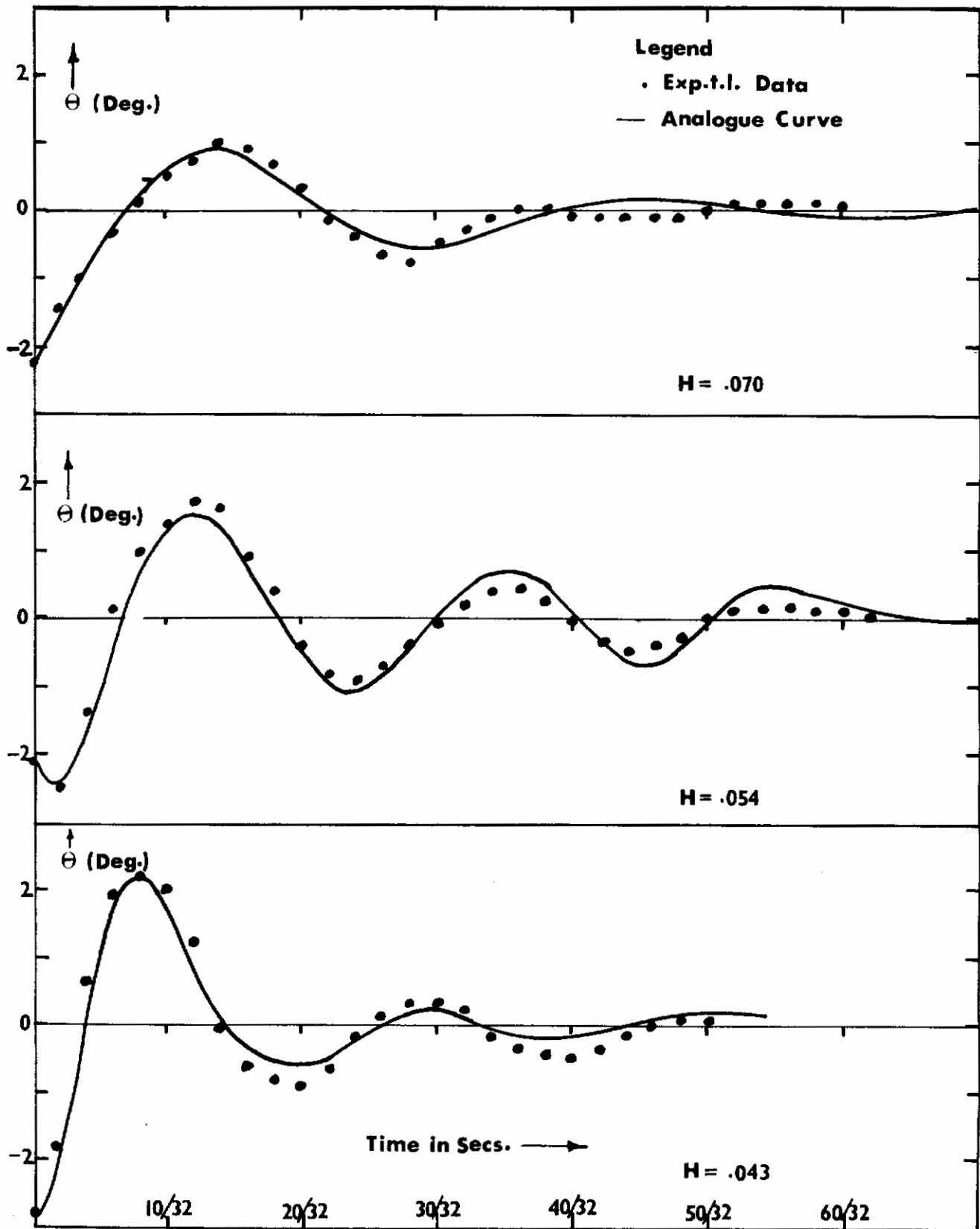


FIG. 30 A COMPARISON OF THE EXPERIMENTAL PITCH PERTURBATIONS AND THE ANALOGUE COMPUTER RESULTS



# Contrails

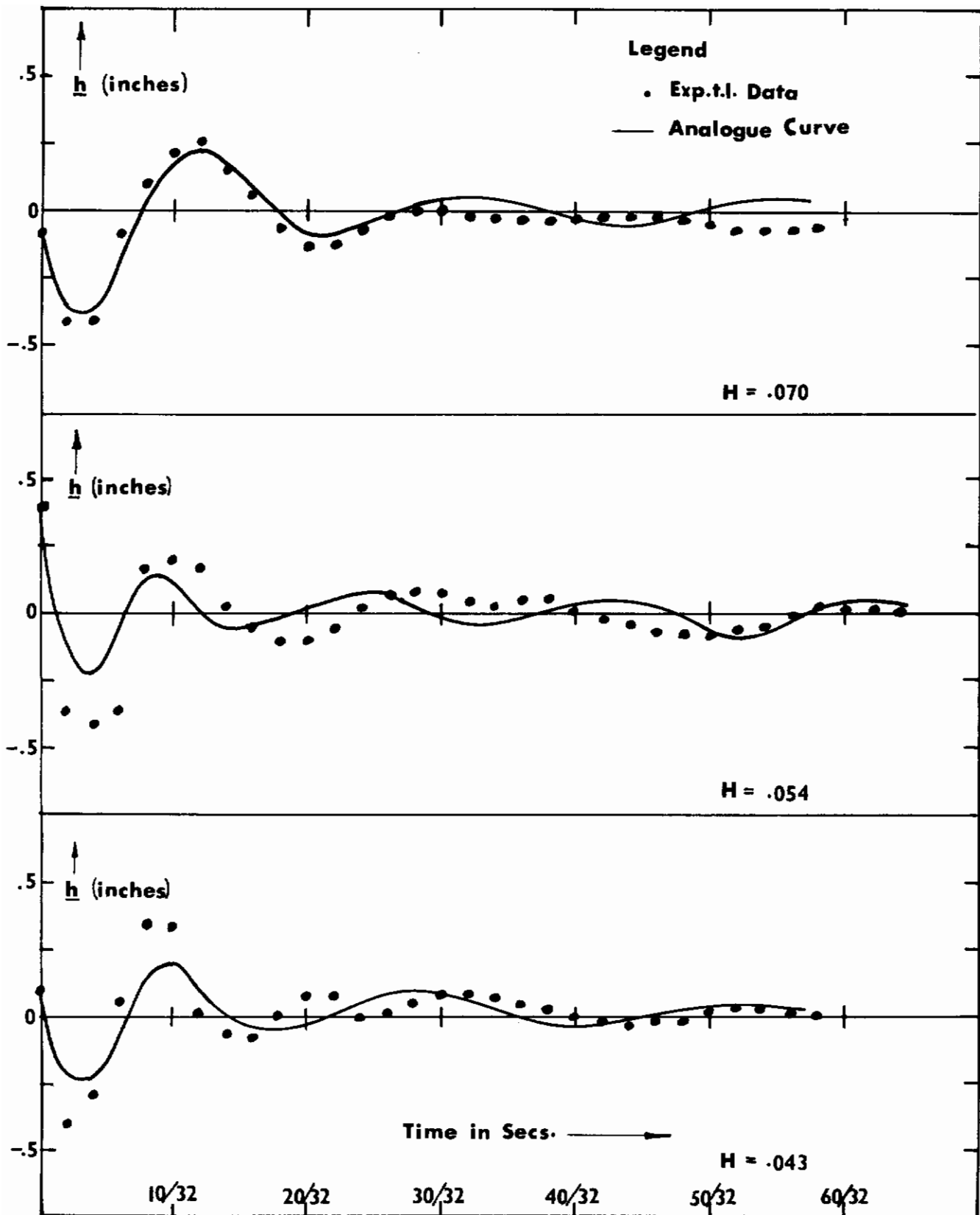


FIG. 31 A COMPARISON OF THE EXPERIMENTAL HEIGHT PERTURBATIONS AND THE ANALOGUE COMPUTER RESULTS

# Contrails

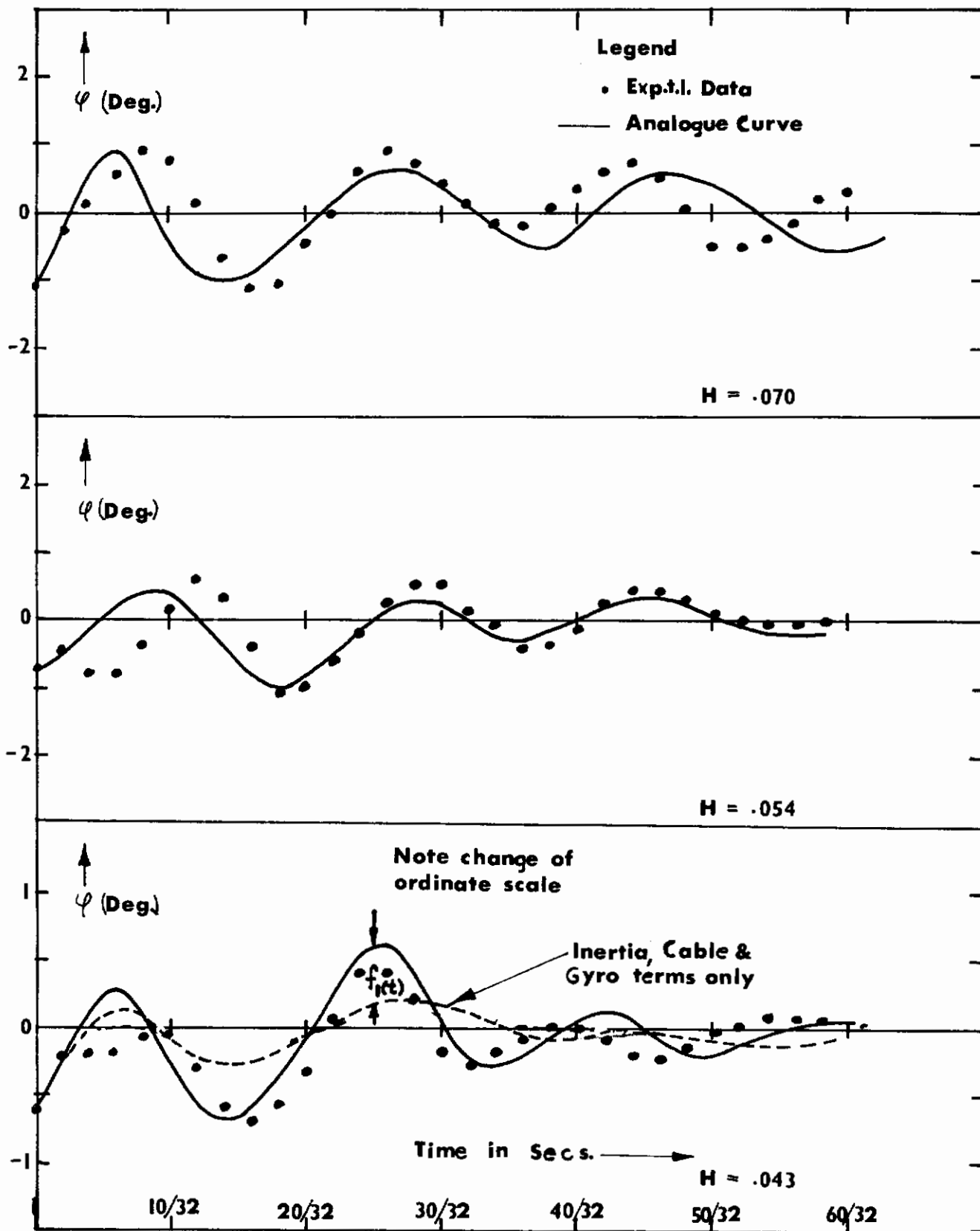


FIG. 32 A COMPARISON OF THE EXPERIMENTAL ROLL PERTURBATIONS AND THE ANALOGUE COMPUTER RESULTS

# Contrails

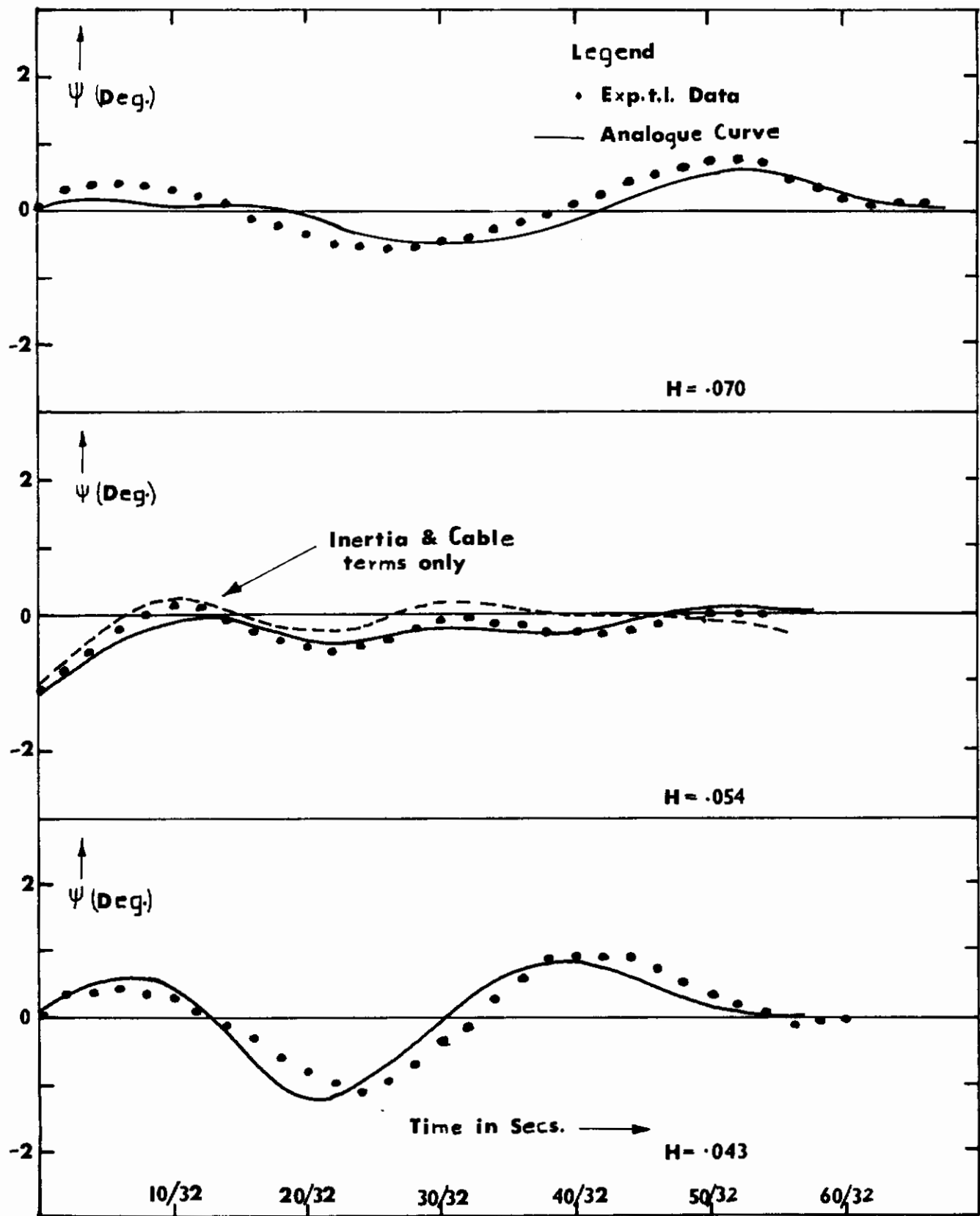


FIG. 33 A COMPARISON OF THE EXPERIMENTAL YAW PERTURBATIONS AND THE ANALOGUE COMPUTER RESULTS

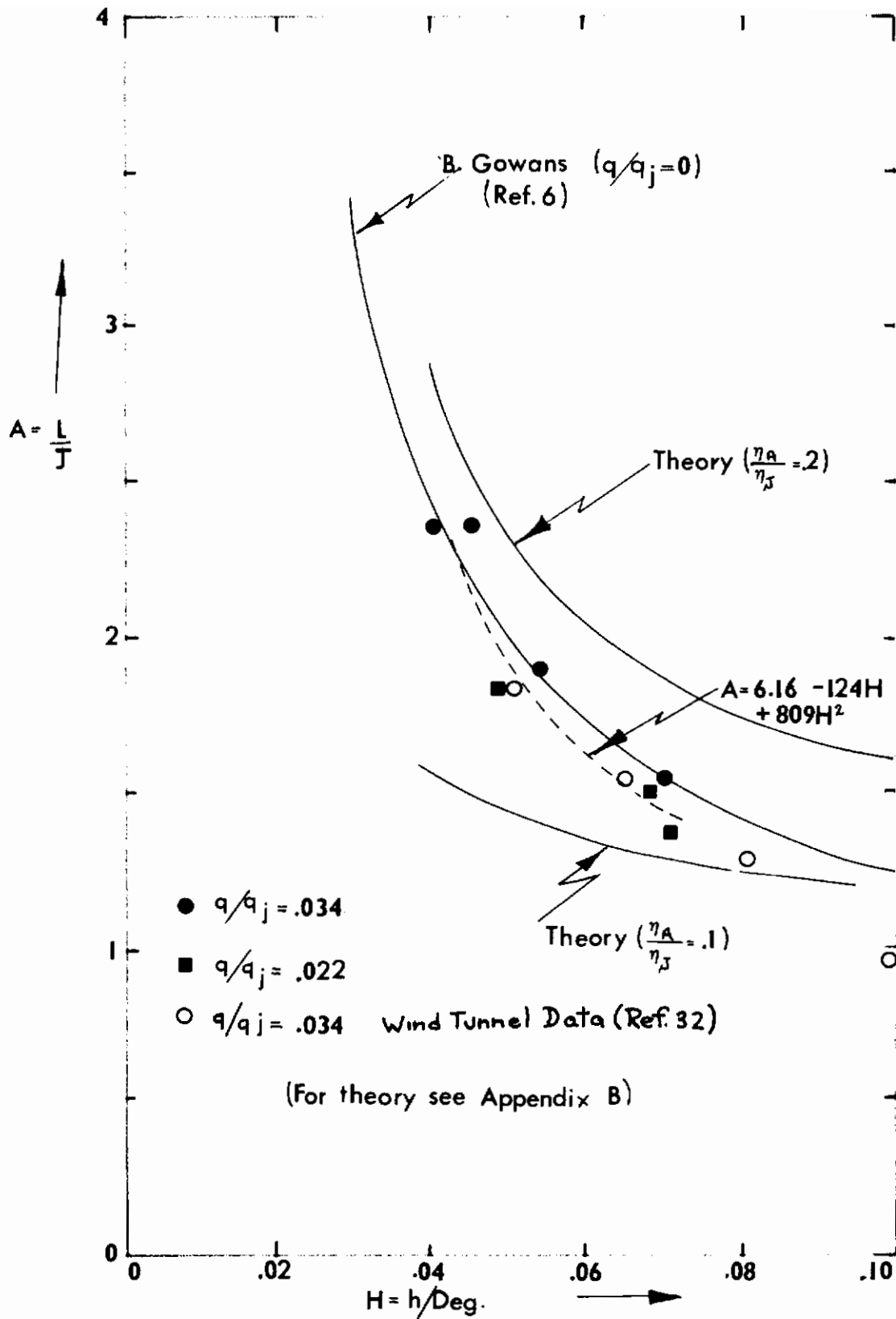


FIG. 34 THE AUGMENTATION CURVE

# Contrails

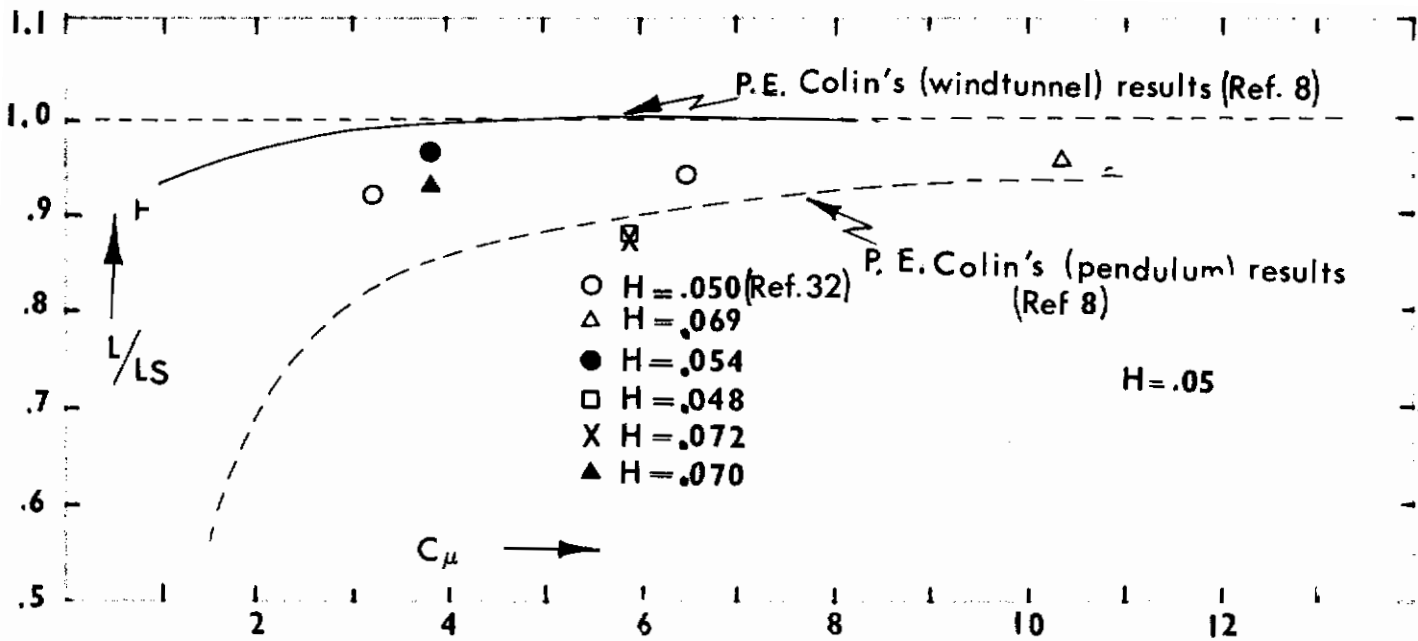


FIG. 35  $L/L_S$  VS  $C_{\mu}$

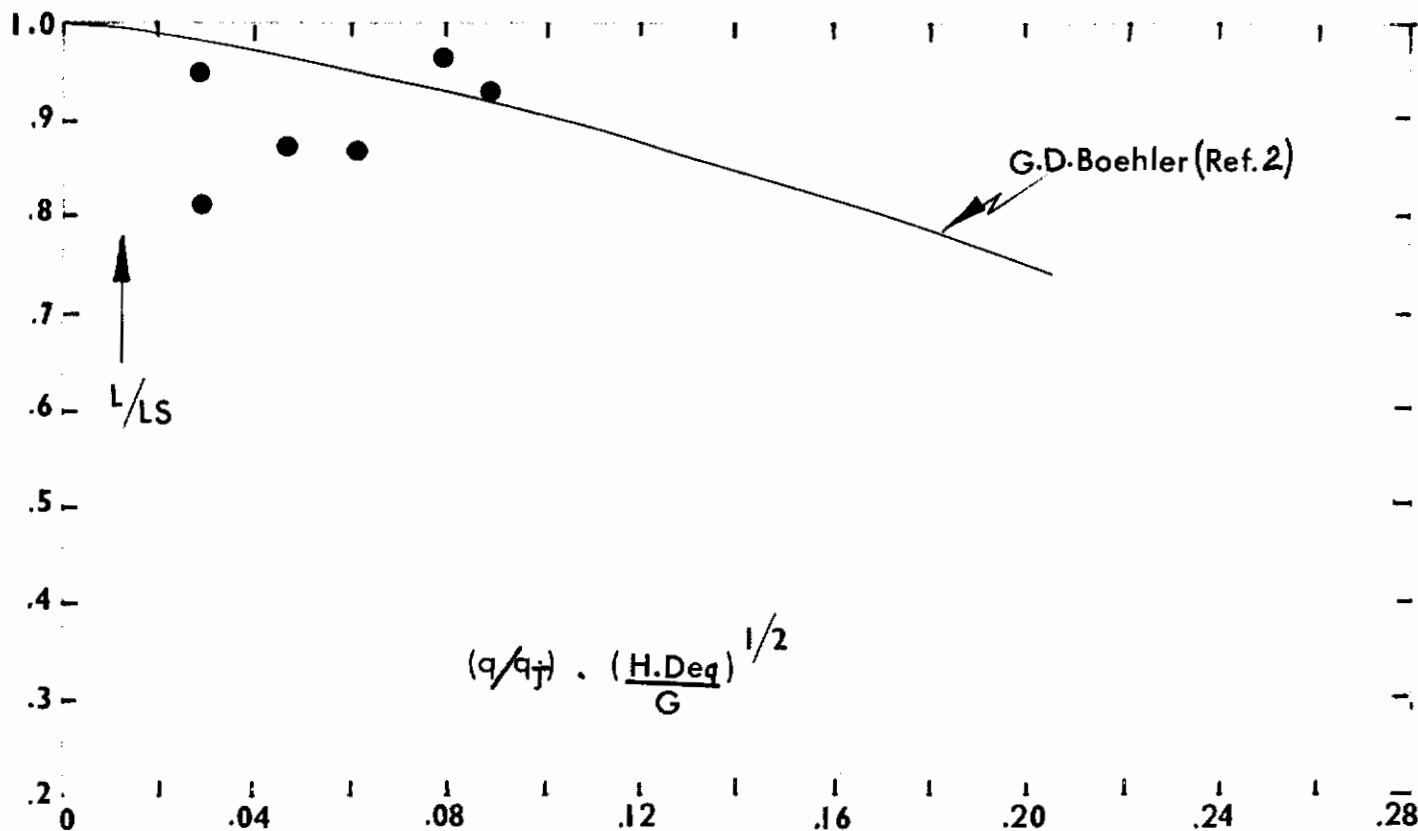


FIG. 36  $L/L_S$  VS  $(\frac{q}{q_J}) \cdot (\frac{H \cdot Deq}{G})^{1/2}$

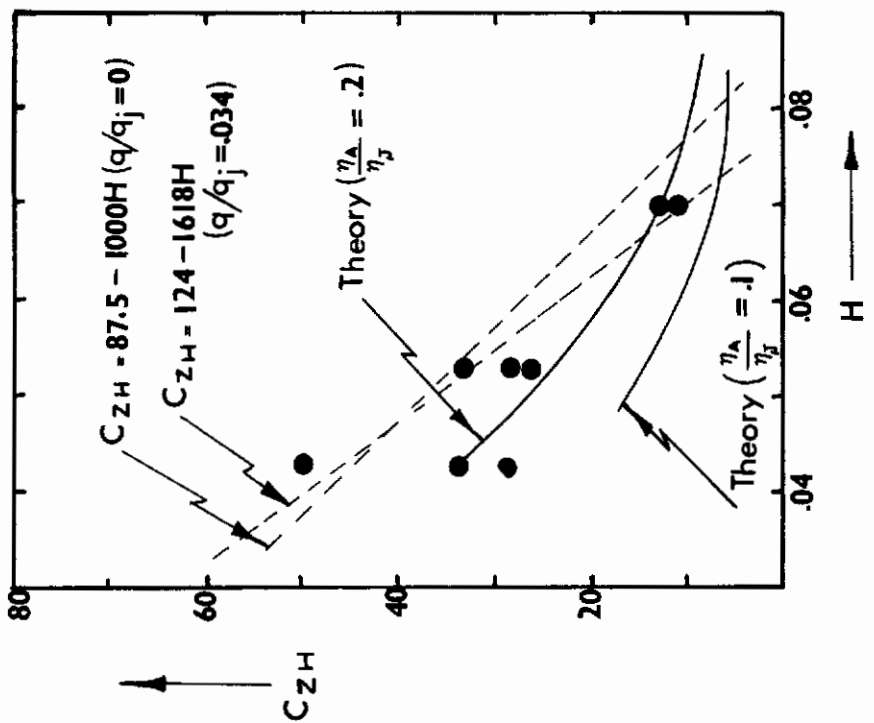
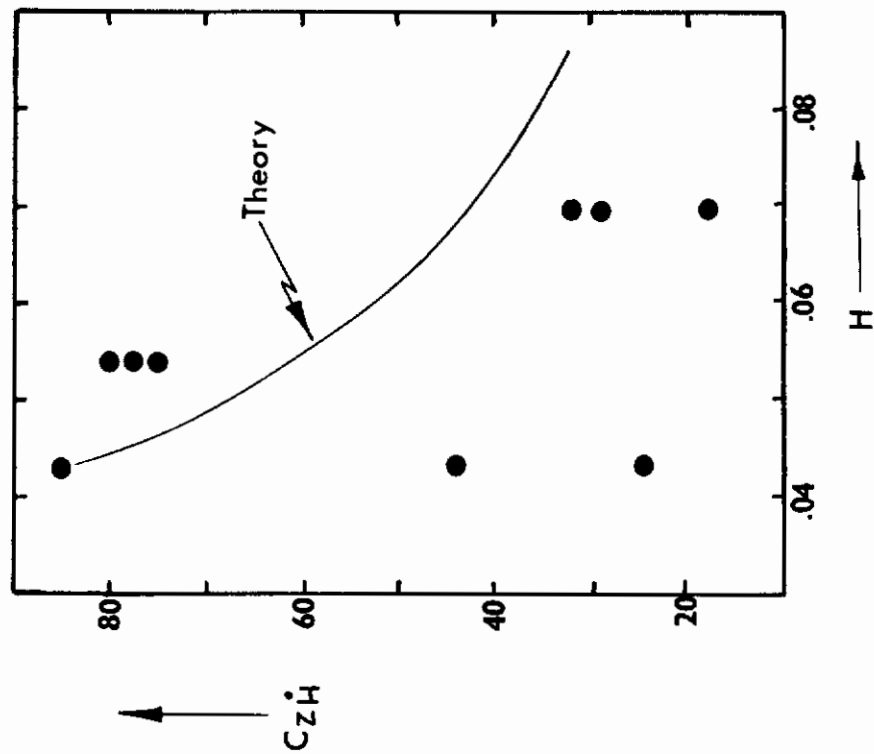


FIG. 37  $C_{ZH}$  AND  $C_{ZH}$  VS  $H$

*Contrails*

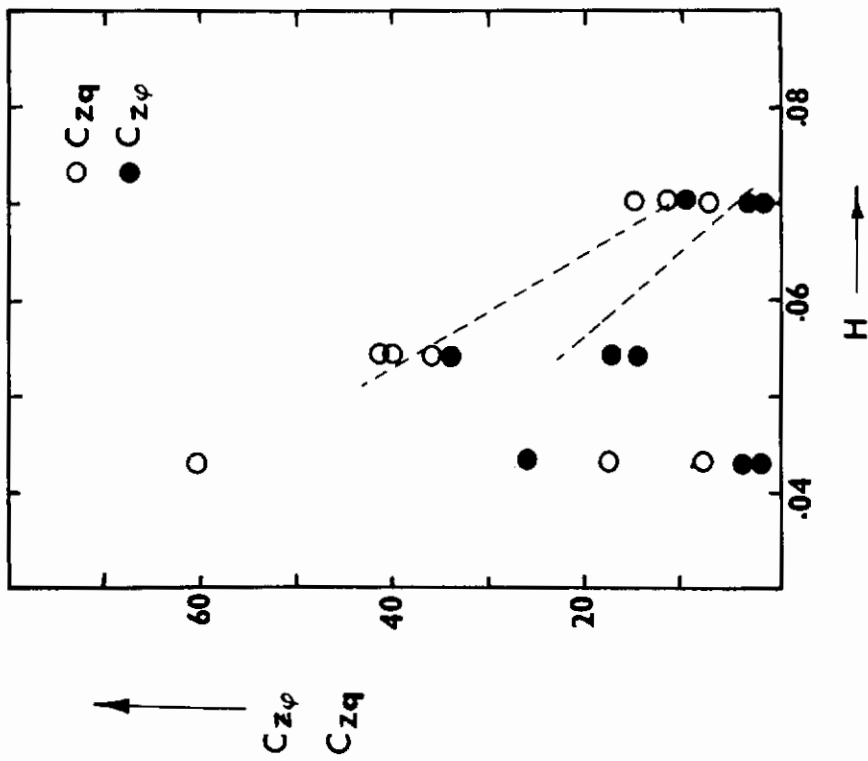
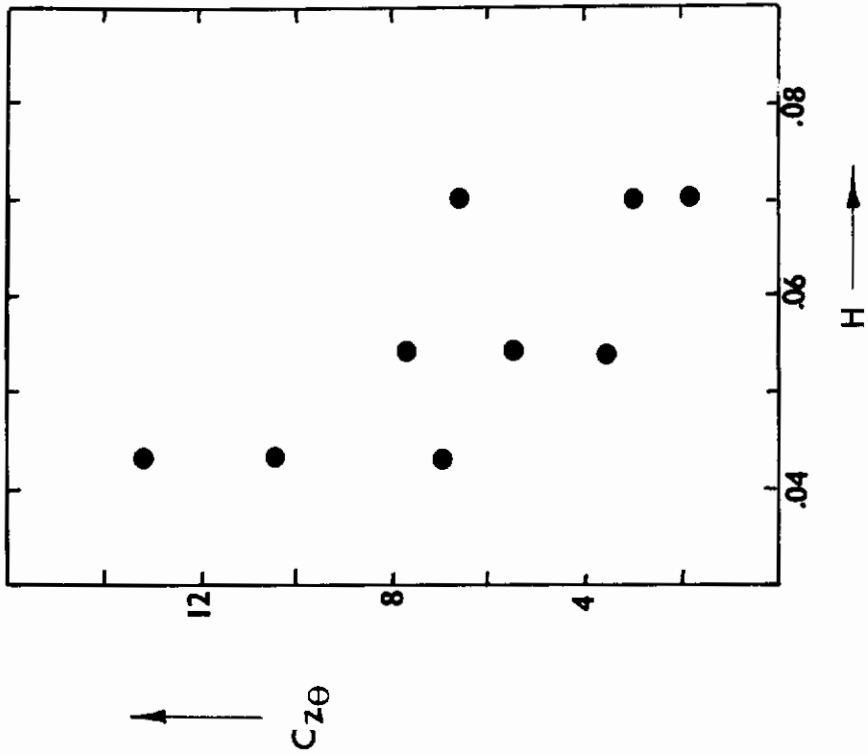


FIG. 38a.  $C_{z\phi}$ ,  $C_{zq}$  and  $C_{z\theta}$  VS H

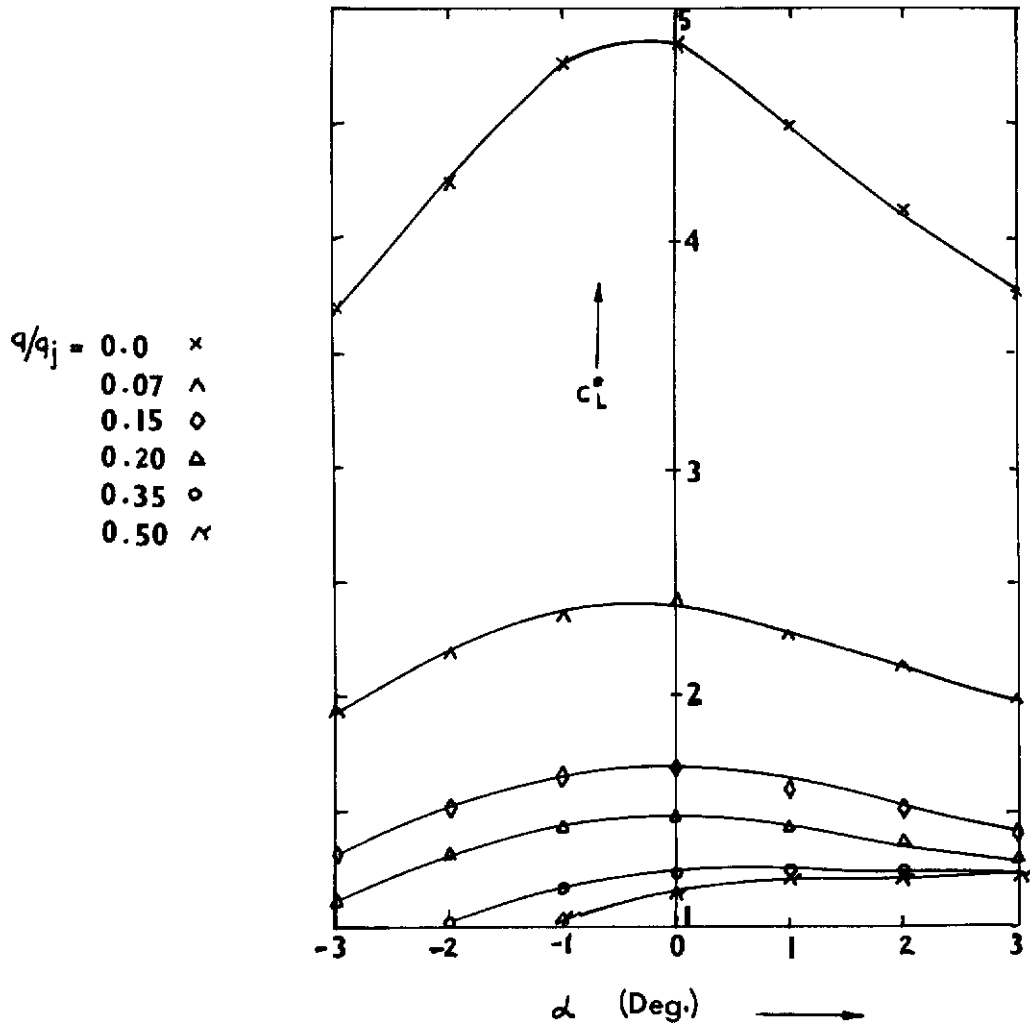


FIG. 38b LIFT VS  $\alpha$  (COURTESY OF K. DAU - REF. 13)



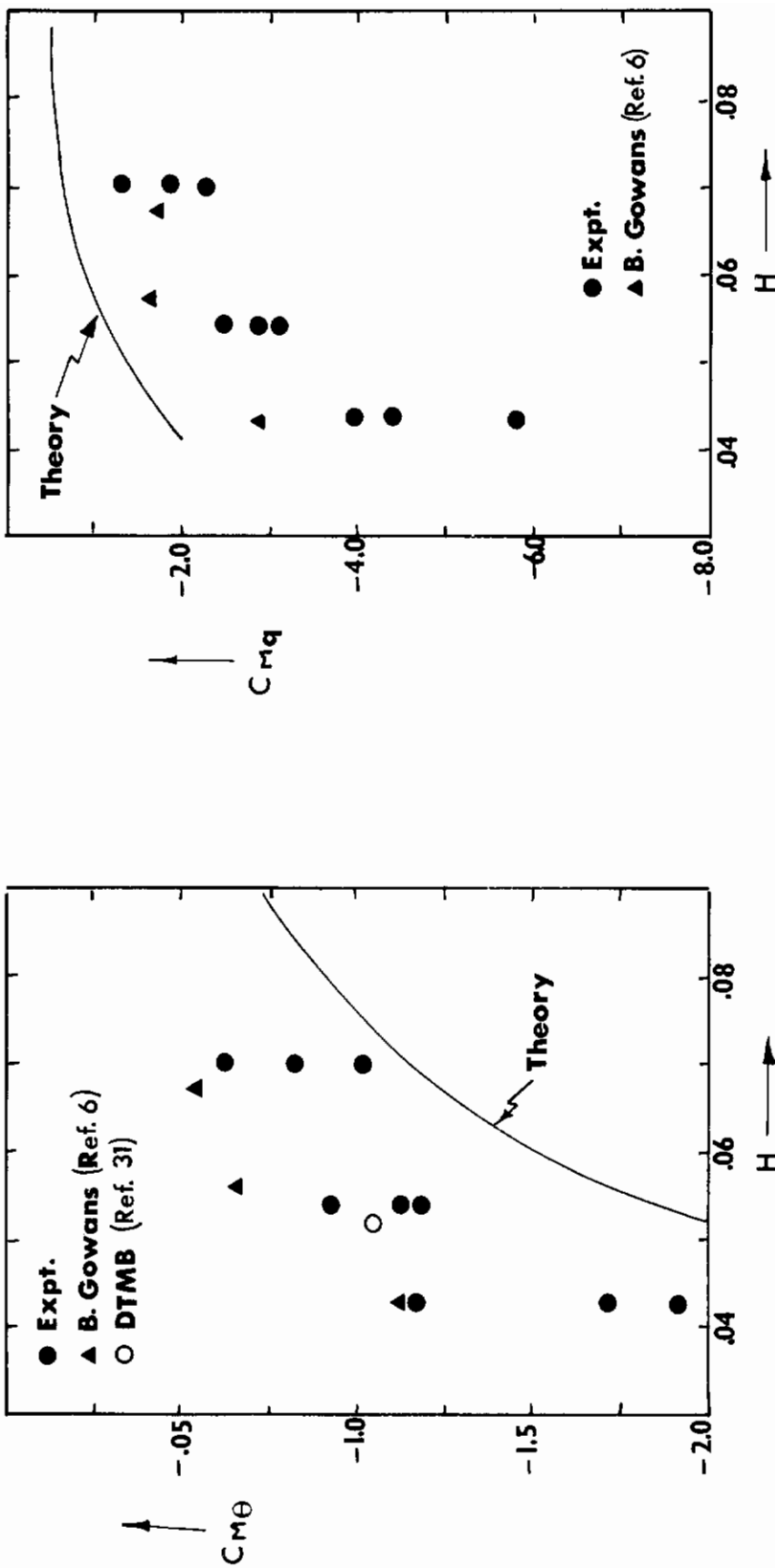


FIG. 39  $C_{M\theta}$  AND  $C_{Mq}$  VS H

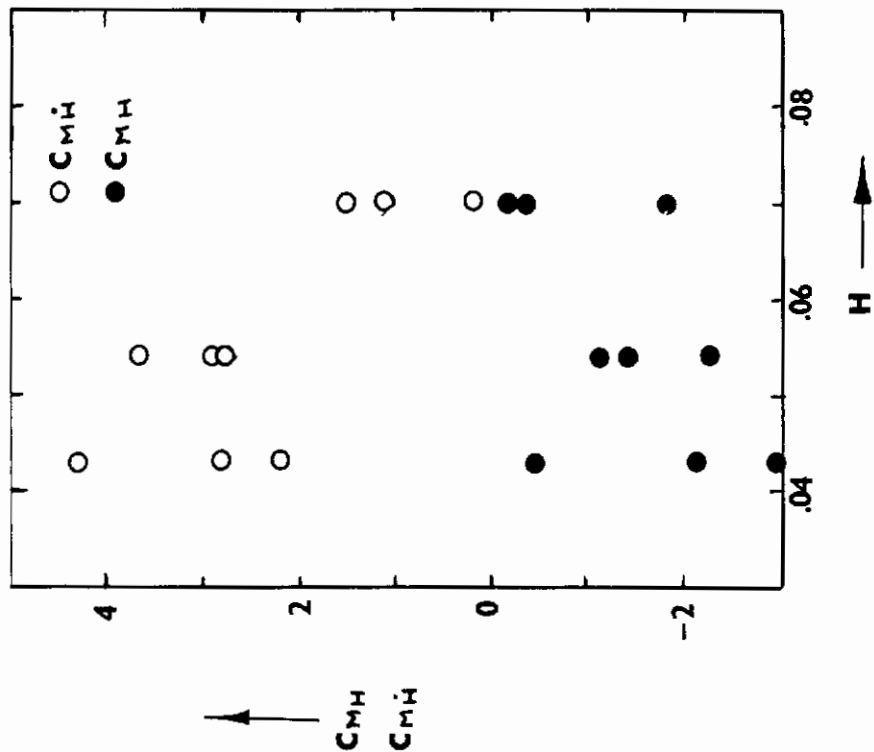
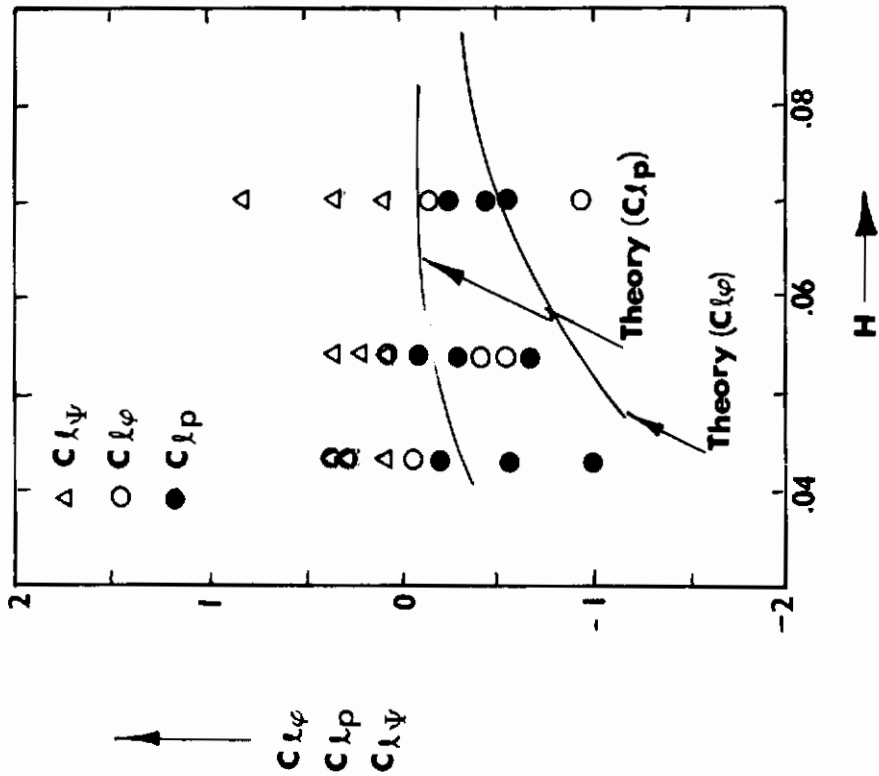


FIG. 40  $C_{MH}$ ,  $C_{MH}$ ,  $C_{l\phi}$ ,  $C_{l\rho}$ , AND  $C_{l\psi}$  VS  $H$

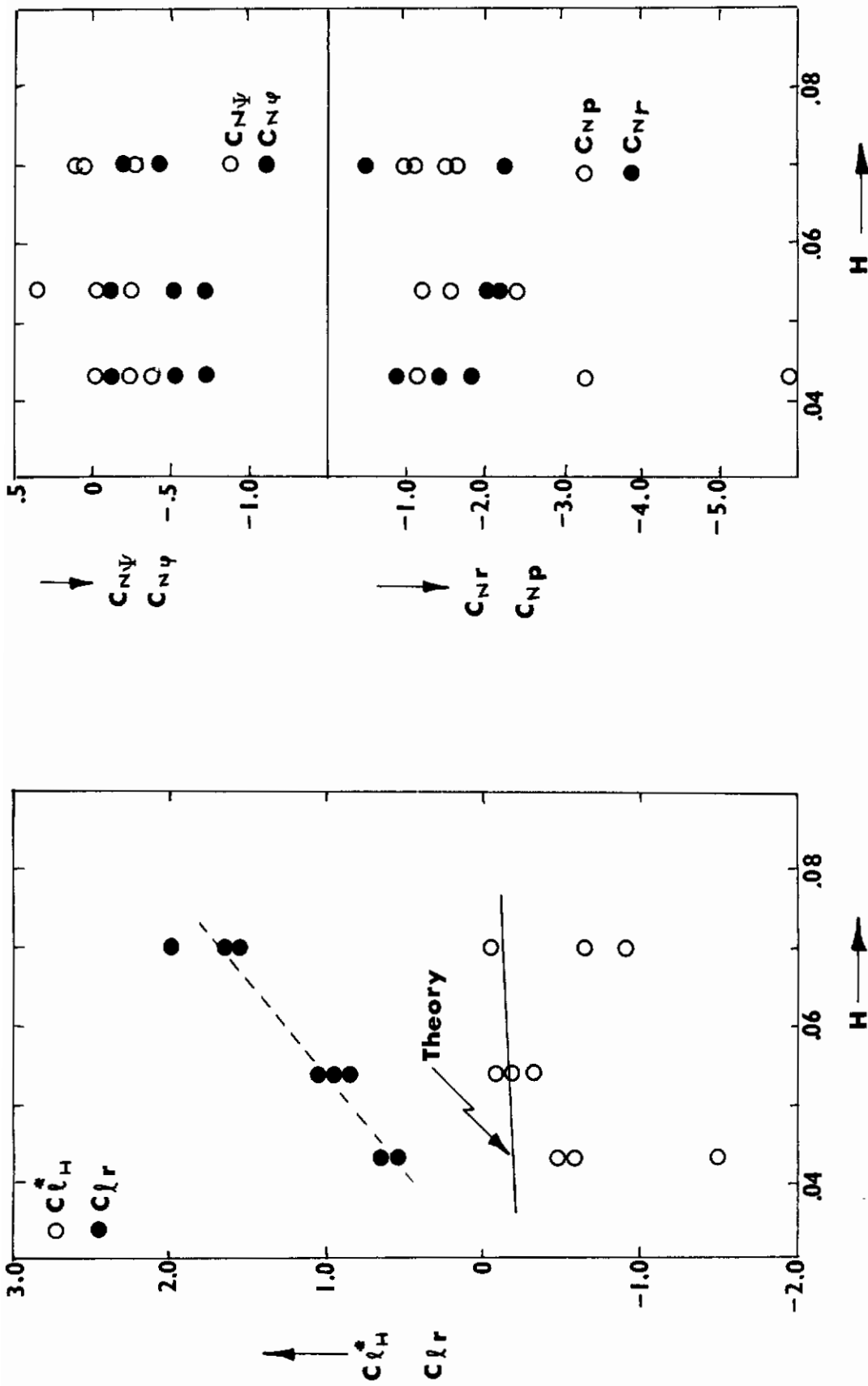


FIG. 41  $C_{lH}^*$ ,  $C_{lr}$  AND THE YAW DERIVATIVES VS H

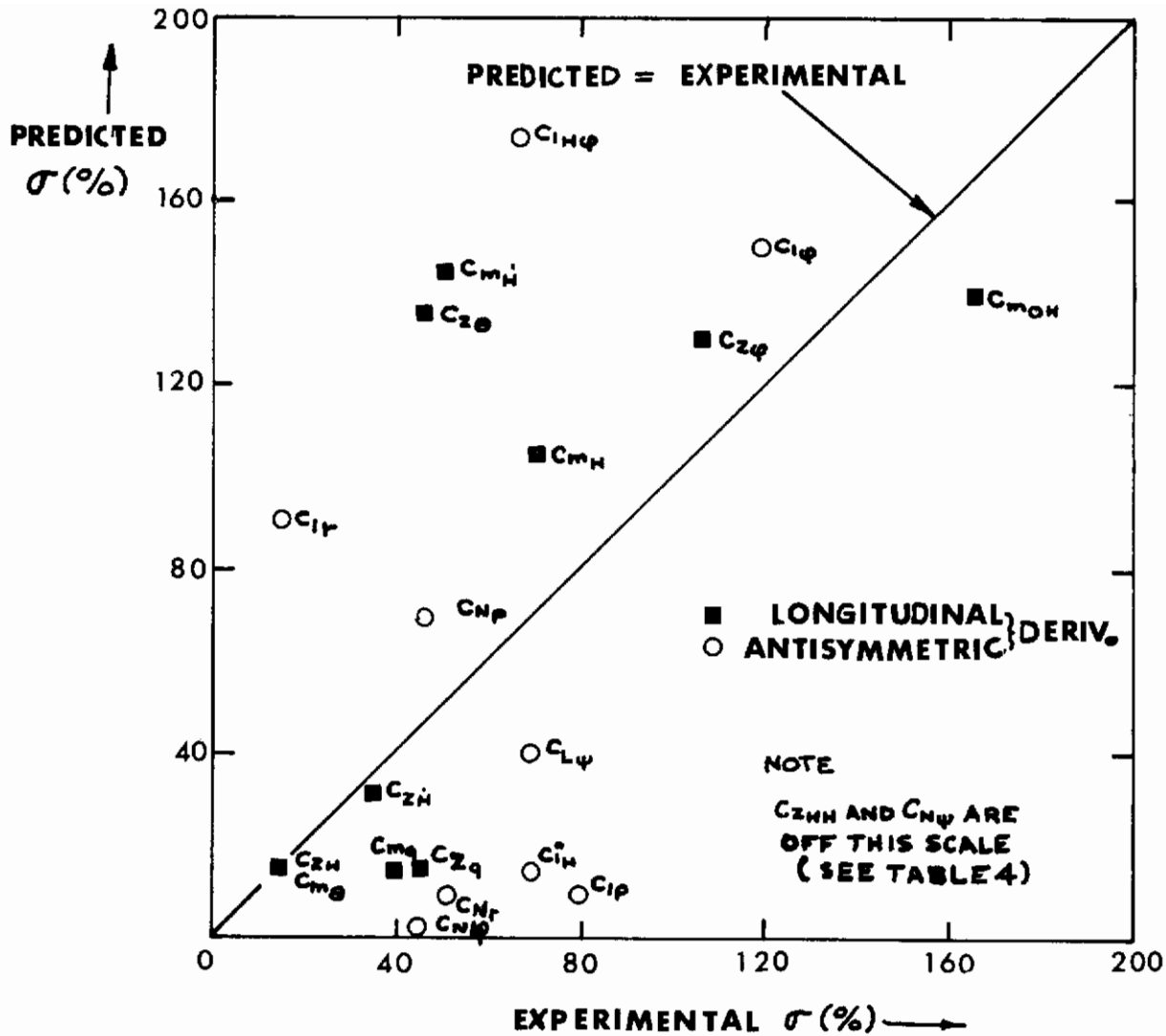


FIG. 41 a COMPARISON BETWEEN PREDICTED AND EXPERIMENTAL STANDARD DEVIATIONS

# Contrails

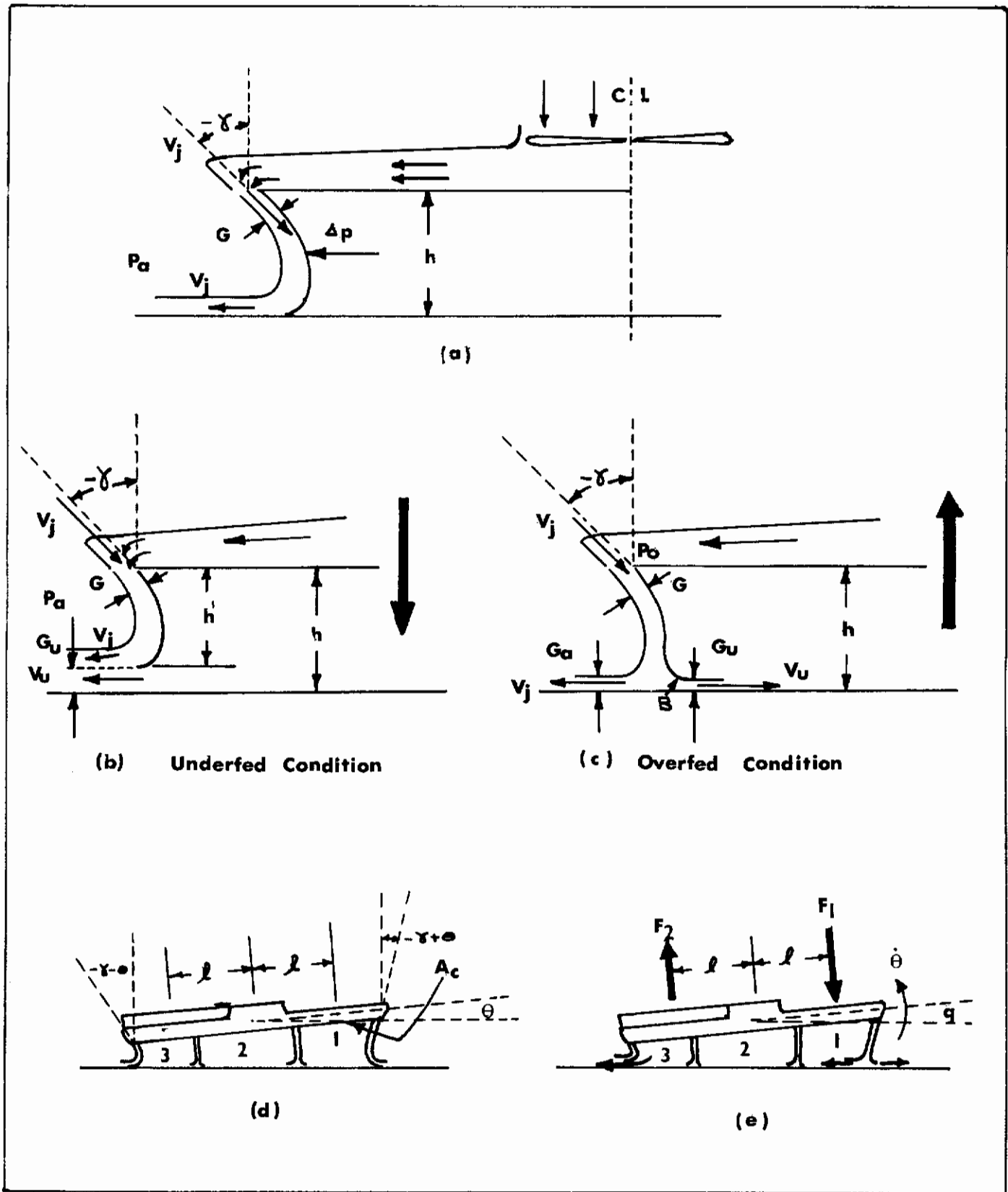


FIG. 42 SCHEMATIC DIAGRAMS FOR APPENDIX B

# *Contrails*

DOCUMENT CONTROL DATA - R&D

(Security classification of title, body of abstract and indexing annotation must be entered when the overall report is classified)

1. ORIGINATING ACTIVITY (Corporate author) <b>University of Toronto Toronto, Ont., Canada</b>		2a. REPORT SECURITY CLASSIFICATION <b>Unclassified</b>	
		2b. GROUP <b>N/A</b>	
3. REPORT TITLE <b>THE LIGHT-LINE-TETHERING TECHNIQUE FOR DETERMINING THE AERODYNAMIC DERIVATIVES OF AN AIR CUSHION VEHICLE</b>			
4. DESCRIPTIVE NOTES (Type of report and inclusive dates) <b>Final Report, Oct. 1960 to May 1965</b>			
5. AUTHOR(S) (Last name, first name, initial) <b>Kurylowich, G.</b>			
6. REPORT DATE <b>June 1966</b>		7a. TOTAL NO. OF PAGES <b>119</b>	7b. NO. OF REFS <b>--</b>
8a. CONTRACT OR GRANT NO. <b>AF33(657)-8451</b>		9a. ORIGINATOR'S REPORT NUMBER(S) <b>AFFDL TR 65-159</b>	
b. PROJECT NO. <b>8219</b>		9b. OTHER REPORT NO(S) (Any other numbers that may be assigned this report)	
c. Task: <b>821907</b>			
d.			
10. AVAILABILITY/LIMITATION NOTICES <b>Distribution of this document is unlimited.</b>			
11. SUPPLEMENTARY NOTES <b>None</b>		12. SPONSORING MILITARY ACTIVITY <b>AFFDL (FDCC) Wright-Patterson AFB, Ohio</b>	
13. ABSTRACT <p>A complete feasibility study was performed on a new technique for determining ACV aerodynamic derivatives. A circular track simulated "ground" while the vehicle, tethered to a centerpost by means of a light cable, flew a circular flight path above the track surface. A step on the "ground" perturbed the vehicle from equilibrium and the resulting oscillations were recorded by a movie camera. The results obtained indicated that many derivatives were functions of height.</p> <p>Although scatter in the data permitted a qualitative study only, it was concluded that the scatter resulted from random errors in the recorded time histories and the manner in which the cable was attached to the vehicle. By making certain improvements in the experimental design and apparatus (especially using a larger track) it was concluded that all derivatives could be obtained with satisfactory precision with this technique.</p>			

*Control*

14. KEY WORDS	LINK A		LINK B		LINK C	
	ROLE	WT	ROLE	WT	ROLE	WT
Air cushion vehicles						
Aerodynamics - ground effects						
Stability derivatives						
Aerodynamic model test method						
Tethered model tests						

**INSTRUCTIONS**

1. **ORIGINATING ACTIVITY:** Enter the name and address of the contractor, subcontractor, grantee, Department of Defense activity or other organization (*corporate author*) issuing the report.

2a. **REPORT SECURITY CLASSIFICATION:** Enter the overall security classification of the report. Indicate whether "Restricted Data" is included. Marking is to be in accordance with appropriate security regulations.

2b. **GROUP:** Automatic downgrading is specified in DoD Directive 5200.10 and Armed Forces Industrial Manual. Enter the group number. Also, when applicable, show that optional markings have been used for Group 3 and Group 4 as authorized.

3. **REPORT TITLE:** Enter the complete report title in all capital letters. Titles in all cases should be unclassified. If a meaningful title cannot be selected without classification, show title classification in all capitals in parenthesis immediately following the title.

4. **DESCRIPTIVE NOTES:** If appropriate, enter the type of report, e.g., interim, progress, summary, annual, or final. Give the inclusive dates when a specific reporting period is covered.

5. **AUTHOR(S):** Enter the name(s) of author(s) as shown on or in the report. Enter last name, first name, middle initial. If military, show rank and branch of service. The name of the principal author is an absolute minimum requirement.

6. **REPORT DATE:** Enter the date of the report as day, month, year; or month, year. If more than one date appears on the report, use date of publication.

7a. **TOTAL NUMBER OF PAGES:** The total page count should follow normal pagination procedures, i.e., enter the number of pages containing information.

7b. **NUMBER OF REFERENCES:** Enter the total number of references cited in the report.

8a. **CONTRACT OR GRANT NUMBER:** If appropriate, enter the applicable number of the contract or grant under which the report was written.

8b, 8c, & 8d. **PROJECT NUMBER:** Enter the appropriate military department identification, such as project number, subproject number, system numbers, task number, etc.

9a. **ORIGINATOR'S REPORT NUMBER(S):** Enter the official report number by which the document will be identified and controlled by the originating activity. This number must be unique to this report.

9b. **OTHER REPORT NUMBER(S):** If the report has been assigned any other report numbers (*either by the originator or by the sponsor*), also enter this number(s).

10. **AVAILABILITY/LIMITATION NOTICES:** Enter any limitations on further dissemination of the report, other than those

imposed by security classification, using standard statements such as:

- (1) "Qualified requesters may obtain copies of this report from DDC."
- (2) "Foreign announcement and dissemination of this report by DDC is not authorized."
- (3) "U. S. Government agencies may obtain copies of this report directly from DDC. Other qualified DDC users shall request through \_\_\_\_\_."
- (4) "U. S. military agencies may obtain copies of this report directly from DDC. Other qualified users shall request through \_\_\_\_\_."
- (5) "All distribution of this report is controlled. Qualified DDC users shall request through \_\_\_\_\_."

If the report has been furnished to the Office of Technical Services, Department of Commerce, for sale to the public, indicate this fact and enter the price, if known.

11. **SUPPLEMENTARY NOTES:** Use for additional explanatory notes.

12. **SPONSORING MILITARY ACTIVITY:** Enter the name of the departmental project office or laboratory sponsoring (*paying for*) the research and development. Include address.

13. **ABSTRACT:** Enter an abstract giving a brief and factual summary of the document indicative of the report, even though it may also appear elsewhere in the body of the technical report. If additional space is required, a continuation sheet shall be attached.

It is highly desirable that the abstract of classified reports be unclassified. Each paragraph of the abstract shall end with an indication of the military security classification of the information in the paragraph, represented as (TS), (S), (C), or (U)

There is no limitation on the length of the abstract. However, the suggested length is from 150 to 225 words.

14. **KEY WORDS:** Key words are technically meaningful terms or short phrases that characterize a report and may be used as index entries for cataloging the report. Key words must be selected so that no security classification is required. Identifiers, such as equipment model designation, trade name, military project code name, geographic location, may be used as key words but will be followed by an indication of technical context. The assignment of links, rules, and weights is optional.